

POLITECNICO DI TORINO  
Ph.D. in Mechanic, XXV cycle



**PhD Thesis**

**Prediction Method for the Surface Damage in  
Splined Couplings**

Tutor :

Prof. Francesca Curà

Coordinator:

Prof. Luigi Garibaldi

Candidate:

**Vincenzo Cuffaro**

February 2013

## CHAPTER 1: SPLINED COUPLINGS, DESCRIPTION, CLASSIFICATION, TRADITIONAL AND FATIGUE DESIGN.

1.1) Introduction	Pag 1
1.2) Classification of splined couplings	Pag 2
1.3) Traditional methods to design a spline coupling	Pag 7

## CHAPTER 2: FRETTING WEAR PHENOMENA

2.1) Introduction	Pag 10
2.2) Types of wear	Pag 12
2.3) Investigation on Fretting Wear	Pag 20
2.4) Fretting Wear on splined couplings	Pag 26

## CHAPTER 3: FRETTING WEAR MODELLING APPROACH

3.1) Introduction	Pag 29
3.2) Fretting wear modelling approach	Pag 30
3.3) Splined couplings analytical model	Pag 30
3.4) Contact pressure	Pag 56
3.5) Contact slip amplitude	Pag 75
3.6) Fretting models	Pag 80

## CHAPTER 4: SPLINED COUPLING TEST BENCH

4.1) Introduction	Pag 82
4.2) Test bench description	Pag 82
4.3) Test bench characteristics	Pag 86
4.4) Measuring instruments	Pag 88
4.5) Control system	Pag 89
4.6) Wear Tests	Pag 90
4.7) Test interruption	Pag 91
4.8) Parameters monitored during the tests	Pag 92
4.9) Tests description	Pag 95
4.10) Test Article geometry	Pag 95

## CHAPTER 5: SPECIMEN SURFACE TOPOGRAPHY

5.1) Introduction	Pag 102
5.2) The amplitude parameters	Pag 102
5.3) The spacing parameters	Pag 113
5.4) The hybrid parameters	Pag 119
5.5) Surface roughness tester ALPA-SM RT 70	Pag 126

## CHAPTER 6: EXPERIMENTAL RESULTS

6.1) Introduction	Pag 130
6.2) Cataloging phase	Pag 130
6.3) Results of test 1	Pag 132
6.4) Results of test 2	Pag 143
6.5) Results of test 3	Pag 149
6.6) Results of test 4	Pag 157
6.7) Discussion	Pag 163

## CHAPTER 7: CONCLUSIONS

Pag 166

## INTRODUCTION:

At the beginning of the last century the increase in machine performance has led to the evidence of new damage events or premature failures in components, due to the phenomenon generally referred as fatigue.

Similarly, in recent decades, the progresses in technology have led to further improvements in machine performance in terms of power, dynamic behavior and weight reduction, but in the other hand, they have led to the emergence of new types of damage, in particular the damage phenomenon known as fretting.

Generally, the first failures due to fatigue were difficult to interpret and only in-depth study of the phenomenon, from the beginning until now, led to his in-depth understanding and the formulation of related laws describing the evolution of damage. This study allowed to the creation of more or less complex design criteria.

In the same way, nowadays the fretting is a phenomenon not easy to understand and quantify, which creates big problems to producers and users of machines in general, in many industrial sectors (aerospace, rail, automotive, biomedical, etc.). Currently design criteria that can be applied to components to predict fretting damage are not available. Nevertheless design criteria are needed in order to check components about this phenomenon, avoiding the formation of this type of damage or at least to keep it under control.

Being able to formulate standardized procedures for fretting verification at the design phase would result, as well as to a reduction of costs (caused by the need to replace worn components), also and primarily to an efficiency increase of the machines (allowing to decrease the weight of the components) and their safety and reliability.

For these reasons, in recent years, is growing an increasing interest for the study of the fretting, both with regard to the scientific community, both in the industrial world.

The fretting appears when two bodies in contact, pressed by a force, undergo small displacements and this friction leads to the rise of damage.

This phenomenon is divided into two categories: fretting wear and fretting fatigue; in both its types, it is very tricky and dangerous, as components that are statically and fatigue verified or even oversized may have the onset of fretting, that once triggered is a degenerative process that leads to the failure of the component.

The general difficulty of formulating a quantitative model for fretting damage has led the scientific community to focus interest on this phenomenon, although to date there are no robust verification procedures for simplified models of contact. Things are even more complicated considering components with complex geometries, as an example splined shafts teeth.

Recently a collaboration of the Politecnico di Torino and Avio Group, called GREAT LAB, was started.

The program was aimed at supporting the participation of the Regione Piemonte in European projects, researching new environmental aeronautical engines entering service in 2020. The object of this research activity is to develop new design criteria for transmissions.

This work starts from the basis of the above quoted project, taking the particular way referred to the damage analysis in splined couplings

The primary purpose of my PhD thesis was to develop design criteria and to verify procedures about fretting wear, that are applicable to crowned spline couplings of a power transmission system of the aeroengines

In fact, aeroengine splined couplings, particularly mainshaft, low pressure (LP) splines, are complex components that can fail from a variety of mechanisms, and are particularly susceptible to fretting wear (FW) and fretting fatigue (FF), as a result of small oscillatory relative movements between the highly-loaded teeth.

Consequently there was an huge investment, from companies working in aviation sector, to study and to resolve this type of early components decommissioning during the last years.

Fretting is a very complex phenomenon being influenced by many factors, the most important being the presence or absence of lubrication, the load distribution (contact pressure) and the sliding between the bodies.

Therefore, the study of fretting needs a deep knowledge of these three main aspects.

The first aspect of the problem was based on models and experimental tests considering specify specimens (crowned spline couplings) and imposed movements, so as to uniquely identify the working conditions (load and sliding), in order to facilitate the comparison between the experimental tests and the analytical models.

The analytical models have been validated with numerical simulations and by comparison with experimental data, that have been obtained by means of a dedicated test bench that has been designed and built.

Thanks to the test rig was possible to determinate the real contact pressure of two engaging teeth; in fact, it is one of the most important parameters affecting the fretting phenomenon, but it is very difficult to evaluate in a quantitative way, especially when considering components with complex geometries.

The second phase of this thesis was the development of a predictive model for crowned splined couplings. This model is based on the Ruiz first parameter.

The aim of my thesis is to demonstrate how this parameter may be correctly applied to a complex component as the crowned spline coupling, taking into account experimental and FEM validations.

# CHAPTER 1: SPLINED COUPLINGS, DESCRIPTION, CLASSIFICATION, TRADITIONAL AND FATIGUE DESIGN

## 1.1) INTRODUCTION

The mechanical parts joining through components that can be removed when necessary without altering connected parts are properly carried out in most cases by threaded elements.

However, on several occasions, a variety of other linkages are used like removable non-threaded connections which includes the splined couplings.

The splined couplings combine coaxial elements (shaft - hub) that transmitting torque by means of equidistant teeth situated outside of a cylindrical element (shaft) by corresponding vain located within hollow cylindrical element (hub).

According to the shape of the teeth, the splined couplings are divided into: spline with parallel sides and spline with involute teeth.

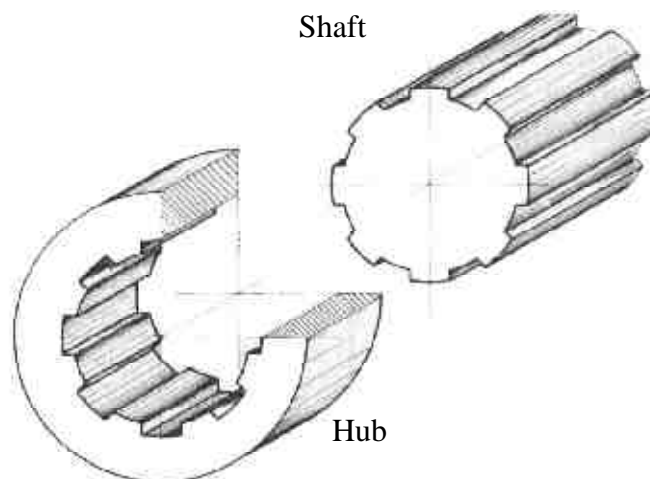


Figure 1.1: Example of a spline coupling [1]

Splined couplings derive from the need of designers to create mechanical components that can rotate at a high speed and can satisfy the widest variety of requirements at the same time:

- to prevent relative rotation of the coupled elements;
- to avoid the mutual translation;

- to avoid a spontaneous disassembling or to prevent the movement above (as well as) predetermined limit.

One of the most common problems to be solved is the connection between rotating shaft and hub so that they can rotate rigidly. The use of keys or tongues leads to shaft weakening, above all if more than one has to be adopted in order to transmit high torque values.

Splined couplings may easily overcome the above cited difficulties

## 1.2) CLASSIFICATION OF SPLINED COUPLINGS

Splined couplings in accordance with shaft shape teeth and hub keyway can be divided into two main categories (Figure 1.2):

- straight teeth
- involute teeth.

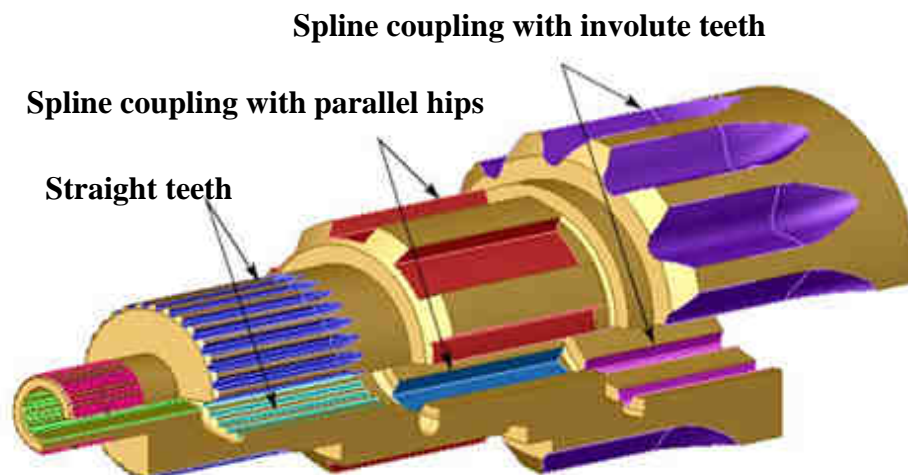


Figure 1.2: Splined couplings types [1]

### 1.2.1) Classification by teeth shape

According to the shape of teeth, Giovannozzi [1] specifies that there are:

- teeth with straight radial sides, then the edge of each tooth is straight and aligned parallel to the axis of rotation;
- teeth with inclined straight sides;

- teeth with involute profile;
- teeth having rounded sides called “crowned-tooth splines”.

a) *Splined couplings with straight radial sides teeth:*

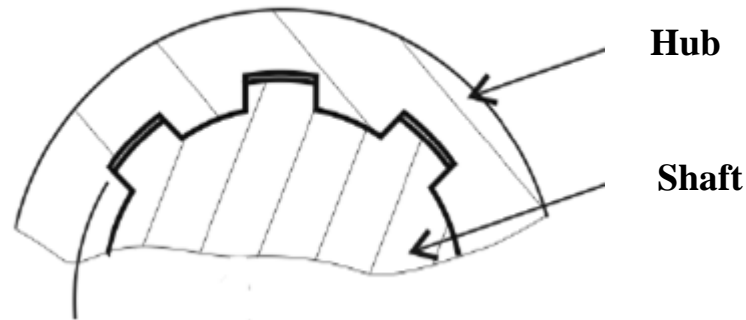


Figure 1.3: representation of teeth with straight radial sides [1]

Shaft of the spline coupling with straight sides is made by milling, while the hub is made by broaching (Figure 1.3). Until now the only Standard applicable is the UNI 8953-86 that replaces the UNI220, the UNI221, the UNI 4400P, the UNI219, the UNI222, the UNI223, the UNI224 and the UNI225. These spline couplings are used when the precision of assembly is not important and power transmission is not very high.

b) *Splined couplings with inclined straight sides teeth:*

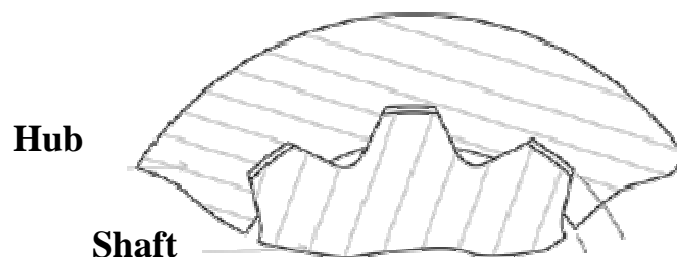


Figure 1.4: representation of inclined straight sides teeth [1]

Their geometry depends on the inclination of the sides between adjacent reliefs (Figure 1.4).

Adjacent sides are connected together on the bottom by circular arcs.

c) *Splined couplings with involute profile teeth:*

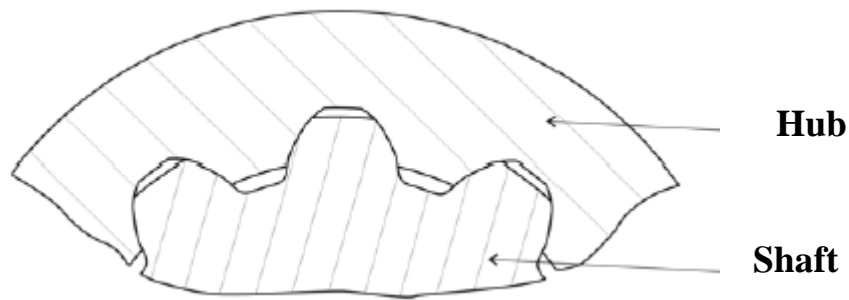


Figure 1.5 : representation of involute profile teeth [1]

Splined couplings with involute profile teeth have some advantages compared to those with parallel sides; as an example, they offer wider root fillet (Figure 1.5).

This type is normalized by the UNI ISO4156-85; this Standard provides the specifications related to the module range from 0.25 to 10, about nominal angle of pressure of 30°, 37.5° and 45°.

Splined couplings with involute profile teeth allow to manage high values of speed and torque.

d) *Crowned tooth splines:*

They are generally used when two shafts need to be connect and their axes may be misaligned.

So, they are designed to compensate an angular misalignment; in particular, two circular crowning are realized, one referring to the head of the teeth (curvature radius  $r_1$ ) and the other referring to the face width (curvature radius  $r_2$ ); these can be expressed by the following equations:

$$r_1 = 0.9 \times \frac{D}{2} \times \tan \Phi$$

$$r_2 = \frac{r_1}{\tan \Phi} = 0.9 \times \frac{D}{2}$$

where  $\Phi$  is the pressure angle [°] and D is the pitch diameter [mm].

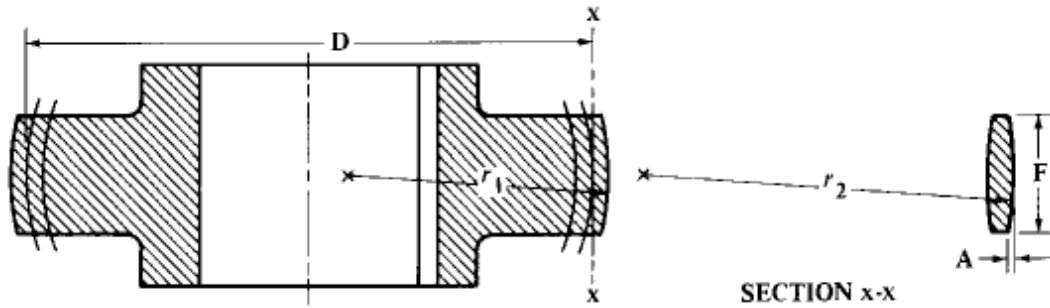


Figure 1.6: Representation of a crowned spline coupling [1]

### 1.2.2) Classification by type of centering

A second classification element for splined couplings is how the hub is centered regard to the shaft; three cases have to be taken into account:

- external centering: the centering is carried out on external diameter of the shaft; a small clearance on both sides and inner diameters is present;

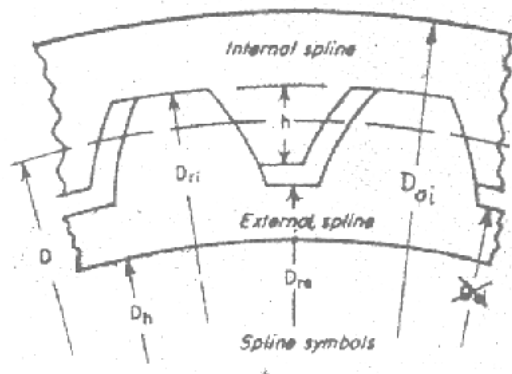


Figure 1.7 : external centering [1]

- sides centering: the centering is carried out on sides; a small clearance on external and inner diameters is left;

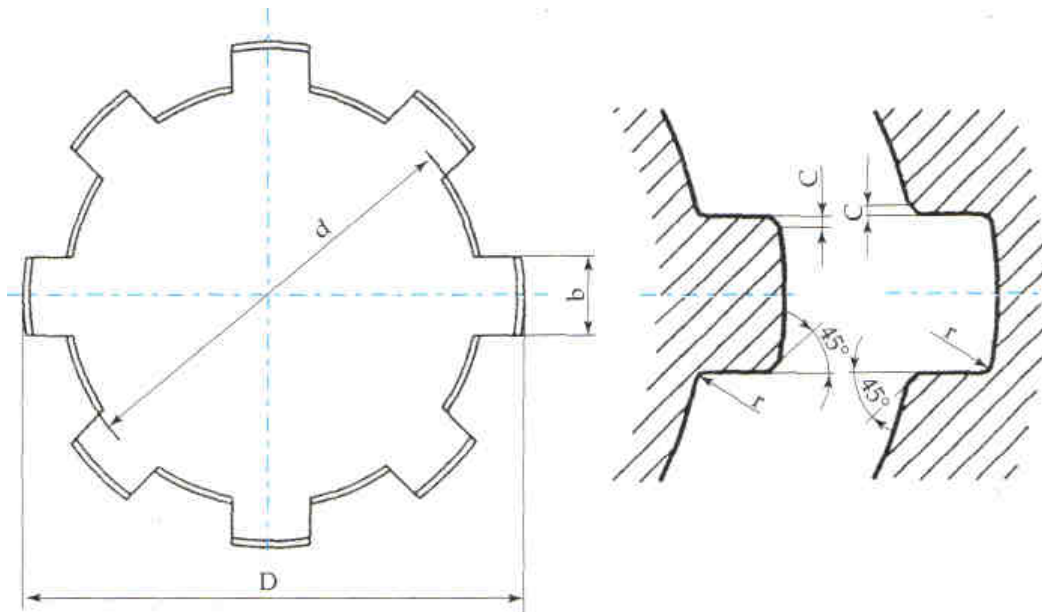


Figure 1.8. sides centering [1]

- inner centering: the centering is carried out on inner diameter; a small clearance on both sides and external diameters is present.

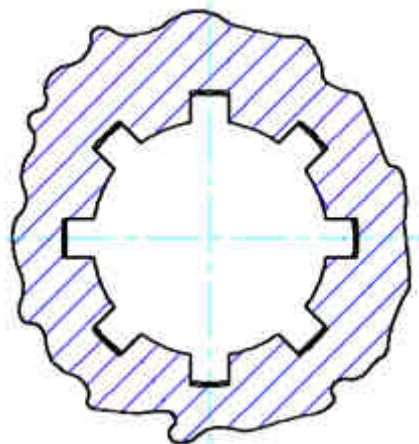


Figure 1.9: inner centering [1]

The various types of splined couplings are chosen depending on the type of the application. Concerning the use of three distinct types of centering, it may be observed that the most used conditions are the internal centering (for parallel side splines) and the side fit (for splines with involute flanks).

The inner centering has the advantage of the execution of grinding on cylindrical surfaces of both shaft and hub; the centering flanks is less

employed, being more expensive due to the increased difficulty of the surface flanks tooth grinding of the shaft and in particular of the hub execution.

A great attention may be paid to the grinding of centering surfaces in the cases of hardening treatment.

Regarding the splined couplings with involute flanks, the UNI ISO 4156-85 defines like centering the side fit, due to the high accuracy degree in the involute profiles cutting.

### 1.2.3) Classification of splined couplings with involute profile

Regarding the splines with involute profile, DUDLEY [3,7] in his papers distinguishes two types:

- fixed splines: they not allow any relative movement between external (shaft) and internal (the hub);
- flexible splines: they allow relative movements between the teeth of shaft and of hub, so that, due to the torque, the teeth may slide axially to permit a possible radial expansion or oscillation;
- crowned splines: they refer [3,7] to the particular case of high angular misalignment between shaft and hub.

## 1.3) TRADITIONAL METHODS TO DESIGN A SPLINE COUPLING

The traditional design methods for splined couplings may be found in two different types of bibliographic sources:

- texts of Machine Design,
- Standards Unification.

By reference to the Machine Design texts, in this chapter are presented the approaches described by Giovannozzi [2] and Niemann [5], while for the Standards Unification, are presented the calculation procedures described by both French [4] and American Standards [6].

Regarding the Giovannozzi's method, he considers three different type of spline coupling profile: radial straight sides, inclined straight sides and involute profile.

For the design of these three types of splined couplings, Giovannozzi proposes to equal the maximum transmissible torque by a solid shaft, with a diameter equal to the inner diameter of the spline shaft, with a formulation that takes into account the maximum tangential forces that each tooth can support; this formulation presents two correction coefficients: one takes into account the non-uniformity of the contact pressure distribution and the other one characterizes the type of the surface in contact [2].

Nimann [5] describes the maximum transmissible torque as the product of pressure and contact geometrical area; this torque acts on a percent number of teeth (75% for spline coupling realized with a precise machining and 90% with sides centering).

The French Standard [4] calculates the transmissible torque as the minimum values of three admissible torques due to different stresses (normal compression stress, shear stress on the shaft and shear stress on the hub).

In the American Standard [6], derived from the works of Dudley [3,7], the calculation procedure provides the evaluation of four types of stresses: shear torsion stresses at the root of the tooth shaft, shear stresses at the pitch diameter of the shaft tooth, normal compression stresses at the sides of the tooth shaft and bursting stresses of the hub.

The Dudley method is iterative: in fact firstly the entity of the various types of stresses has to be estimated; then if only one exceeds the value of the corresponding admissible value, the procedure has to be repeated until convergence to a correct solution, through the variation of the geometry of the spline coupling.

Dudley suggests some correction factors to be used before comparing the stresses value calculated with the permissible; through these correction factors are taken into account various events; as the type of load, the load

distribution, the fatigue (considering the number cycles that the component must do) and the wear (number of revolution) phenomena.

In all methods previously cited, the contact pressure distribution was considered as uniform both in radial and in axial direction.

Another approximation of the methods is the effective number of teeth in contact.

Moreover a phenomenon neglected in all design methods is the presence of wear and, in particular, the effect of fretting wear causing the decommissioning of these components (above all when high performance is required, as in aeroengine industry).

## CHAPTER 2: FRETTING WEAR PHENOMENA

### 2.1) INTRODUCTION

A study on fretting failure is important since the design life of a structure decreases if it suffers from fretting, which is widely found in the industry. Premature failure due to fretting is attributed to either rapid crack growth (fretting fatigue) or surface wear (fretting wear). Fretting wear usually refers to when the contacting structures suffer from contact stresses, which are exerted cyclically with small amplitude onto the contacting surfaces. A bulk fatigue loading is rarely incorporated in fretting wear, so surface wear rather than fatigue cracking is primarily brought into focus. The worn surface loosens the tightness of the couplings or the joints of a mechanical structure, which will result in a malfunction. If the wear proceeds severely, a catastrophic failure may happen. For example, a tube can be perforated due to the wear at the contact surface between it and its support.

Another examples is the fretting wear of ball bearings and fretting wear of gold plated rack and panel connectors when transported in assembled condition.

In fact, in accordance with Ratsimba et al. [8], fretting wear occurs commonly in clamped connections and demountable couplings, and involves surfaces in contact subjected to cyclic small amplitude relative displacements. It is distinguished from reciprocating sliding wear particularly with respect to the trapping of debris within the contact region and the nature of the sliding regime, which is often one of gross slip. The role of debris is critical in fretting wear; generally, once debris accumulates on the contacting surfaces and forms compacted oxide beds, the wear rate is reduced significantly [9,10]; but if the debris remain inside the contact region and there is lubrication, these uniting themselves create an abrasive paste which speeds up the wear phenomenon.

The difficulty of preventing fretting wear arises since cyclic contact stresses of a small amplitude are often inherent for almost all the mechanical structures during service.

During the service period, a vibration of the structure is usually inevitable, which results in cyclic tangential shear stress (slipping) on the contact. Normal stress may also be cyclic if there is a gap between the contacting bodies.

Even though there has been a lot of research on investigating, modeling and preventing fretting wear, it is still a difficult problem for designers and researchers to derive a general solution for wear. This is mainly because a lot of factors are related with the wear phenomenon. For instance, wear is affected by a combination of contacting materials, the environment, the loading conditions, the geometry of the contacting bodies, etc.

A number of authors, including Korovchinsky [11], Galin [12], Galin and Korovchinsky [13], Korovchinsky et al. [14], McColl et al. [15] and Ding et al. [16], have reported on fretting wear prediction methodologies based on the Archard wear equation [17], appropriate, immediately at least, to simple laboratory specimen configurations; inevitably round against-flat or flat-against-flat. However, a number of these approaches are also appropriate for extension to complex engineering assemblies.

Splined couplings are frequently cited as complex assemblies that experience fretting damage [18,19], that is, both wear and fatigue. The loading conditions that give rise to fretting wear, fretting fatigue or plain fatigue in such a coupling have been investigated by the present authors [20-22].

However, the number of publications that consider directly the fretting wear of these couplings is very limited. Ku and Valtierra [19] investigated the effect of design parameters, such as tooth crowning and angular misalignment, as well as the effects of lubrication, material type and surface treatment on general wear in splines. In particular this work highlighted that angular misalignments are the most significant parameters causing spline coupling wear.

Misalignments are typically attributed to manufacturing and installation errors and, more importantly, to dynamic operating conditions.

Using boundary element analysis, Olver et al. [23] attempted to make qualitative correlations between wear depth distribution computationally determined and the appearance of worn spline tooth flank surfaces.

For these reasons it is started this PhD thesis that has the purpose of realizing a new design method that, considering the effective number of teeth in contact and then the real contact pressure on them, is able to predict the presence of fretting wear in a complex component as the splined coupling.

This chapter reviews the current state of knowledge concerning fretting wear (FW). Firstly, a brief historical review of types of wear is conducted.

The subject of fretting is introduced, followed by the key analysis techniques that can be applied to the fretting problem.

## 2.2) TYPES OF WEAR

Wear is generally defined [24] as the progressive material removal from the surface of a solid that has a relative motion related to another solid or a fluid.

The most common types of wear are adhesive and abrasive.

A third type of wear is the corrosive one, in which the surface layer is cyclically corroded and removed by sliding, and after it comes back to form.

Last phenomenon classifiable as a wear phenomenon is called fretting, also known as fretting corrosion, which is classified as adhesive wear, but usually includes also characteristic aspects of abrasive and corrosive wear.

All forms of wear are greatly influenced by the presence of a lubricant.

### 2.2.1) Adhesive Wear

The surfaces of metallic materials are characterized by a certain degree of surface roughness; this range across a few microns (semifinished product) and tenths or hundredths of a micron (grinding, polishing and lapping).

The high contact pressure and local heat generated by the friction cause significant temperature increases in minor areas, this creates favorable conditions for forming microwelding.

However, since the action of motion continues, the welded areas are separated as a result of breakage.

The process, that continues cyclically with the formation and the subsequent breaking of welds or parts of the surrounding material, can deteriorate rapidly and irreversibly the component.

Given that the adhesive wear is essentially an expression of a localized welding phenomenon, turn out to be more prone to it weldable materials.

If the welding and breaking process of the surface asperities causes a metal transfer from one surface to another, the wear will also defines "scoring".

When the welding interested extended portions of the contacting surfaces in such a way as to reduce (or to prevent) the relative sliding, it speaks of "seizing".

A high adhesive wear is also called "galling". A moderate adhesive wear (for example between piston rings and cylinder liner) is defined as "scuffing".

In Figure 2.1 is shown a schematic representation of adhesive wear.

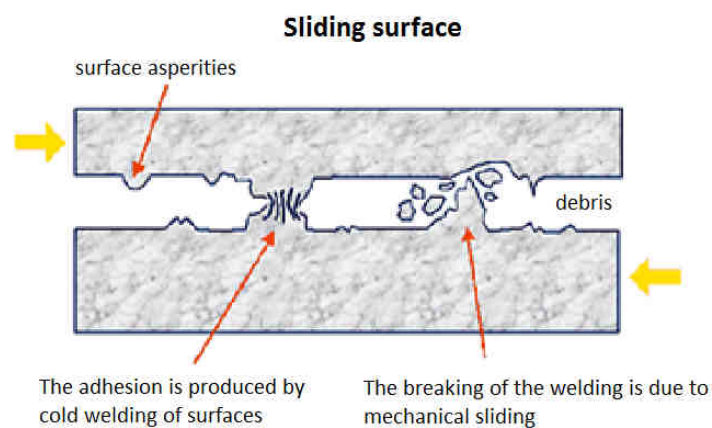


Figure 2.1: schematic representation of adhesive wear [25]

### 2.2.2) Abrasive Wear

Main feature abrasive wear is the presence of oxides that tend to scratch the contact surface and gives typically red rust color.

The oxidation of steel is essentially due to the effect of air or other substances containing oxygen; in addition to this phenomenon, it must be considered that also the lubricant used can decompose into harmful products that clog the filter by decreasing the correct dosage of oil.

In Figure 2.2 is shown a schematic representation of abrasive wear.

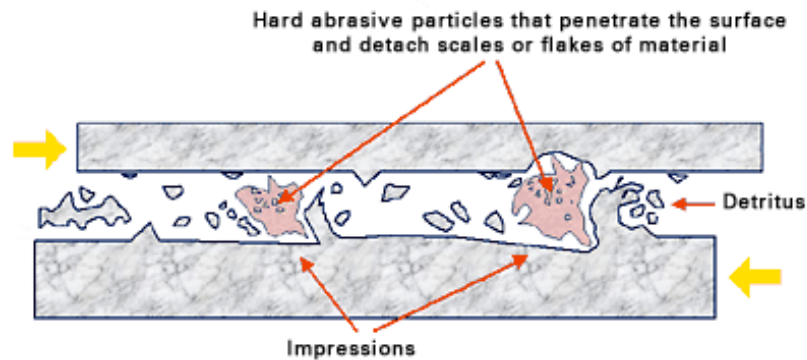


Figure 2.2: schematic representation of abrasive wear [25]

To prevent the formation of these abrasive substances it must be ensured a continuous and constant dosage of lubricant and it must be prevented the relative sliding between the components.

A possible solution can be the coating with substances such as silver, copper or nickel; thus doesn't eliminate the wear phenomenon, but it increases the operating life: in fact, the metal removal occurs only once it is removed the coating too.

As it can be seen in the Figure 2.3, it is possible to have four types of abrasive wear: *the cut* (I) is the first mechanism represented. The cut material is removed as wear debris and on the surface is observed many grooves generally pyramid or spherical shaped. Below the abraded surface there is a considerable plastic deformation, which leads to material hardening and thus a wear phenomenon reduction.

When the abraded material is fragile, for example a ceramic, it has the *fracture* (II) of the surface. In this case, the debris are the result of the advancement of cracks.

When a ductile material is subject to abrasion by particles without corners, cutting phenomena are disadvantaged and the abraded surface is subjected to *repetitive deformations* (III). In this case, the debris is the result of metals fatigue phenomena.

The final mechanism, *pull-out* (IV), is the detachment or the expulsion of the particles.

This mechanism is very common in ceramic materials where the grain boundary is relatively weak for which the phenomenon is very rapid. In this case, the whole grain becomes debris.

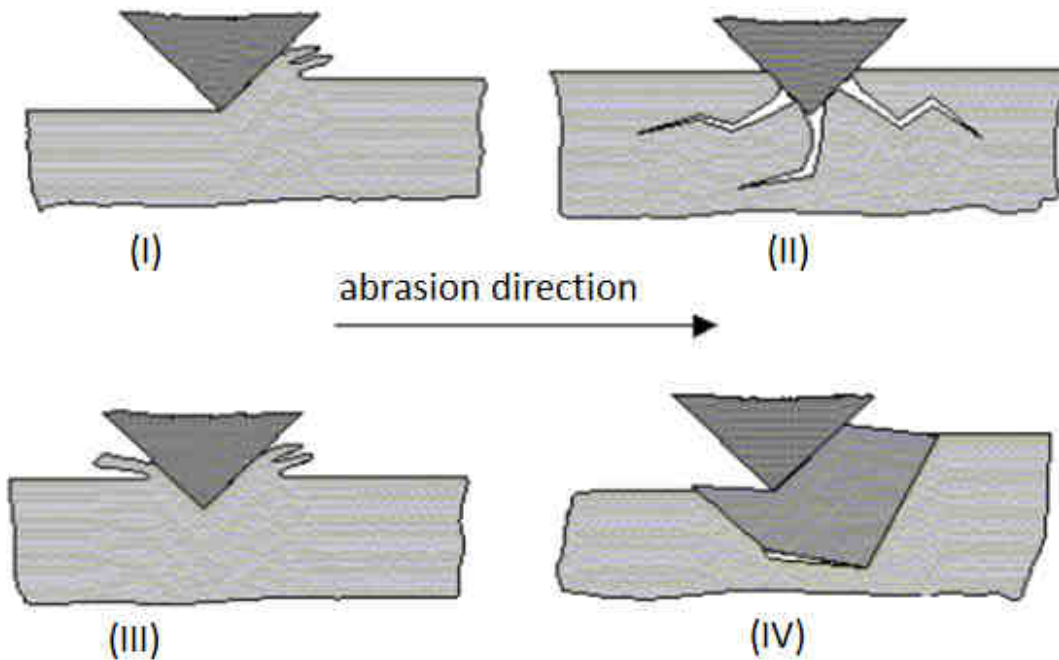


Figure 2.3: types of abrasive wear [24]

### 2.2.3) Fretting wear phenomenon

Fretting is defined as the small amplitude (typically 1-100  $\mu\text{m}$ ) oscillatory relative motion between two surfaces in contact.

The fretting is mainly a type of adhesive wear, but also includes aspects of abrasive corrosive wear: the wear occurs when two surfaces pressed one against the other are subject to relative movements of small amplitude.

The resulting damage may consist in a simple surfaces discoloration, in the formation of surface craters (the most common case) or in the removal of a considerable amount of material.

The oscillating movement causes the surface layers erosion, exposing new areas to the phenomena of welding and breaking parts.

The debris oxidizing give rise to very small abrasive particles (order of microns), which are deposited and cause the worsening of wear process.

Depending on the materials in contact resistance to fretting varies strongly.

This phenomenon is delayed when there is the presence of compression surface residual stresses.

The lubricants characterized by low viscosity and high strength tend to reduce the intensity of fretting because they maintain the oxygen away from the area of interface and generally they carry away the debris created by wear.

In some cases, the wear can be stopped by increasing the contact pressure in order to stop the relative movement; however, in the event that the movement continues, the damage from erosion usually will tend to increase with increasing pressure.

It is known that this phenomena occurs in many nominally static mechanical arrangements undergoing vibrations or cyclic stresses. The microslip causes damage to the surfaces and eventual failure is by means of fretting fatigue (catastrophic failure) or fretting wear (loss of fit).

The slip condition in fretting is often described as:

- complete stick,
- partial slip,
- full (gross) sliding.

Fretting was first observed in the grips of a plain fatigue test by Eden and Rose in 1911 [26]. The presence of fretting is often unexpected and causes reduction in life, emphasizing the importance of recognizing and avoiding the phenomenon for practical design cases. The understanding of fretting is complicated by the presence of friction at the contact interface.

#### 2.2.3.1) Effect of Friction in Fretting Wear

A metallic surface is not perfectly flat and increased magnification reveals the roughness of the surface profile. The individual surface protrusions are termed asperities. When two surfaces are brought into contact, the asperities

of the individual surfaces interact and junctions of contact are formed. This interaction creates a resistance to tangential motion and this force is termed 'friction'.

Leonardo da Vinci is credited as the first to attempt a systematic study of friction, with the investigations later rediscovered by Guillaume Amont.

The so-called laws of friction, formulated from empirical observations, are often stated as:

- the friction force is proportional to the normal load (Amont's 1st law),
- the friction force is independent of the apparent area of contact (Amont's 2nd law),
- the friction force is independent of the sliding velocity (Coulomb's law).

These 'laws' are not observed across all experimental conditions and were formulated for 'dry' conditions where no lubricant is applied.

Amont's 1st law leads to the relation:

$$F = \mu N \quad (\text{eq. 2.1})$$

where  $F$  is the friction force,  $N$  is the normal load and  $\mu$  is termed the coefficient of friction.

The coefficient of friction (COF) can vary widely between different material combinations, from as low as 0.001 to around 10 in a vacuum.

Most metals tested in air lie in the range 0.1 to 1.0 [27]. It has often been observed that the COF is greater under static ( $\mu_s$ ) than dynamic conditions ( $\mu_d$ ), but frequently found that  $\mu_d$  is essentially independent of sliding velocities for most practical situations encountered (Coulomb's law).

In addition to the commonly employed Coulomb friction law, different friction laws have been formulated and are detailed in [28].

It was initially believed that the frictional force principally arose from the interaction of asperities [29]. The Coulomb model describes the contact

between two surfaces with simplified wedge-shaped asperities, by applying a normal contact load and displacing the two surfaces relative to each other. The model indicates that the work done is fully recovered as the surfaces slide, inferring that no frictional force is generated if the model is followed exactly.

This leads to the conclusion that another mechanism is responsible for the generation of the frictional force. In metallic materials this is attributed to the plastic deformation experienced by the asperities, and is denoted  $F_{def}$ .

It has also been proven that adhesion between the two surfaces  $F_{adh}$ , caused by the inter-atomic forces contributes to the total friction force.

The groundbreaking work of Bowden and Tabor [30] offered a key explanation of the behavior of friction. They stated that the 'real' area of contact is significantly less than the apparent area. Their work, at first, seemed to be in discrepancy with Amonton's laws, but they showed that with an increase in normal load, a subsequent increase in the 'real' area of contact is obtained. This may be investigated by approximating the asperity contacts as cylindrical, with the assumption that asperities are usually blunt. This leads to the application of the mathematical theory of Hertzian contact that it will be explained in the later chapter.

Assuming plastic behavior of the asperities, the total real area of contact is found to be proportional to the normal load, thereby attaining approximate agreement with Amonton's laws.

By investigating the real area of asperity contact and assuming asperity failure is governed by the shear stress of the material, the contribution of the adhesion force, for conventionally processed metals, to the COF is approximated by [27]:

$$\mu_{adh} \sim 0.2 \quad (\text{eq. 2.2})$$

From an assumption of an idealized rigid conical asperity, the contribution of deformation processes is estimated by:

$$\mu = \cot(\alpha) \quad (\text{eq. 2.3})$$

where  $\alpha$  is defined in Figure 2.4 and is generally greater than  $80^\circ$ , giving  $\mu_{def} < 0.1$ .

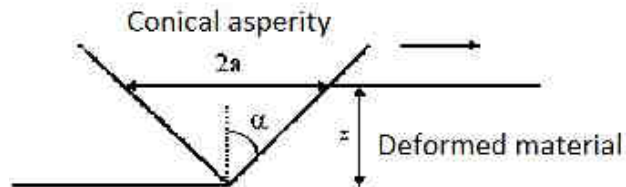


Figure 2.4: The model for the deformation component of friction, reproduced from [27].

This suggests that the total coefficient for two metals in sliding contact should not be around 0.3. It is usually observed that the experimentally estimated COF is significantly greater than this. Junction growth (dependence of real contact area on tangential load) and work hardening effects are thought to contribute to the discrepancy between the predicted and measured COF.

The COF is often difficult to quantify and its determination remains one of the biggest challenges in fretting research. Experimentally, it is commonly observed that the COF is initially low (as low as 0.1), followed by a rapid increase [31].

This is attributed to the beneficial (lubricating) surface layer films that are present during the initial stages of the test, which are quickly eliminated during the sliding motion, leading to metal-on-metal contact.

The initial sliding motion can also increase surface roughness, leading to an increased COF. The standard approach is to establish the bulk variables (friction force and normal load) by measurement or calculation. A complexity encountered is that, under partial slip conditions, the bulk approach is an approximation due to the presence of stick zones. One approach taken is to interrupt a test to determine the mean coefficient. This is

conducted by increasing the tangential force until full sliding occurs. From the mean value, the distribution of the COF was analytically determined for the Hertzian and rounded-flat cases [32]. An additional obstacle is that the local distribution of the COF will vary across the contact surface. This effect is usually neglected in the analysis of FW.

### 2.3) INVESTIGATION ON FRETTING WEAR

In the early period of fretting research, experimental data was extensively interpreted with the aid of S-N curves. Plain fatigue testing would be conducted and the subsequent fretting results compared. This allowed the determination of strength reduction ('knock-down') factors that quantified the effect of fretting on life. It was subsequently recognized that a significant number of variables affect fretting and that greater rigor was necessary for further understanding. It has been cited that as many as fifty variables can influence the fretting process [33], highlighting the complexity. It was suggested that the factors could be separated and that they can be categorized into primary and secondary sets of variables. The primary variables were listed as:

- contact pressure (normal load),
- coefficient of friction (COF),
- slip amplitude.

The secondary variables consist of factors that are arguably accounted for by their effect on the primary variables. These include: contact geometry, material, surface conditions (roughness, hardness, etc.), residual stress, temperature and test frequency amongst others.

#### 2.3.1) The methodology to quantify fretting damage

The methodology proposed to quantify fretting damage is subdivided into three following tasks:

- identification of the sliding conditions and quantification of the fretting regimes;

- analysis of a prediction model for the fretting wear;
- analysis of wear, focusing on surface roughness topography characterization.

This approach to fretting is focused on describing the contact behavior through intrinsic variables, which are respectively coefficient of friction, critical contact stresses and sliding of the contact area.

### 2.3.2) Sliding Analysis

Experiment and stress analysis show that it is necessary to well specify the various fretting loadings. The stress distributions in partial slip and gross slip are indeed different.

As described by Mindlin [34] for the sphere/plane contact, partial slip corresponds to a composite contact where a central stick domain is surrounded by a pulsing sliding annular domain. The contact behavior is then defined by a coupled elastic-sliding response inducing a hysteresis tangential force  $Q(t)$  versus displacement  $\delta(t)$  loop evolution [35, 36].

When gross slip occurs, the initial partial slip evolution is followed by a full sliding period. During this stage, the contact is characterized by a constant friction force associated with a pure dissipative behavior.

The tangential force  $Q(t)$  versus displacement  $\delta(t)$  loop presents a quadratic shape. The different domains of the sliding conditions are identified depending on the normal force and the displacements through the plotting of the sliding conditions are identified depending on the normal force and the displacements through the plotting of the sliding condition fretting map (Figure 2.5) [37, 38].

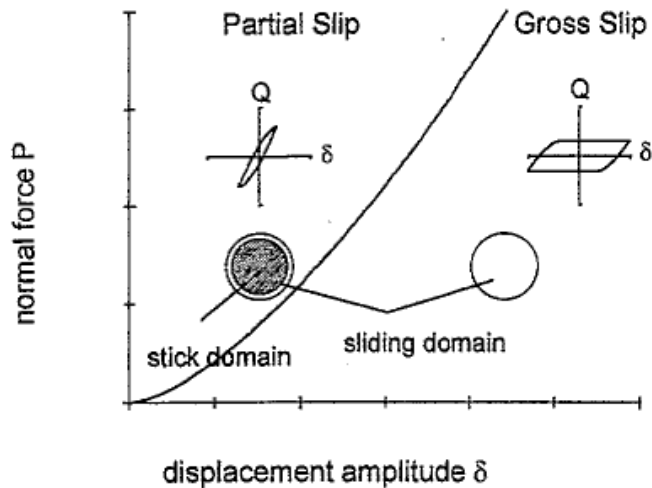


Figure 2.5: sliding condition fretting map [39]

As shown in Figure 2.6, assuming the Mindlin [34] fretting contact model, the tangential force amplitude, which controls the stress amplitudes and then the cracking process, strongly increases under partial slip until a maximum at the transition  $Q(t)$  which is maintained constant under gross slip.

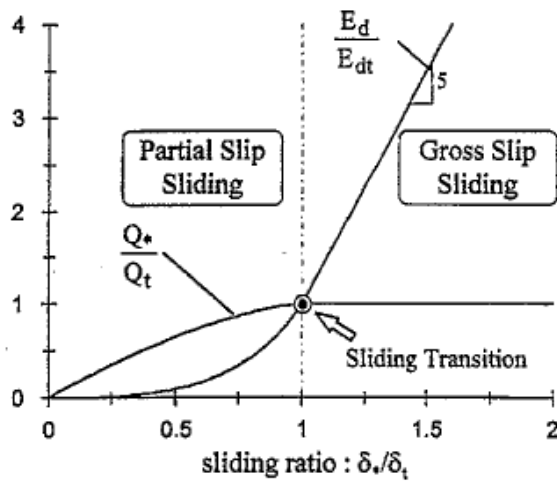


Figure 2.6: Evolution of the two ratios tangential force amplitude and the dissipated energy as a function of the sliding ratio [39]

On the other hand, the interfacial dissipated energy which is supposed to control matter removal is rather small under partial slip, displaying a curved evolution, whereas it presents a fast straight rise under gross slip conditions.

This basic observation is in total agreement with a large amount of experimental results where it was observed that the cracking process mainly evolved under partial slip before reaching a maximum risk next the transition.

Debris formation is essentially observed under gross slip.

### 2.3.3) Fretting Regimes

The subdivision into two fretting conditions (Figure 2.5) leads to three different fretting regimes when time evolution is considered (Figure 2.7): partial slip regime, gross slip regime (GSR) and mixed slip regime (MSR). [39, 40].

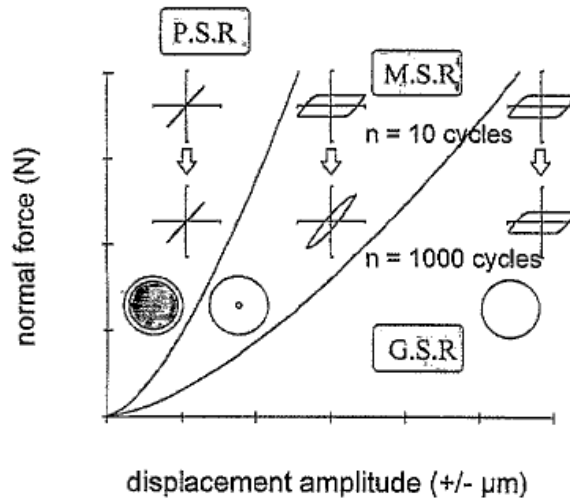


Figure 2.7: Normal force versus displacement amplitude regime map [39]

The most important thing to estimate is the boundary between sliding regimes, taking into account the tangential compliance of the system, the transition conditions  $\delta_t$  can be compared to the expression given by Mindlin [34] (Figure 2.8):

$$\delta_t = \mu P^{\frac{2}{3}} K_1 \left( \frac{4E}{3R} \right)^{\frac{1}{3}} \quad \text{eq 2.1}$$

$$\frac{1}{E} = \frac{1-\nu_1^2}{E_1} + \frac{1-\nu_2^2}{E_2} \quad \text{eq 2.2}$$

$$K_1 = \frac{3}{16} \left[ \frac{2-\nu_1}{G_1} + \frac{2-\nu_2}{G_2} \right] \quad \text{eq 2.3}$$

where  $\mu$  is the COF ;  $E_1, E_2$  are Young's elastic moduli of bodies in contact [GPa];  $\nu_1, \nu_2$  are Poisson's ration of the two bodies;  $G_1, G_2$  are the shear elastic moduli of bodies in contact [GPa];  $R$  is the curvature equivalent [mm] and  $P$  is the normal force [N].

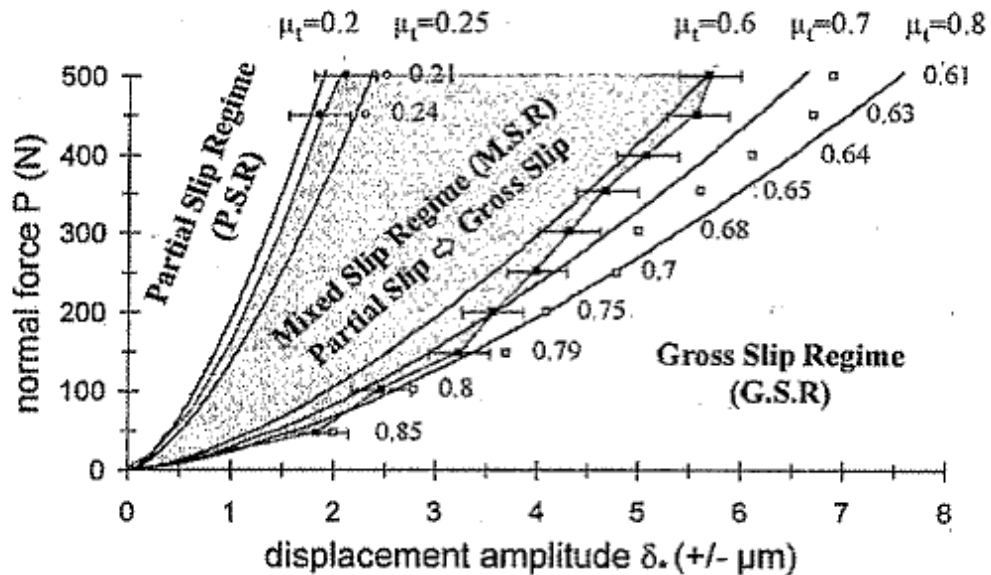


Figure 2.8: Example of fretting map applied on HSS vs alumina materials [39]

Observing what has just been described, it is essential to know, in order to study the phenomenon of fretting wear, the flow conditions that lead to have a phenomenon of gross slip.

For this reason it is set up a program that, once insert the metal characteristic in exam, gives the fretting map for it (Figure2.9)

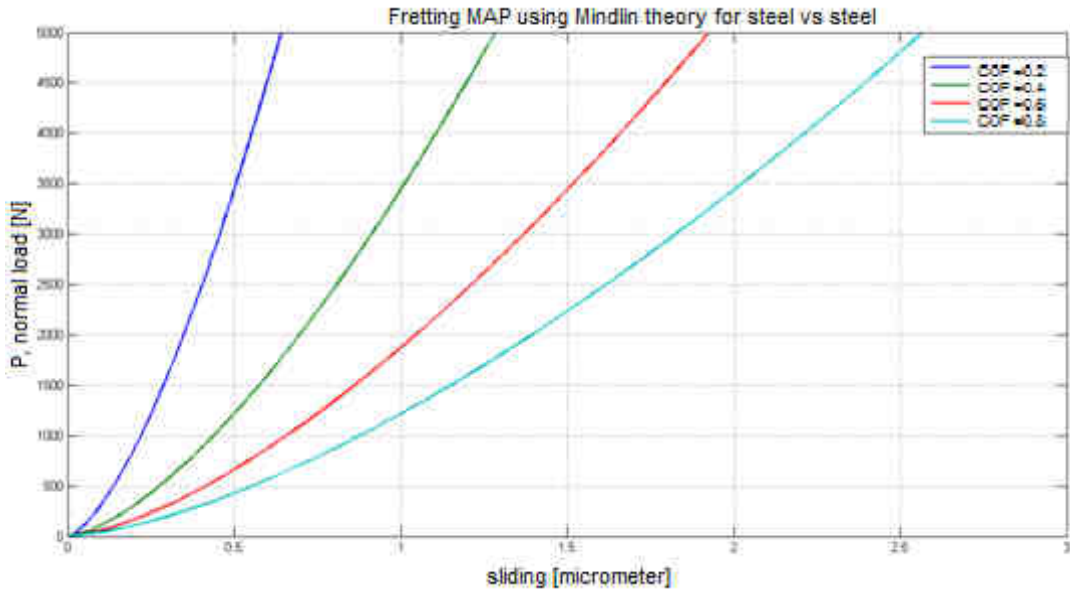


Figure 2.9: Fretting map for steel versus steel for different coefficient of friction values

Once achieved this fretting map (Figure 2.9) it was decided which misalignment the spline coupling test bench (that will be described later in detail) needed to manage in order to obtain the GSR.

Observing Figure 2.9 is simple to note that the value of sliding, considering a COF=0.3 and a normal load under 100 [N] (equal to have a 700 [Nm] of torque), is near 0.2 [ $\mu\text{m}$ ].

The Table 2.1 explains the correlation between misalignment and sliding of the contact area during a wear test on the test bench:

Misalignment [']	Sliding [ $\mu\text{m}$ ]
1	7.8
5	38
10	78

Table 2.1: values of sliding of the contact area during a wear test on the test bench

As can be seen, all sliding values on Table 2.1 are greater than those of Figure 2.9; this means that in all our tests done during this study the gross slip regime is found and therefore the spline coupling under fretting wear phenomenon has analyzed.

#### 2.4) FRETTING WEAR ON SPLINED COUPLINGS

Splines couplings are frequently employed in mechanical transmission systems for aeroengine applications because of their high specific torque transmission capacity and ability to tolerate some misalignment and movement [3].

Three spool high-bypass gas turbine aeroengines typically employ spline couplings to connect the low-pressure and intermediate-pressure turbine shafts to their corresponding fan and compressor shafts; also the transmission of torque within the gear box is guaranteed by these components. This suggests like the efficiency of the engine is correlated to the functioning of spline couplings.

The design and application of involute splines in aircraft power plants not only must consider the engineering properties of the metal employed, but also must provide for adequate lubrication to prevent serious wear problems. Splined connections can accommodate appreciable shaft misalignments; hence it is customary to use such connection when shaft misalignment is anticipated. However, when misalignment occurs, the resulting oscillatory relative motion between the engaged splines may result in significant wear damage.

For the small amplitude oscillatory motion normally associated with misaligned spline, the wear process appear to be 'fretting' dominated. That is, the amplitude of the relative motion is so small that wear debris is retained between the surfaces which are exposed to the contact stresses.

Splined couplings are frequently cited as complex assemblies that experience fretting damage [41, 42], both wear and fatigue. The loading conditions that

may rise to fretting wear, fretting fatigue or fatigue in such a coupling have been investigated by the present authors [43–45].

The fatigue behavior of spline couplings has been the subject of a number of studies [20, 21, 43, 44], with three prominent sources of stress concentration; spline root/fillet torsional stresses, spline fillet bending stresses and friction enhanced contact stresses [44]. To improve the fatigue performance, spline profile (tooth thickness) modification by axial barreling/crowning has been employed in order to reduce the end-of-engagement contact stresses [47, 48]; however, this further increases the complexity of the analysis due to the dependence of the spline tooth contact area on torque level.

Fretting wear is typically more gradual and progressive, compared with the above-mentioned fatigue failures. However, it can significantly add to the maintenance cost of an aeroengine. The fretting wear of spline couplings has received limited attention with studies initially concentrating on the wear and friction of straight flat sided splines [49-51].

Afterward Medina and Olver [52] carried out fretting tests on model splines with different surface treatments and coatings.

More recently, Ratsimba et al. [8] reported on a methodology to predict the fretting wear of a spline coupling subjected to cyclic torque, cyclic axial load and rotating bending moment.

Spline couplings involve complex geometries and loading regimes, ensuring that the prediction of stress (and slip) distributions in such assemblies is not straightforward; consequently, early studies were generally restricted to torsion-only loads [3, 8, 53].

However, extensive testing of ‘simple’ fretting geometries, such as cylinder-on-flat, flat-on-flat and crossed-cylinders has been carried out [52, 53], and the main parameters affecting fretting wear found to be contact load, slip amplitude, frequency, contact geometry, surface roughness and material properties [10,54].

During the last decade the extension of numerical methods to contact problems involving friction made possible to predict the surface and

subsurface stresses on the spline teeth under general loads, and to determine contact pressure and slip distributions across the contacting spline surfaces. The “fretting map” approach showed previously confirms that fretting damage evolution depends strongly on the fretting regime [37, 55]. Debris is also a critical factor influencing fretting wear.

## CHAPTER 3: FRETTING WEAR MODELLING APPROACH

### 3.1) INTRODUCTION

Due to the great need of industry to prevent fretting damage, fretting wear and fretting fatigue have been widely studied for more than twenty years [10, 55, 56]. Thanks to the fretting mapping approach [37,38], fretting wear and fretting fatigue are now both recognized to be at the origin of the two main mechanisms of damage, wear associated with particle detachment and crack nucleation and propagation, which can lead to failure of parts.

Palliatives have been analyzed both theoretically and experimentally [55, 57, 58]. Soft and hard coatings were shown to be possible palliatives, depending on the tribosystem.

Even if some understanding now exist to explain why a coating can prevent or diminish fretting damage, it is still very difficult to propose guidelines for material or coating selection and to predict and quantify wear and cracking.

Fretting resistance cannot be considered as an intrinsic property of a material, or even of a material couple. Recognizing that fretting can induce material loss (wear) or deep cracking, it is obvious that these two types of damage cannot be interpreted in terms of the same properties of the bodies. Wear induced by cracking is clearly identified as the response of materials to global overstraining of the surface, while cracking induced by fretting usually appears as the consequence of local overstressing [59]. These two kind of loading (overstraining and overstressing) can appear in a vibrational contact. For instance, depending on the amplitude of the displacement or on the normal load, the fretting conditions can be partial slip or gross slip. These two situations do not induce the same local loading of the surface. Moreover, depending on the amplitude of the displacement, the environmental atmosphere may be suspected of having a different effect.

Many analyses have dealt with crack phenomena, but only in the case of fretting fatigue. However, it is to be kept in mind that fatigue cracking is related to two types of fretting. In the same way the question now arises about the specificity of fretting in the wear analysis.

This work is concerned with identifying convenient tools to firstly detect the nature of the local condition and then to quantify the risk of material loss.

### 3.2) FRETTING WEAR MODELLING APPROACH

The development of a fretting wear model for a spline coupling or other coupling subjected to a complex loading regime requires the integration of a number of 'tools'. However, if successful, in addition to the prediction of fretting wear and concomitant service life, such an approach would enable the evolution of contact geometry and the associated fatigue pertinent stresses to be predicted.

The tools required for such an approach are:

- (i) a detailed geometrical model of the coupling;
- (ii) knowledge of how the coefficient of friction changes with distance slid (in this study it is considered constant and equal to 0.3 on first approximation);
- (iii) a solver to calculate the contact pressure and then the stresses;
- (iv) a solver to calculate the slip distributions during a complete rotation of the spline coupling;
- (v) an algorithm to predict the wear and its direction.

### 3.3) SPLINED COUPLINGS ANALYTICAL MODEL

The currently design methods available in literature take into account the static and fatigue failures, with regard to the wear, only the Dudley method [3] takes this into account, but roughly.

Several factors influence the duration and, therefore, the dimensioning of splined couplings: the type of load, lubrication, rotational speed, etc., but the most important is the number of teeth in contact that actually contribute to load transmission.

Ideally, the load that must be transmitted by a splined coupling is distributed uniformly on all component teeth; in practice, only a part of them is in contact and transmits torque and this is due to machining tolerances and relative production and mounting errors.

Previously, it isn't easy to be able to calculate the actually teeth number in contact and traditional design methods suggest a predetermined number of that, in general, vary from 50% to 75% [2-5] depending on the spline coupling and the applied load type.

In a recent paper [60], a statistical method for the determination of the actual teeth number in contact has been proposed.

It is clear that knowing the real load distribution between the teeth is the most important information to be able to correctly size and/or to verify these components.

In fact, the load distribution on teeth doesn't only affect static and fatigue behavior of these, but also affects the wear phenomena.

For these reasons it was created a two-dimensional model that has the purpose of calculating the effective contact teeth number and the forces distribution between the teeth knowing the machining and assembly tolerances of the spline coupling.

The computational code was validated by comparison with FEM models.

### 3.3.1) Superspline program calculation description

The new calculation code, called SUPERSPLINE, must allow a better spline coupling sizing than the methods currently used, optimizing the design and avoiding unnecessary over dimensioning.

The calculation program described below is proposed to determine the actual teeth number in contact, knowing in advance the machining and the assembly tolerances of the components.

In this discussion is taken into account the tolerance of parallel offset that is a concentricity error between shaft and hub rotating axes and which can be determined by construction or mounting errors.

The calculation program developed is divided into three main modules:

1. GEOSPLINE
2. STRASPLINE
3. ITERSPLINE

The module GEOSPLINE is a subroutine that graphically represents the spline and calculating the clearance between the teeth, the teeth sequence engagement and the rays on the teeth of the forces applied.

The module STRASPLINE performs the teeth deformation calculation (and therefore the calculation of their rigidity) discretizing the tooth into parts and representing it as a fixed beam.

The module ITERSPLINE is the central part of the program and allows to calculate the number of teeth in contact and the forces exchanged between the teeth through an iterative procedure.

Figure 3.1 shows the flowchart of the computational code SUPERSPLINE.

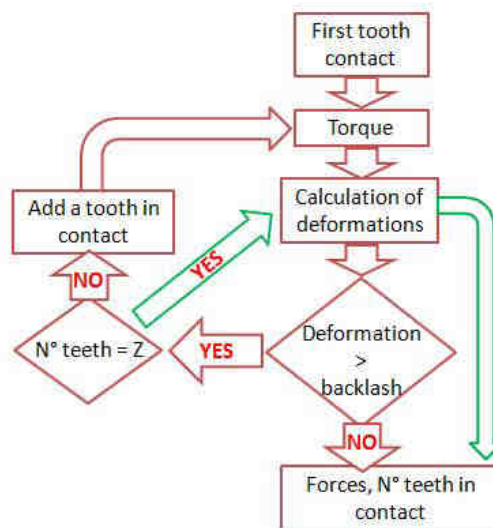


Figure 3.1: SUPERSPLINE flowchart

### 3.3.1.1) Geometric sub-program (GEOSPLINE)

The geometric calculation program (GEOSPLINE) is used to define the geometry of the spline coupling analyzed by inserting the geometric characteristics and the tolerance of itself.

The function of this module is not only graphics, but it allows to calculate the clearance between the spline coupling teeth which will allow the determination of the teeth deformation and therefore the number of teeth in contact.

The spline coupling geometry is automatically generated giving main dimensions (form, diameter, etc. ..), the scaling and tolerances like input. It is also possible the inputting of the fillet radii at the tooth root.

The first step in the geometry generation is the design of involute profile of the ideal shaft and the ideal hub (no clearance) and the design of the inside, the outside and the bottom of the tooth diameters (Figure 3.2).

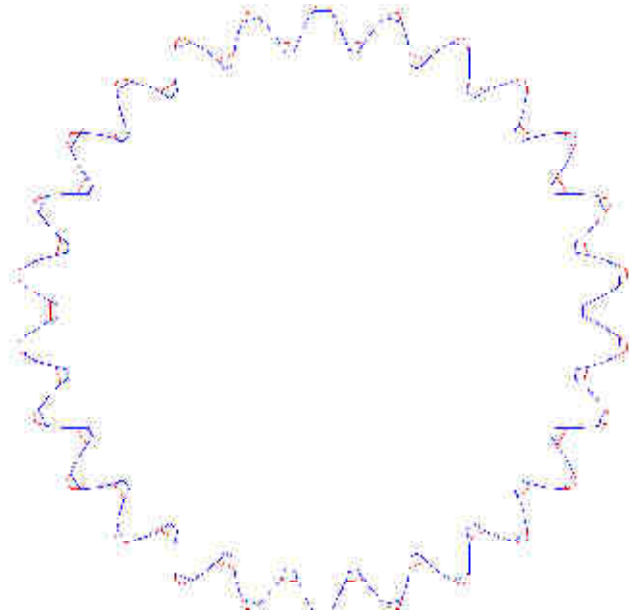


Figure 3.2: Representation of the shaft and the hub teeth in nominal conditions.

Following, clearance between the teeth is created by rotating the tooth profile around the center of the spline coupling (Figure 3.3), so as to obtain the value of the clearance set, which consists in a linearly clearance measured on the point of the involute at the pitch diameter.

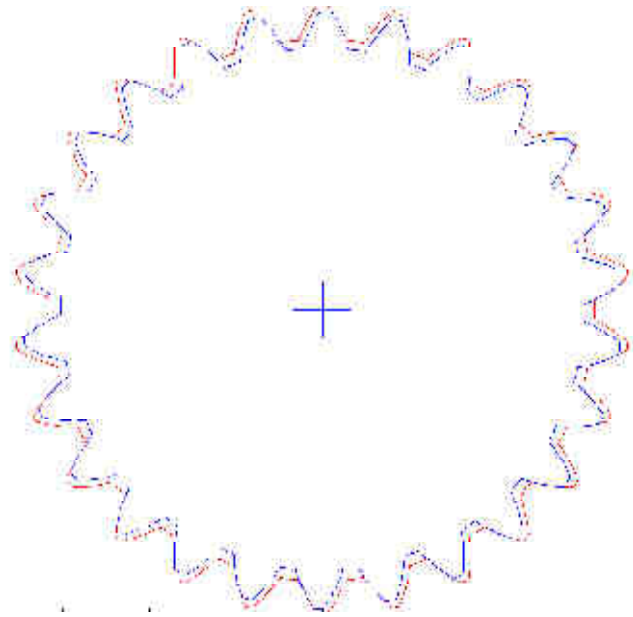


Figure 3.3: Teeth clearance input.

Following the shaft is moved respect to the hub in order to obtain the parallel offset error (which has been set in the input data) (Figure 3.4).

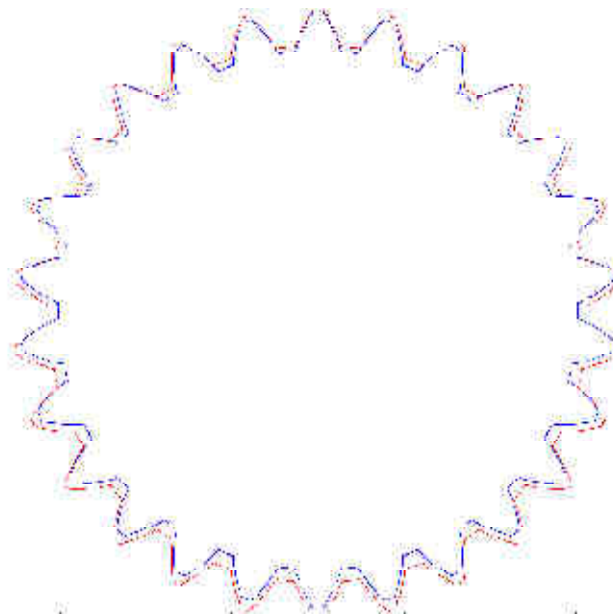


Figure 3.4: parallel offset input

The next step is the points identification, on the involute, of each tooth that are in contact (Figure 3.5).

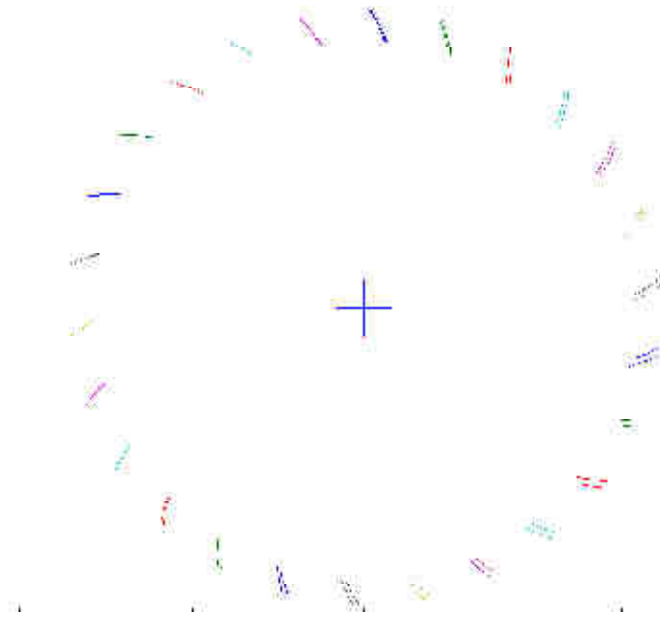


Figure 3.5: Identification of the involutes points on the shaft and on the hub that may come into contact.

From these points the clearance between the teeth is calculated (Figure 3.6).

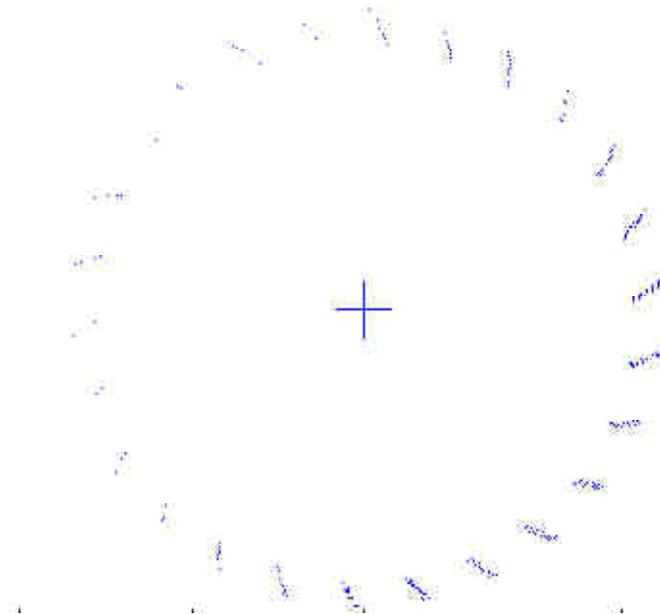


Figure 3.6: Clearance calculation between the teeth along the involute side.

Then the first pair of teeth in contact is identified, after that the teeth engagement sequence is obtained and the points of contact between the teeth is calculated and, therefore, the rays of force application (Figure 3.7).

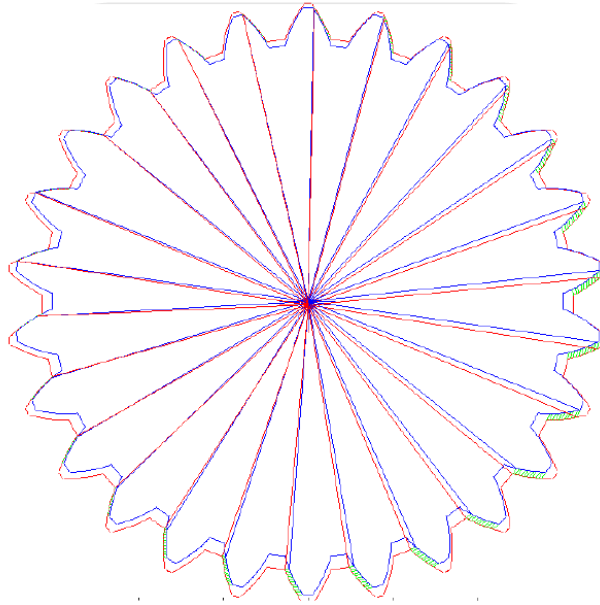


Figure 3.7 : Rays of force application.

The GEOSPLINE module also allows the fillet radii integration at the tooth bottom of the shaft and of the hub. It is possible, according to the geometric dimensions put into the program, to obtain different fitting configurations (Figure 3.8 and 3.9).

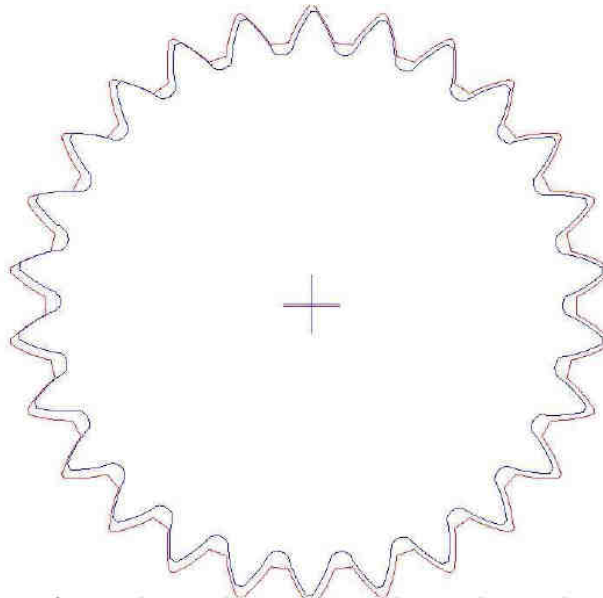


Figure 3.8: Spline coupling with fittings at teeth root.

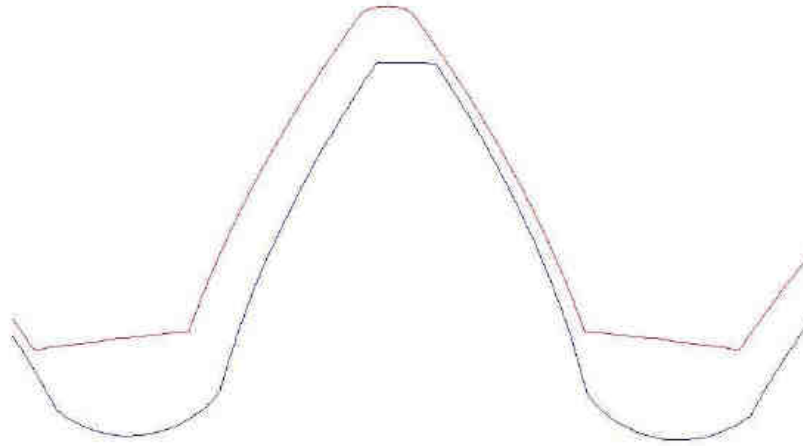


Figure 3.9: Fittings detail at the teeth root.

The outputs of the GEOSPLINE module are: the teeth clearances, the contact rays, the engagement sequence and the individual thicknesses slices in which the teeth will be discretized.

#### 3.3.1.2) Teeth deflections sub-program (STRASPLINE)

The module STRASPLINE allows to calculate the deformation and, therefore, the teeth bending stiffness.

Teeth deformation has been calculated considering the tooth as a cantilever beam and it is discretized into slices and it is loaded by a concentrated force at the bottom.

In the literature works the teeth stiffness [4, 61, 62], is calculated considering bending, shear and compression. In [61] and [62] is also taken into account the stiffness of the constraint.

In the works above, the contact force exchanged between the spline teeth is considered applied along the straight line of action, as in the case of the gear.

In Figure 3.10 are shown, by example, two gear teeth in contact: the force exchanged between them acts along the pressure line and it can be shifted until it intersects the tooth centerline.

If the contact is considered in the center of instantaneous rotation, the strength is inclined to the tooth centerline by the pressure angle, and it can be decomposed into its tangential ( $F_t$ ) and radial ( $F_r$ ) components.

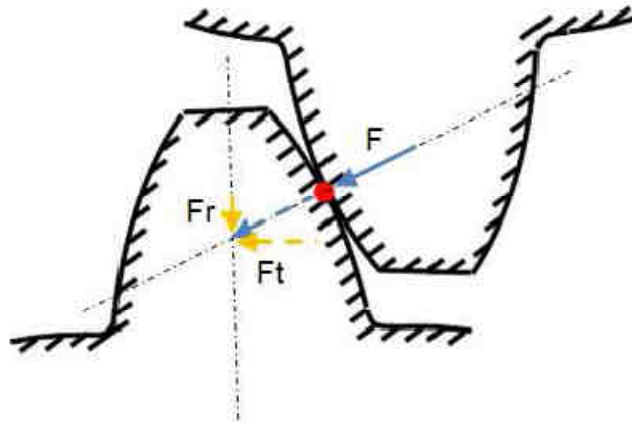


Figure 3.10: Contact force exchanged between the teeth of two wheels [63]

The splined coupling with involute teeth profile can be thought of as gear, but they are fundamentally different to them, not so much for the geometrical construction parameters, but rather for the coupling mode.

In fact, in the splined couplings case, theoretically all teeth are simultaneously engaged and the contact between them is always present during the rotation of the shaft;

Moreover, the contact area between the teeth is not a limited area (ideally a line along the face width), but is a larger area which includes the entire length of the involute in contact (Figure 3.11).

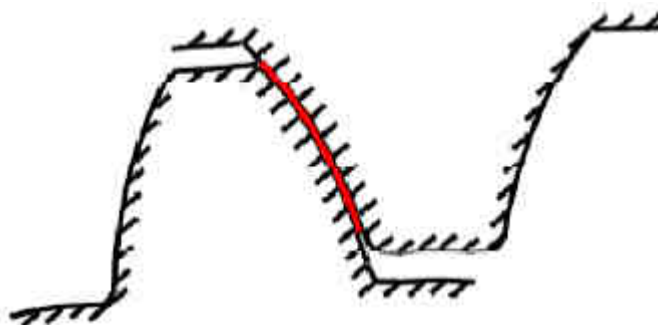


Figure 3.11: Splined coupling teeth contact area [63]

This makes that the force exchanged between the splined coupling teeth doesn't act along a pressure line, but it must necessarily obtain the point of the resulting application [64].

The resulting of contact pressure between the teeth and the relative point of application depend on the contact pressure distribution and, therefore, by the tooth stiffness itself.

In this work, as a first approximation, has been considered as the application point of the force resultant a contact point on the involute in correspondence of the pitch diameter [64], as shown in Figure 3.12.

The mathematical formulation was developed by Curà et al. [65].

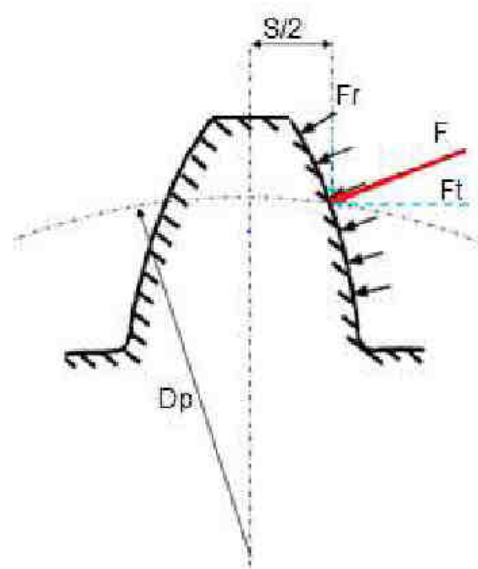


Figure 3.12: Scheme of the contact force exchanged between the teeth of a splined coupling [63]

### 3.3.1.3) Number of teeth in contact sub-program (ITERSPLINE)

The actual number of engaging teeth and the corresponding load sharing is calculated by means of an iterative process. This recursive logic can be easily explained with reference to the flow chart shown in Figure 3.1 where Z is the total number of teeth.

At the beginning of the iterative process only one pair of teeth is in contact, the corresponding load value is applied and the teeth deformation is calculated; if the deformation is higher than the circular gap required for a new pair of teeth to get in contact (gap between teeth and engagement order in unloaded condition have been previously calculated with the dedicated subroutine described previously), the new deformation is again calculated,

together with the number of engaged teeth. The algorithm proceeds until the total external torque is balanced and no further teeth get in contact due to loaded teeth deflections.

At the end of the recursive process, the actual number of engaging teeth and the corresponding applied load is obtained.

### 3.3.2) Validation Code

This paragraph describes the tests performed for validate the analytical models developed and previously analyzed.

#### 3.3.2.1) Convergence of method

As first thing it is tried to find an acceptable tooth discretization value.

For doing this, the tooth was discretized with different values of slides; and in particular the slides values are: 5, 10, 50, 100, 200, 500, 1000, 2000, 3000, 4000, 5000 e 10000.

Obviously these results shall be obtained with the same Young's modulus, Poisson coefficient, load conditions and with the same geometry.

METHODS	CORNELL			POLITECNICO			Constant section beam			
	Slides number	Shear [mm]	Bending [mm]	Tot [mm]	Shear [mm]	Bending [mm]	Tot [mm]	Shear [mm]	Bending [mm]	Tot [mm]
	2	2.87E-04	4.34E-05	3.31E-04	2.81E-04	0.00E+00	2.81E-04	2.34E-04	9.12E-05	3.25E-04
	5	3.23E-04	7.51E-05	3.98E-04	3.22E-04	4.95E-05	3.71E-04	2.34E-04	9.12E-05	3.25E-04
	10	3.40E-04	1.10E-04	4.49E-04	3.39E-04	4.51E-05	3.84E-04	2.34E-04	9.12E-05	3.25E-04
	50	3.56E-04	1.55E-04	5.11E-04	3.54E-04	2.67E-04	6.21E-04	2.34E-04	9.12E-05	3.25E-04
	100	3.58E-04	1.63E-04	5.21E-04	3.56E-04	3.11E-04	6.67E-04	2.34E-04	9.12E-05	3.25E-04
	500	3.60E-04	1.69E-04	5.29E-04	3.57E-04	3.50E-04	7.07E-04	2.34E-04	9.12E-05	3.25E-04
	1000	3.60E-04	1.70E-04	5.30E-04	3.58E-04	3.55E-04	7.13E-04	2.34E-04	9.12E-05	3.25E-04
	5000	3.60E-04	1.71E-04	5.31E-04	3.58E-04	3.59E-04	7.17E-04	2.34E-04	9.12E-05	3.25E-04
	10000	3.60E-04	1.71E-04	5.31E-04	3.58E-04	3.60E-04	7.17E-04	2.34E-04	9.12E-05	3.25E-04

Table 3.1: Convergence analysis of analytical models

From the results shown in Table 3.1 it can be seen that the model converges to a result asymptotic from 1000 subdivisions.

#### 3.3.2.2) FEM models

This section will describe the various steps that have led to the 2D model creation on which the FEM analysis were carried out.

In particular the analyzes were made on 1000-3000-5000 [Nm] load cases and under nominal alignment conditions.

MSC. Marc, that is a nonlinear implicit FEM solver, was the solver used and it was chosen for this case by the numerous contacts present in the model.

MSC. Patran was the graphic interface used.

Spline coupling geometry:

The spline coupling tested has been designed by Avio SpA Group

Table 3.2 summarizes the characteristic data of the spline coupling adopted.

	<b>HUB</b>	<b>SHAFT</b>
<b>Teeth number</b>	26	26
<b>Centering</b>	On sides	On sides
<b>Pressure angle [°]</b>	30	30
<b>Pitch diameter [mm]</b>	33.02	33.02
<b>Base diameter [mm]</b>	28.596	28.596
<b>Outside diameter [mm]</b>	35.281-35.789	34.595-34.722
<b>Start involute diameter [mm]</b>	34.874	31.166
<b>Inner diameter [mm]</b>	31.318-31.445	29.972-30.48
<b>Circular thickness [mm]</b>	1.994-2.068	1.886
<b>Face width [mm]</b>	25	25

Table 3.2: Design data of splined coupling

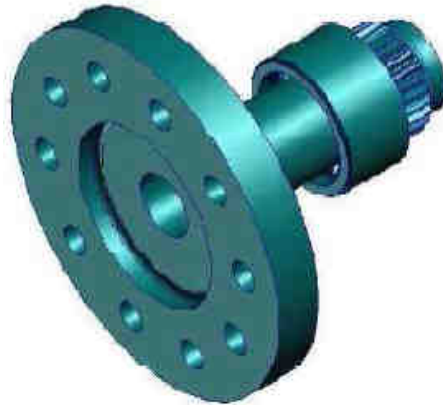


Figure 3.13: Internal spline coupling (shaft)

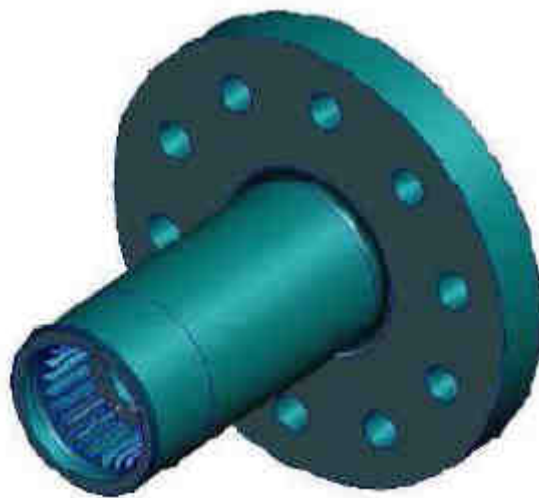


Figure 3.14: External spline coupling (hub)

It was obtained a 2D section of the spline coupling at the half-face width. This slice, which is shown below, represents the starting point of the FEM analysis.

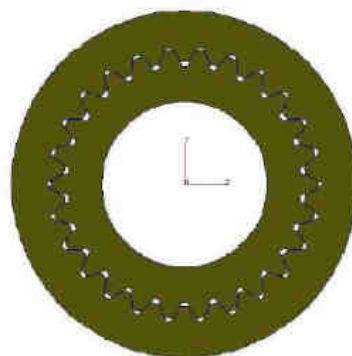


Figure 3.15: Spline coupling slice

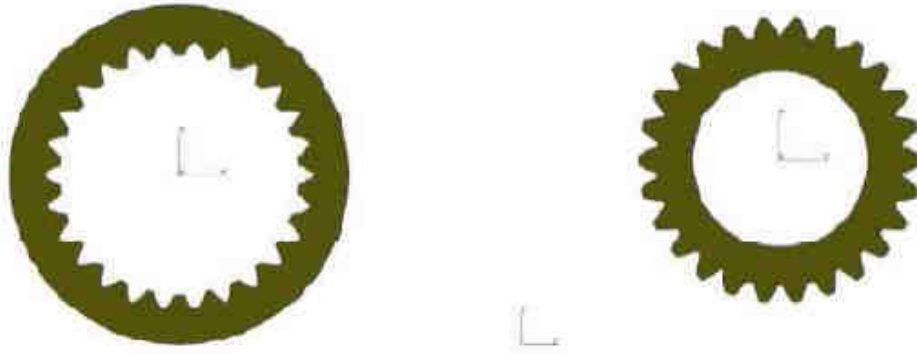


Figure 3.16: Hub (left) and shaft (right) sections

Subsequently it has been obtained, always with the CAD aid, a circular sector corresponding to the half tooth and to the half vain respectively for the external and the internal spline coupling.

It was decided to carry out the mesh of the half tooth in order to have a full symmetrical mesh.

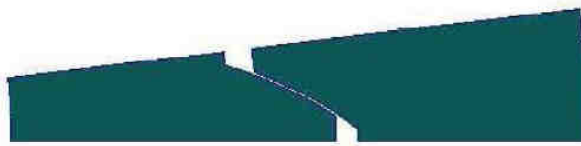


Figure 3.17: Circular sector used for meshing

### 3.3.2.3) Mesh creation

The circular sector, described in the paragraph above, was used as the basis for obtaining the mesh of the whole 2D model, as shown in Figure 3.18.

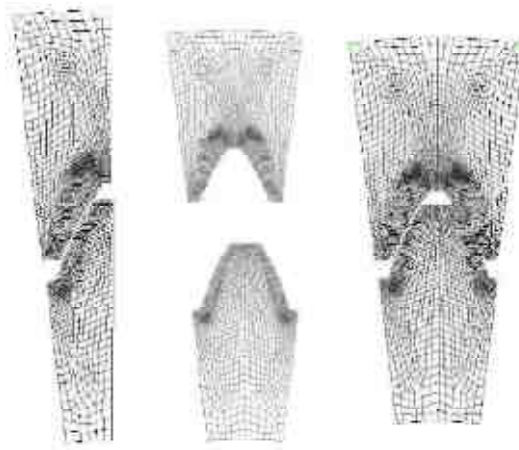


Figure 3.18: Spline coupling tooth mesh

As shown, it was decided to adopt a finer grid at the tooth sides and sparser to get away from it. This decision is a good compromise in terms of accuracy of the results and use of resources. In fact, a finer grid over the model has led to excessive computation time without value-added results.

The next step was to rotate the circular sector, previously obtained, in order to get the splined coupling completely modeled.

It is essential to mention that not using the 2D model like commencing section allowed to have a symmetrical mesh for the single tooth and, beside it, to have equal meshes for each teeth.

In this way, it becomes much easier to compare the FEM results with those of analytical models because the latter are obtained on the single tooth.

In the Figure 3.19 is shown the images relating to the splined couplings meshes.

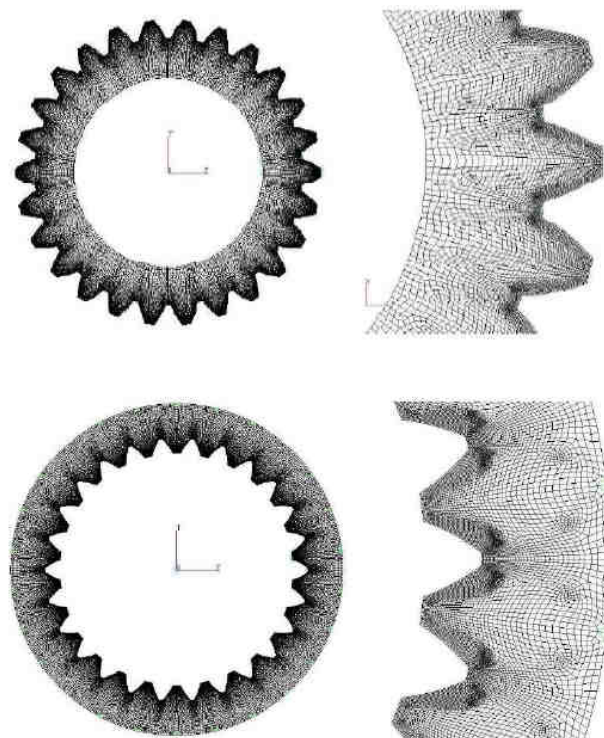


Figure 3.19: Images of splined couplings meshes

#### 3.3.2.4) Material properties

In this paragraph and in the corresponding sub-sections are described steps taken to define the 2D solid properties. In particular are defined:

- material and his properties
- elements' properties

For material properties are considered essentially the modulus of elasticity, Poisson's ratio and the density. The properties included in the model are those reported in Table 3.3.

<b>Young's modulus</b>	206000 [MPa]
<b>Poisson's ratio</b>	0.3
<b>Density</b>	$7.85 \cdot 10^{-6}$ [Kg/mm <sup>3</sup> ]

Table 3.3: Model's properties

The definition of this property is very important for reliability of the results and in particular with regard to two-dimensional analysis.

In fact, while for 3D models you can define only the sets of elements as 3D solid, for two-dimensional models, there are two possible options: shell property and Plain Strain.

For the this analysis is used the second case, because the 2D model analyzed is a section of a three-dimensional solid; using instead the first option you consider the model as a three-dimensional shell element.

### 3.3.2.5) Constraint definition

Considering our model it was decided to take on a tangential constrain on internal spline because it is more suitable to simulate a resistive torque, Figure 3.20.

It was decided, instead, not to constrain the radial displacement in order to allow a kind of spline ovalization; in this way it is simulated as close as possible the real case.

In order to obtain a tangential constraint, it is created a local cylindrical system of reference.

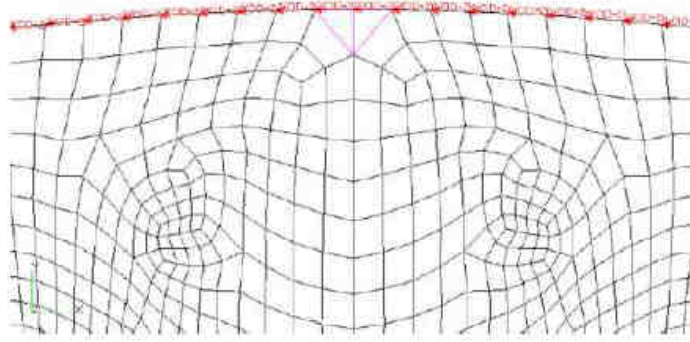


Figure 3.20: Tangential constrains

However, this condition of constraint was later modified to be able to compare the FEM results with those of the analytical model.

In fact, as a constraint condition of fixed joint is used and, therefore, it was decided to compare it with a model that does not permit the radial displacements.

#### 3.3.2.6) Definition of contact conditions

As regards the contact instead, the software needs input regarding the bodies which can be rigid or deformable.

The ideal condition is one where the contact bodies are defined by all the elements constituting the solid in question.

However, because of the very high number of elements and nodes, it was opted for a lighter solution from the computational point of view; in fact, have been taken only the constituent elements of the involute profiles, that are the elements that really participate in the contact (Figure 3.21).

Both bodies were defined as deformable.

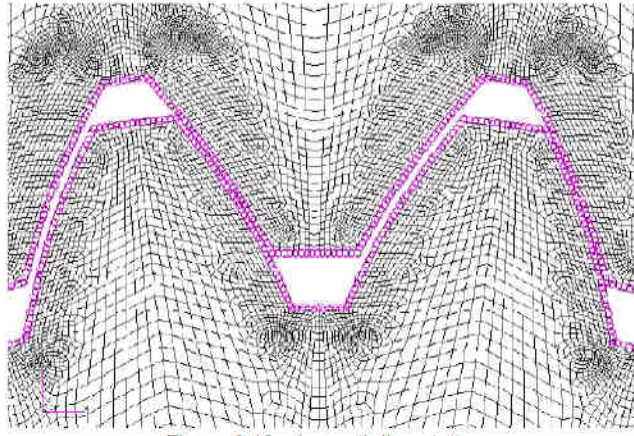


Figure 3.21: Elements in contact

### 3.3.2.7) Load definition

The splined coupling is designed to work in 3 different load conditions, that are: 1000 - 3000 - 5000 Nm.

Torque has been defined as a tangential forces system acting on the nodes of the pitch diameter.

Are shown below the values of the tangential forces applied to the nodes (Table 3.4) and some pictures related to the load of 1000 Nm.

Torque [Nm]	Tangential Force [N]
1000	93.18
3000	279.55
5000	465.92

Table 3.4: Tangential forces

To obtain the value of the force was applied to the following equation:

$$F_t = \frac{C}{R_p n b} 1000 \quad (\text{eq. 3.1})$$

where  $F_t$  is the tangential force [N];  $C$  is the torque [Nm];  $R_p$  is the pitch diameter [mm];  $n$  is the number of teeth and  $b$  is the face width [mm].

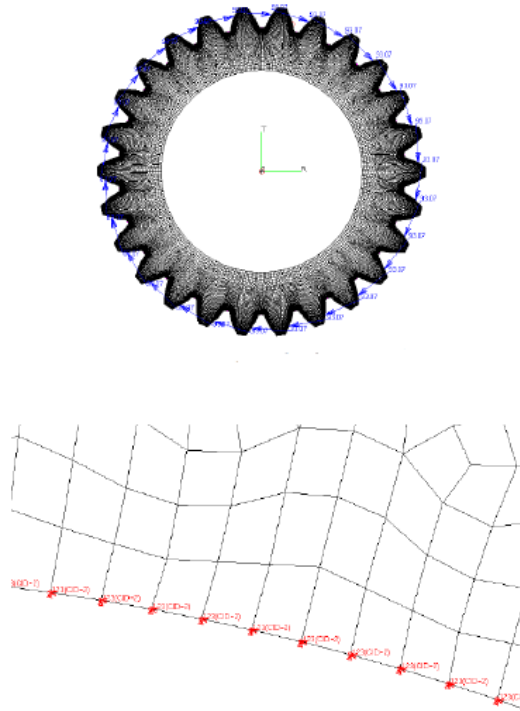


Figure 3.22: Load definition

The last step was to calibrate the model in order to have a uniform distribution of the contact along the profiles of the teeth (Figure 3.23).

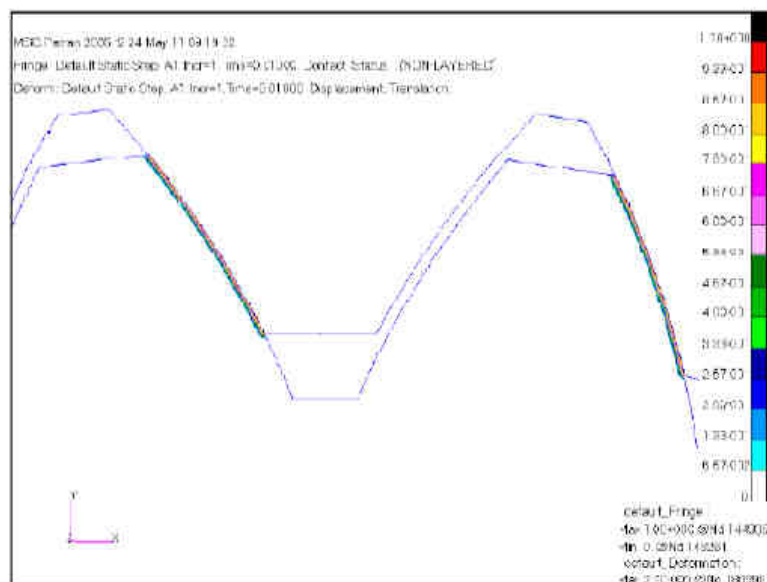


Figure 3.23: Contact distribution

### 3.3.2.8) Fixed joint single tooth model (FEM-0).

This model has a verification purpose; in fact its aim is to demonstrate that the spline coupling tooth can be studied as a beam with fixed joint constraints loaded along the profile to a concentrated force that you decide to position along the pitch diameter (Figure 3.24).

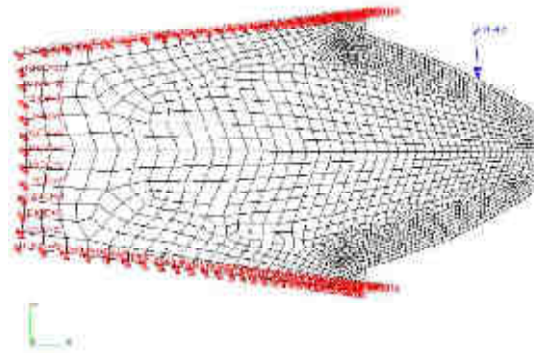


Figure 3.24: Single tooth model

For this model are shown (Figure 3.25-3.27) graphical representations of the distribution of stress and strain.

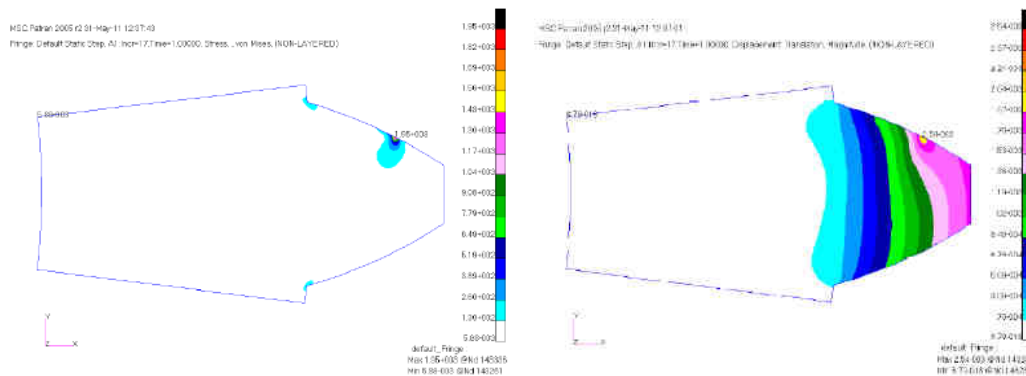


Figure 3.25: Stress (left) and strain (right) distribution for 1000 Nm torque

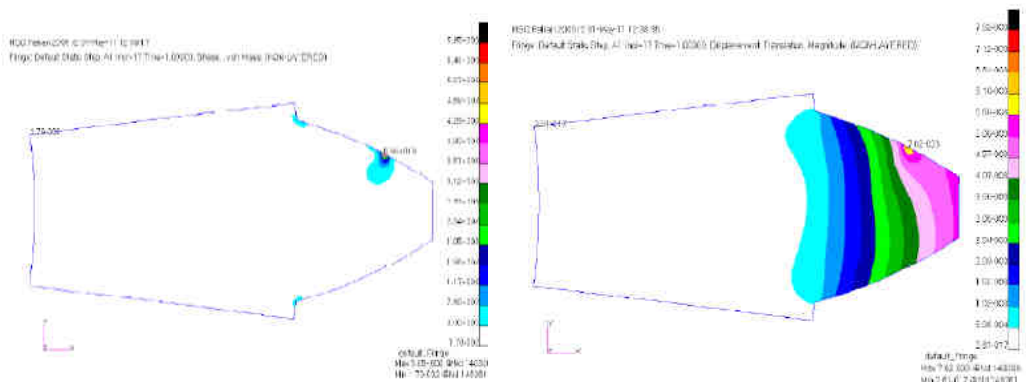


Figure 3.26: Stress (left) and strain (right) distribution for 3000 Nm torque

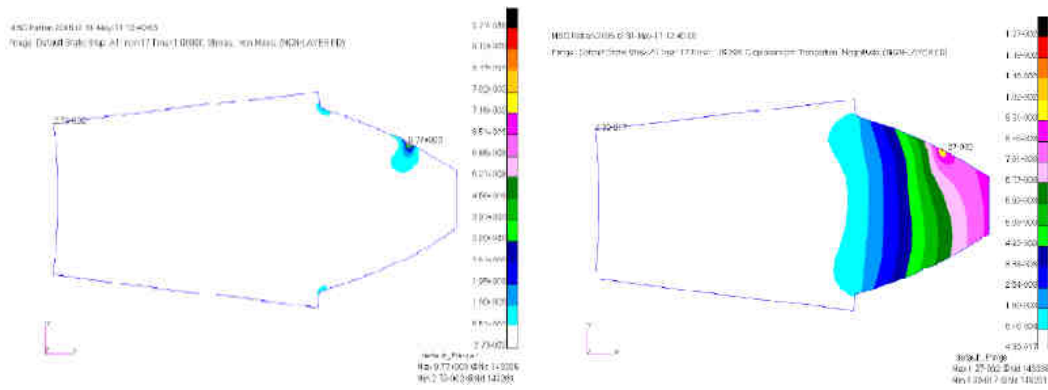


Figure 3.27: Stress (left) and strain (right) distribution for 5000 Nm torque

As can be seen from the previous images, when the tooth is fixed to the other part of the spline coupling, it tends to not deform; this analysis justifies the approximation made in the analytical model in which the contributions of deformation due to the sliding has not be considered.

The following models represent the shaft discretized with symmetrical mesh and loaded by concentrated forces applied to the pitch diameter.

### 3.3.2.9) Splined shaft loaded by concentrated tangential forces (FEM-1)

In Figure 3.28 is shown the model for analyzing the concentrated tangential forces.

In Figure 3.29 is shown, the graphical representation of the strains distribution given by FEM software.

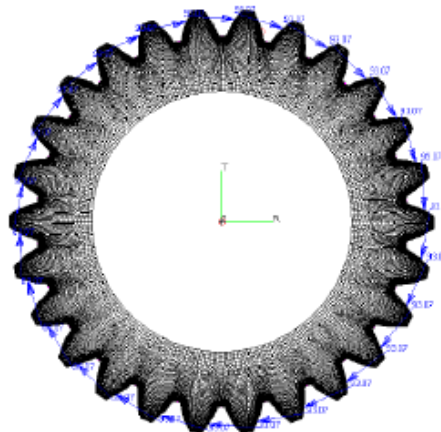


Figure 3.28: Fixed shaft model

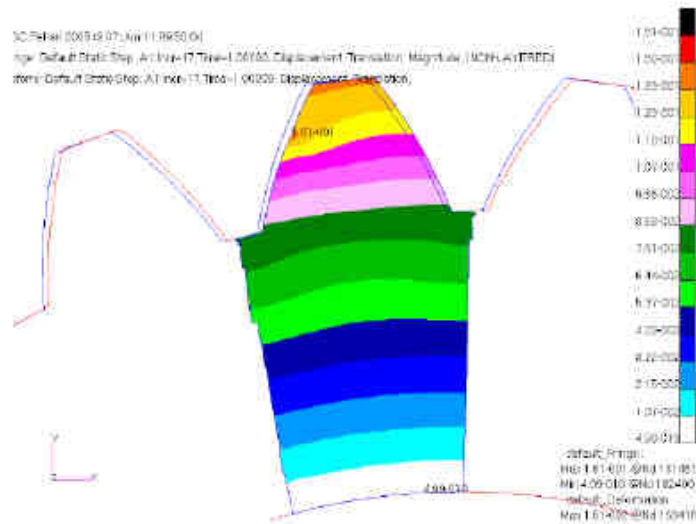


Figure 3.29: Strains distribution of FEM-1

### 3.3.2.10) Splined shaft loaded by concentrated inclined forces (FEM-2)

In this model, unlike the previous one, the concentrated forces applied on the pitch diameter are inclined.

It was decided to use a pressure angle of 30 [°].

The tangential component can easily be calculated as:

$$F_r = F_t \tan(\alpha) \quad (\text{eq. 3.2})$$

The forces are shown in the table 3.5:

C [Nm]	F <sub>t</sub> [N]	F <sub>r</sub> [N]
1000	93.18	53.8
3000	279.55	161.4
5000	465.92	269.00

Table 3.5: Forces of the model

### 3.3.2.11) Splined shaft loaded by concentrated inclined forces and with only tangential constrains (FEM-3)

This further FEM model has been developed to investigate the influence of the sliding on the tangential strains. According to Barrot [4], in fact, the

sliding effect causes a shaft compression that creates orthoradial deformation.

The model has been developed starting from the one described previously and just eliminating the radial constraint. The forces applied, therefore, are the same.

### 3.3.3) Analysis and results comparison

Results obtained in the previous chapter will now be analyzed and compared. Tables will be realized to facilitate the understanding and the percentage differences between the various models will be calculated.

For notation simplicity, the analytical and numerical models will be indicated as:

POLITO that is the analytical model presented previously.

Depending on the contributions considered it will be named as:

- POLITO 1: includes the tangential strains due to bending, shear and rotation of the base.
- POLITO 2: includes the same strains of the model POLITO 1 but considers the concentrated force inclined at 30 °.
- CORNELL: analytical model proposed by Cornell for the gear [67]: it will be compared with the model POLITO and it includes, consequently, the same contributions for the various cases.

Due to the different constraints of each model, they will be compared only with the shear strains ( $\delta_t$ ).

The deformations of the FEM 0 and 1 models are firstly compared with models POLITO 1 and CORNELL 1 to see if the hypothesis introduced in this study is valid and to calculate the percentage of error obtained by using it.

Torque [Nm]	$\delta_t$ FEM 0 [mm]	$\delta_t$ FEM 1 [mm]	Difference [%]
1000	1.02E-03	1.09E-03	6.42
3000	3.89E-03	4.17E-03	6.71
5000	6.49E-03	6.95E-03	6.62

Table 3.6: Comparison between FEM 0 and FEM 1

Torque [Nm]	$\delta_t$ FEM 0 [mm]	$\delta_{TOT}$ POLITO1 [mm]	Difference [%]	CORNELL 1 [mm]	Difference [%]
1000	1.02E-03	1.10E-03	7.27	1.51E-03	32.45
3000	3.89E-03	4.3E-03	9.53	4.46E-03	12.78
5000	6.49E-03	7.2E-03	9.86	7.5E-03	13.46

Table 3.7: Comparison between FEM 0, POLITO 1 and CORNELL models

Torque [Nm]	$\delta_t$ FEM 1 [mm]	$\delta_{TOT}$ POLITO1 [mm]	Difference [%]	CORNELL 1 [mm]	Difference [%]
1000	1.09E-03	1.10E-03	0.9	1.51E-03	27.81
3000	4.17E-03	4.3E-03	3.02	4.46E-03	6.5
5000	6.95E-03	7.2E-03	3.47	7.5E-03	7.33

Table 3.8: Comparison between FEM 1, POLITO1 and CORNELL models

As it can be seen from Table 3.6, models FEM 0 and 1 appear to be tuned; in particular, the percentage difference varies between 6 and 7% depending on the load case.

Comparing both FEM models with analytical models (POLITO 1 and CORNELL 1), good results may be obtained. In fact, the strains calculated by the model POLITO differ by no more than 9% from those obtained with the FEM 0 (Table 3.7) and not more than 3% from those resulting from the model FEM 1 (Table 3.8); the results of model CORNELL 1 are slightly higher.

The next step concerns the comparison of FEM 2, POLITO 2 and CORNELL 2 models.

In all three models the tangential force has been replaced the force inclined, obtained as a combination of a radial and a tangential component.

Being the contribution to the radial force and to the sliding of POLITO and of CORNELL models are similar; the FEM models 2 and 3 will be compared only with the analytical model POLITO.

<b>Torque</b> <b>[Nm]</b>	<b><math>\delta_t</math> FEM 2</b> <b>[mm]</b>	<b><math>\delta_t</math> POLITO 2</b> <b>[mm]</b>	<b>Difference</b> <b>[%]</b>
<b>1000</b>	1.16E-03	1.12E-03	3.57
<b>3000</b>	3.49E-03	3.36E-03	3.86
<b>5000</b>	5.82E-03	5.69E-03	2.28

Table 3.9: Comparison between FEM 2 and POLITO 2 models

The analytical model POLITO gives excellent results even with the addition of the radial component of the applied force, presenting a maximum percentage difference of about 4%.

The next analysis will be carried out by comparing the tangential strains of the FEM 3 and POLITO 3 models.

It is recalled that the FEM 3 model is different from the FEM 2 model for the addition of the radial degree of freedom and, consequently, the POLITO 3 model has in addition sliding compared to the POLITO 2 model.

This contribution was introduced using the notation proposed by Barrot [4].

However, from the analysis of Table 3.10, it is possible to note that FEM 2 and FEM 3 models differ except for the values of radial deformation and not for tangential strains.

Torque [Nm]	$\delta_r$ FEM 2 [mm]	$\delta_t$ FEM 2 [mm]	$\delta_r$ FEM 3 [mm]	$\delta_t$ FEM 3 [mm]
1000	1.33E-06	1.16E-03	1.6E-05	1.16E-03
3000	5.54E-06	3.49E-03	4.64E-05	3.49E-03
5000	1.18E-05	5.82E-03	7.47E-05	5.82E-03

Table 3.10: Comparison of radial strain between FEM 2 and FEM 3 models

On the basis of this analysis it can be established that, in accordance with the classical structural mechanics, the presence or the absence of constraints or loads in purely radial direction influences only on the radial strains.

For this case, values of the difference percentage are substantially higher, as it can be seen from Table 3.11.

Torque [Nm]	$\delta_t$ FEM 3 [mm]	POLITO 3 [mm]	Difference [%]
1000	1.16E-03	1.7E-03	31.76
3000	3.49E-03	5.06E-03	31.03
5000	5.82E-03	8.59E-03	32.25

Table 3.11: Comparison between FEM 3 and POLITO 3 models

Comparing, instead, the FEM 3 model with the analytical model POLITO 2, results obtained are equivalent to those of Table 3.9.

On the basis of the previously compared results (both FEM and analytical), it may be observed that the analytical model is able to describe the behaviour of a spline coupling loaded by a system of concentrated and inclined forces: the related percentage errors are about 3%.

It can be seen that the models for the determination of the tooth deformation has a good correlation compared to the FEM models (Table 3.7, 3.8, 3.9).

So, using the Teeth deflections sub-program (STRASPLINE) with the Geometric sub-program (GEOSPLINE) it is possible to determine the

effective number of teeth in contact when geometric and/or mounting errors are applied to a spline coupling.

Once established the real number of teeth in contact, it is possible to determine the actual contact pressure between the teeth of a splined coupling.

#### 3.4) CONTACT PRESSURE

The effect of the contact pressure on fretting wear life has been debated in the literature. It has generally been observed that there is a decrease in life with increasing contact pressure [68]. These findings are of significant practical importance, indicating that a designer ought to minimize the contact pressure in order to reduce the likelihood of an FW failure. One difficulty with the interpretation of the results of contact pressure studies is that other variables are also varied (notably shearing traction and contact slip). Iyer and Mall [69] studied the interaction for a titanium alloy (Ti-6Al- 4V) for a cylinder-on-flat configuration. They suggested that decreasing FW lives with increasing contact pressure was solely due to the increased contact pressure and increased stress magnitudes associated with higher normal loads and was independent of the other fretting parameters. This is unlikely to be the case given the importance of slip amplitude for fretting [70] and the interaction between all of the parameters.

As previously discussed, the work of Bowden and Tabor [30] offered a key explanation of the behavior of friction. Their work, at first, seemed to be in discrepancy with Amonton's laws, but they showed that with an increase in normal load, a subsequent increase in the 'real' area of contact is obtained.

This leads to the application of the mathematical theory of Hertzian contact that it finds particular confirmation in the case of crowned splined couplings, in fact, because of their particular geometry, the tooth surfaces in contact can be simplified in the case of ellipsoid on plane.

### 3.4.1) Hertzian theory

Classical contact mechanics is most notably associated with Heinrich Hertz [71]. In 1882, Hertz solved the contact problem of two elastic bodies with curved surfaces. This still-relevant classical solution provides a foundation for modern problems in contact mechanics. For example, in mechanical engineering and tribology, Hertzian contact stress is a description of the stress within mating parts. The Hertzian contact stress usually refers to the stress close to the area of contact between two spheres of different radii, but with this theory it is possible to apply to arbitrary-geometry surfaces in contact (nonconforming and continuous).

According to the Hertz theory, when two generic bodies are in contact, and each other are pressed, they create an ellipsoidal contact area and the trend of pressure takes the form shown in Figure 3.30

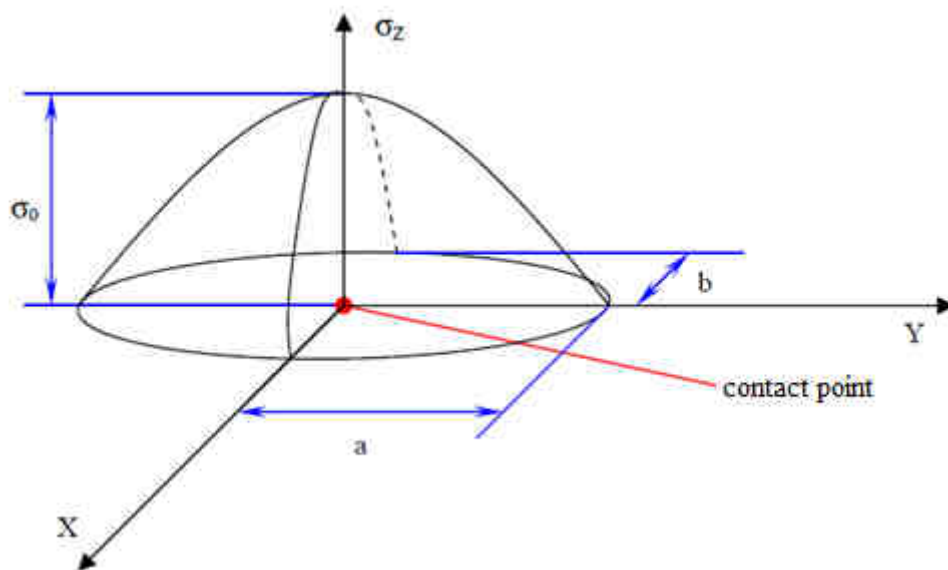


Figure 3.30: pressure trend on contact area [72]

Where X and Y are the principle axes, a and b the semiaxis of the contact area,  $\sigma_0$  the maximum value of pressure contact and  $\sigma_z$  the trend of the pressure along the contact area.

To determine the contact pressure Hertz [71] suggests the following formulation:

$$\sigma_z = \sigma_0 \sqrt{1 - \left(\frac{X}{b}\right)^2 - \left(\frac{Y}{a}\right)^2} \quad (\text{eq. 3.3})$$

where the maximum value of pressure is equal to:

$$\sigma_0 = \frac{3}{2} \frac{F}{\pi ab} \quad (\text{eq. 3.4})$$

It is simple to note that, in order to know the trend of the contact pressure, it is necessary to determine the real contact area.

To do that, Hertz [71] suggests these formulations:

$$a = \mu q \quad (\text{eq. 3.5})$$

$$b = \nu q \quad (\text{eq. 3.6})$$

with:

$$q = \sqrt[3]{\frac{3}{8} \left( \frac{\vartheta_1 + \vartheta_2}{\Sigma \rho} \right) F} \quad (\text{eq. 3.7})$$

$$\vartheta_1 = \frac{1 - \nu_1^2}{E_1} 4 \quad (\text{eq. 3.8})$$

$$\vartheta_2 = \frac{1 - \nu_2^2}{E_2} 4 \quad (\text{eq. 3.9})$$

and for the gears:

$$\Sigma \rho = \left( \frac{1}{R_1} + \frac{1}{R_2} \right) \frac{1}{\sin \alpha} \quad (\text{eq. 3.10})$$

where with  $\nu_i$  and  $E_i$  ( $i=1,2$ ) are respectively indicated the Poisson's ratio and the Elastic modulus for the two bodies in contact;  $R_1$  and  $R_2$  are the diameters of the teeth in contact and  $\alpha$  the pressure angle and  $F$  is the force applied to the bodies.

As a function of the  $\cos \tau$  (eq. 3.11) the value of the two parameters  $\mu$  and  $\nu$  can be determined, using the graph (Figure 3.31) or solving a five equations system (Figure 3.32).

The expression of  $\cos \tau$  is:

$$\cos \tau = \frac{\sqrt{(\rho_1 - \rho'_1)^2 + (\rho_2 - \rho'_2)^2 + 2(\rho_1 - \rho'_1)(\rho_2 - \rho'_2) \cos 2\omega}}{\Sigma \rho} \quad (\text{eq. 3.11})$$

where  $\rho_i$  and  $\rho'_i$  ( $i=1,2$ ) are the principal curvatures and  $\omega$  is the angle between the main tangents of the bodies in contact.

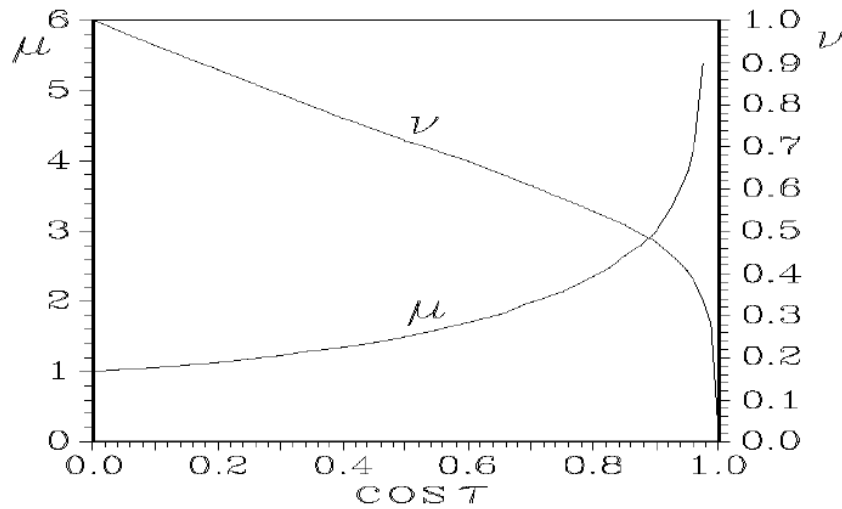


Figure 3.31:  $\mu$  and  $\nu$  trend in function of  $\cos \tau$  [72]

$$\left\{ \begin{array}{l} \frac{\nu}{\mu} = \cos \varepsilon \\ \nu = \sqrt[3]{\frac{2 \cdot E_{(\varepsilon)} \cdot \cos \varepsilon}{\pi}} \\ \cos \tau = 1 - \frac{2}{\operatorname{tg}^2 \varepsilon} \cdot \frac{K_{(\varepsilon)} - E_{(\varepsilon)}}{E_{(\varepsilon)}} \\ K_{(\varepsilon)} = \int_0^{\pi/2} \frac{d\varphi}{\sqrt{1 - \sin^2(\varepsilon) \cdot \sin^2(\varphi)}} \\ E_{(\varepsilon)} = \int_0^{\pi/2} \sqrt{1 - \sin^2(\varepsilon) \cdot \sin^2(\varphi)} \cdot d\varphi \end{array} \right.$$

Figure 3.32: five equations system to determine  $\mu$  and  $\nu$  [72]

In case of crowned splined couplings, the first hypothesis was that the contact is that cylinder-cylinder; by considering the following main

curvatures for the hub :  $\rho_1 = 0$  (along the face width) and  $\rho'_1 = -\frac{1}{R_1}$  (concave curvature,  $R_1$  is the contact radius); for the shaft:  $\rho_2 = \frac{1}{R_c}$  ( $R_c$  is the crowned radius) and  $\rho'_2 = \frac{1}{R_1}$  (convex curvature); when  $\omega=0$  (perfect alignment between hub and shaft teeth);  $\cos \tau$  is:

$$\cos \tau = \frac{\sqrt{(\rho_1 - \rho'_1)^2 + (\rho_2 - \rho'_2)^2 + 2(\rho_1 - \rho'_1)(\rho_2 - \rho'_2) \cos 2\omega}}{\Sigma \rho} = \frac{\sqrt{\left(\frac{1}{R_1}\right)^2 + \left(\frac{1}{R_c} - \frac{1}{R_1}\right)^2 + 2\left(\frac{1}{R_1}\right)\left(\frac{1}{R_c} - \frac{1}{R_1}\right)}}{\frac{1}{R_c} + \frac{1}{R_1} - \frac{1}{R_1}} = 1$$

(eq.3.12)

when  $\cos \tau=0$   $\mu \rightarrow \infty$  and  $v=0$  than  $a \rightarrow \infty$  and  $b=0$  and the contact happens between two cylinders with parallel axes [72].

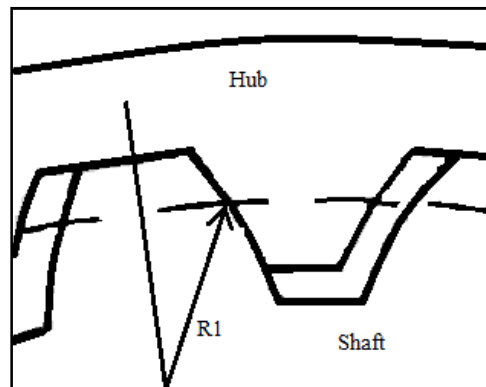


Figure 3.33: contact radius between shaft and hub

By these premises, it would be expected a pressure profile like that shown in Figure 3.34, but this doesn't happen; in fact, as indicated by the experimental tests described in the next paragraph, the real contact area and the trend of the pressure are as shown in Figure 3.35.

This happens because of little machining errors (order of hundredths of a millimeter) make  $\rho_1 \neq 0$ .

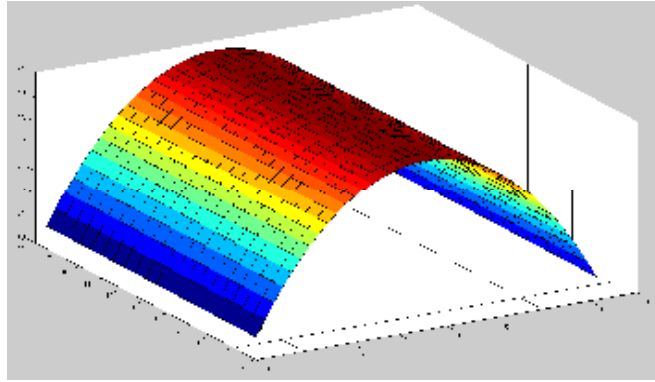


Figure 3.34: hypothesis of pressure trend

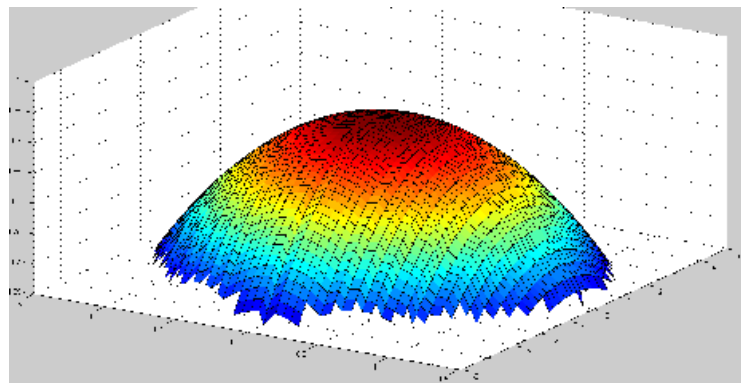


Figure 3.35: real pressure trend

#### 3.4.2) Experimental validation of pressure model

As seen previously, the work of Bowden and Tabor [30] explains how the contact of spline coupling teeth can be analyzed by Hertzian theory; for this way, it has been developed a program that, once set the input parameters (geometries of spline coupling), gives the real contact area and pressure values.

The aim of the tests, conducted in the laboratory, is to validate the program realized during the PhD research activity.

To do that it has been used a test bench (described in detail in the next chapter) able to apply a constant torque and to permit a perfect alignment between hub and shaft axes of a spline coupling.

The pressure in the contact region (ie on the teeth) is very difficult to detect, due to the space between teeth very limited, making impossible to insert any mechanical/electronic device or dedicated sensor.

The only possibility to measure the contact pressure is to use a specific pressure-sensitive film positioned between the contact surfaces.

These films have the property to color themselves proportionally to the applied torque.

#### 3.4.2.1) Test Equipment

To realize the pressure test, a specific specimen has been realized; the difference of a specimen that has been used for the wear test are the whole dept of the teeth.

In fact to have an appropriate area in which to place the film it is chosen to realize a spline coupling with modulus equal to 6 (Figure 3.36 - 3.37).



Figure 3.36 Shaft specimen



Figure 3.37: Hub specimen

Additional equipment results to be a hygrometer (Figure 3.38) that allows measurement of the temperature and the humidity, knowledge of which is essential to acquire the data provided by the films.



Figure 3.38: hygrometer

#### 3.4.2.2) The fuji-film prescale

This kind of sensor is a tool easy to use to detect the magnitude and the distribution of the pressure between two surfaces in contact, and to determinate the real contact area.

The application of the film results to be a simple operation, just cut it of the desired size and apply it between the two surfaces in contact, start the test and remove them once impressed namely once that appear different magenta hues proportional to the load applied between the two surfaces of interest; like show in Figure 3.39.

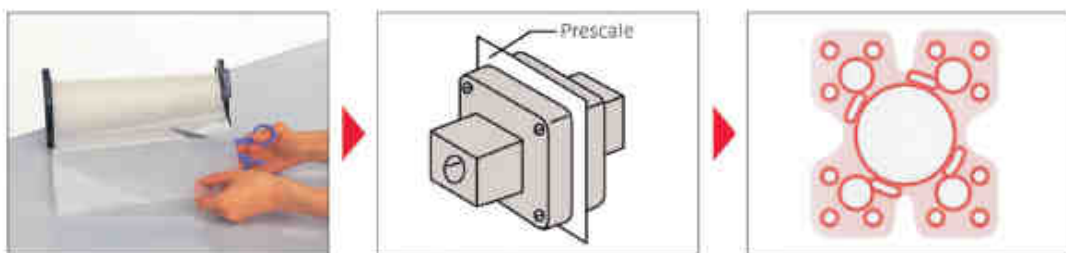


Figure 3.39: Sequence film preparations [73]

It is possible perform two types of pressure measurements with this sensor: momentary or continuous.

In the first case the time to reach the pressure is 5 sec and the time of retention at the pressure is 5 sec.

In the second case the time to reach the pressure is 2 min and the time of retention at the pressure is 2 min.

The films may be of two different types, one consisting of two layers (designated by the producer A + C) and one formed instead by a single layer. In the two-layer (Figure 3.40) are overlapped two different films, the first (named A) is constituted by a polyester base on which are deposited microcapsules of color, the second (named C) also consists of one polyester base coated but with a developing layer. This type is used for the films more sensible, ie those which measure a pressure range less than 10 [Mpa].

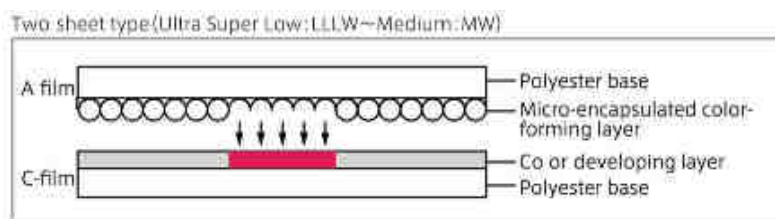


Figure 3.40: Two layers film [73]

The films with a single layer (Figure 3.41) instead are obtained by depositing on a polyester base firstly the layer of development and then covering this with the microcapsules containing the color. This solution is adopted for the films which measure pressures greater than 10 [Mpa].

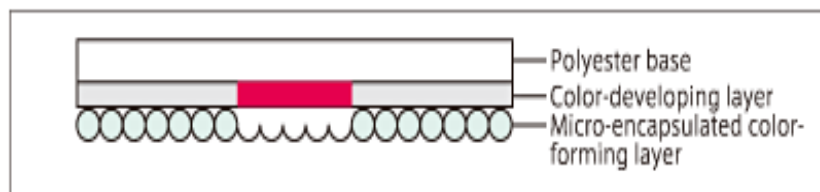


Figure 3.41: One layer film [73]

The prescale films also are available in eight different types according to the range of pressure that are able to detect. Below is a list (Figure 3.42):

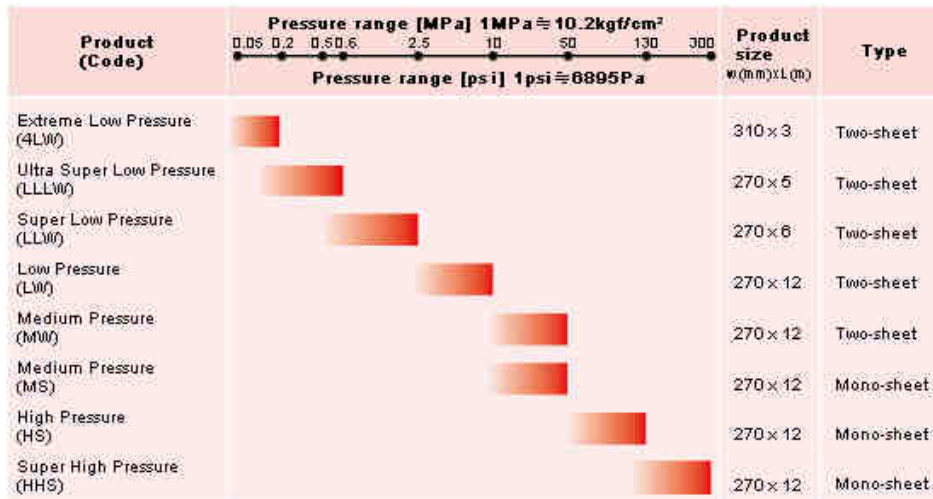


Figure 3.42: Fuji-film prescale types [73]

This type of sensor is sensitive to environment humidity and temperature, in fact, the manufacturer must declare for the Prescale films an accuracy of 10%, calculated at the temperature of 23 ° C and with a relative humidity of 65% . Furthermore, the temperature recommended for the use of these varies from 20 to 35°C and the humidity from 20 to 80%.

For the tests the single sheet MS films with a measuring range from 10 MPa to 50MPa has been chosen to use.

Once finished the test, it must be acquired the data; for do this it is possible to operate in two ways:

1) It is based on the analysis of the film through the use of the human eye, in fact to identify the color intensity imprinted on the film it is used a table (given by the manufacturer), Figure 3.43.

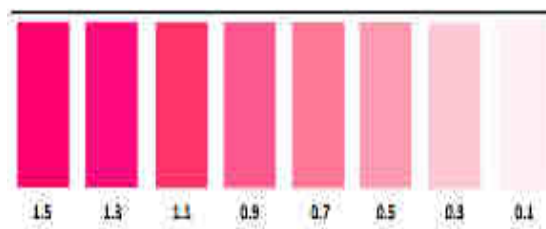


Figure 3.43: Density table of magenta color [73]

Then it must classify the working environment conditions during the experiment ie known temperature and humidity of that and use the

following chart (Figure 3.44) to identify the corresponding workspace (A, B, C, D or E).

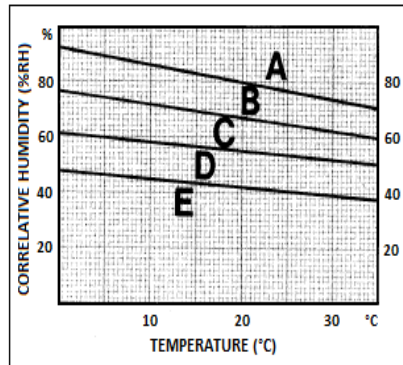


Figure 3.44: Working environment conditions [73]

Finally, depending on the type of test carried out (continuous or momentary) and the film type, it is used an additional chart (Figure 3.45 - Figure 3.46) to define the pressure in a certain film area.

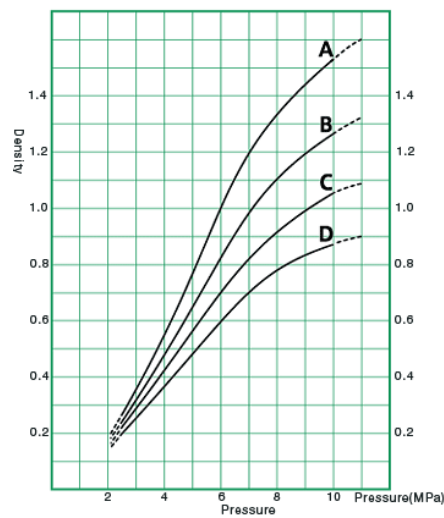


Figure 3.45: Example of continuous pressure chart for LLLW film type [73]

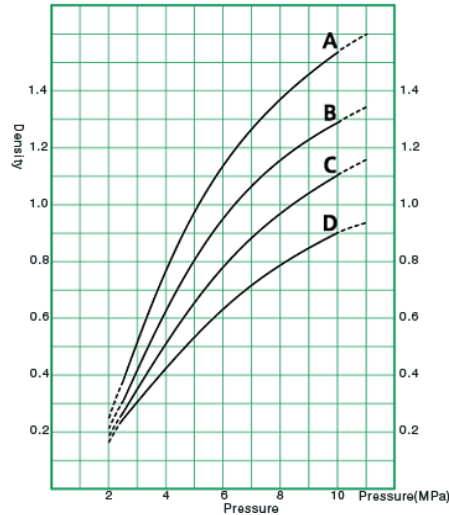


Figure 3.46: Example of momentary pressure chart for LLLW film type [73]

Defect of this method is the greater imprecision of calculation compared to that afforded by the producer, in fact the accuracy becomes of  $\pm 25\%$ .

2) The film is used by a dedicated software called FPD-8010E (developed by the Fujifilm). Thanks to that is possible to analyze the values of the pressure with an accuracy of about 0.125 [mm]

When the film is scanned, the program creates a new file, converting the intensity of the magenta color in pressure values: the results of this conversion can be seen in figure 3.47

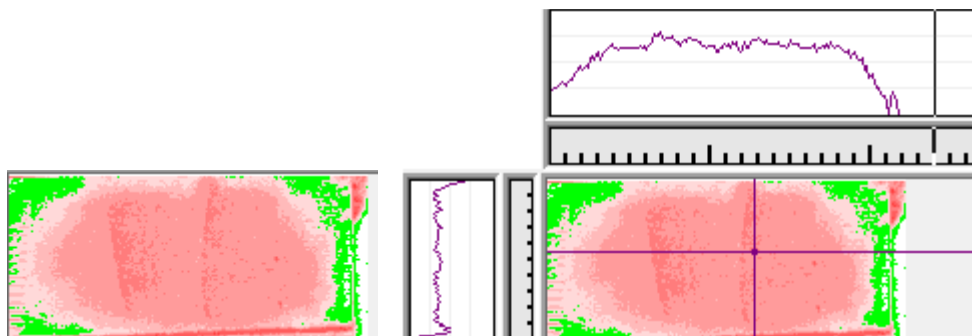


Figure 3.47: film analysis through software FPD-8010E

### 3.4.2.3) Results

Once obtained the digital images of the films, pressure points data have been transferred into a file. TXT, that permit to analyze them with Excel.

With Excel was possible to identify easily the average value that the pressure along the radial direction assumes for each axial coordinate, and with this program it was possible to compare the analytical data of the model with the experimental ones.

To validate the analytic model numerous tests have been carried out, and particularly three different levels of torque (400-700-1000 [Nm]) and thus of force on the teeth of the splined coupling have been analyzed.

In Figure 3.48-3.56 there are the results of the comparison between the analytical model and the experimental tests for some teeth.

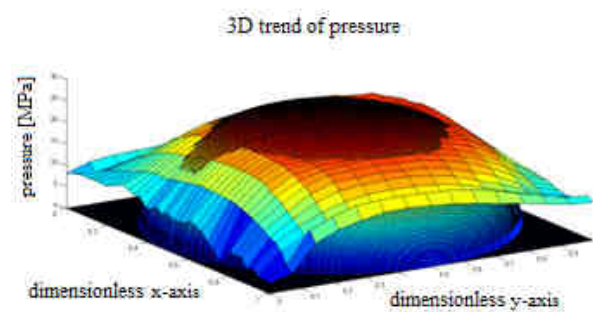


Figure 3.48: 3d trend pressure: experimental data (big mesh) and analytical model (fine mesh) for 400 [Nm] torque

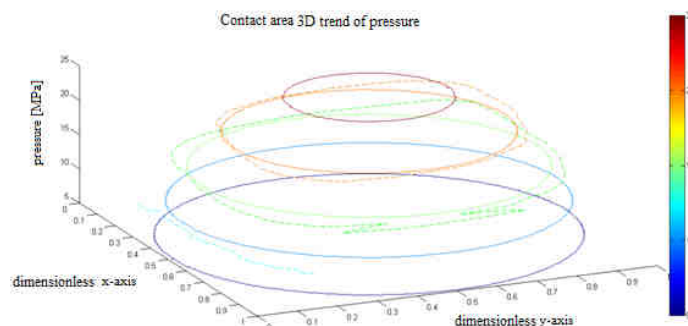


Figure 3.49: contact area: experimental data (dotted line) and analytical model (solid line) for 400 [Nm] torque

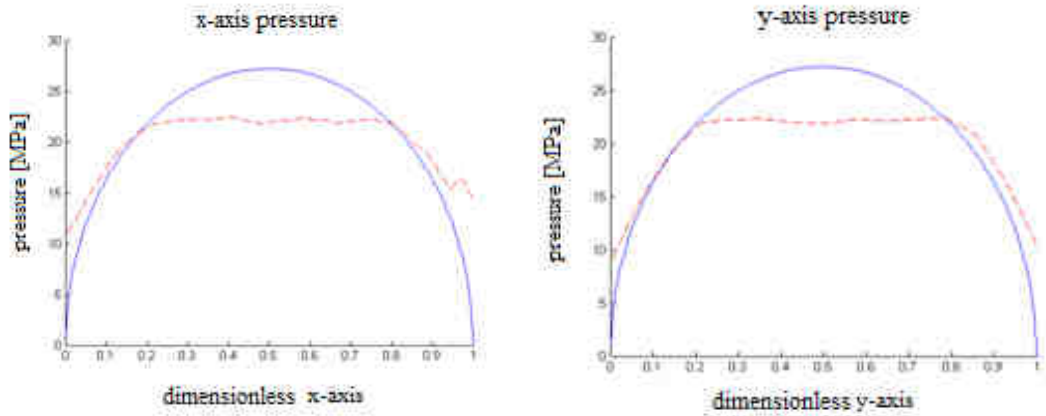


Figure 3.50: pressure comparison, x-axis(left) and y-axis (right); experimental data (red line) and analytical model (blue line) for 400 [Nm] torque

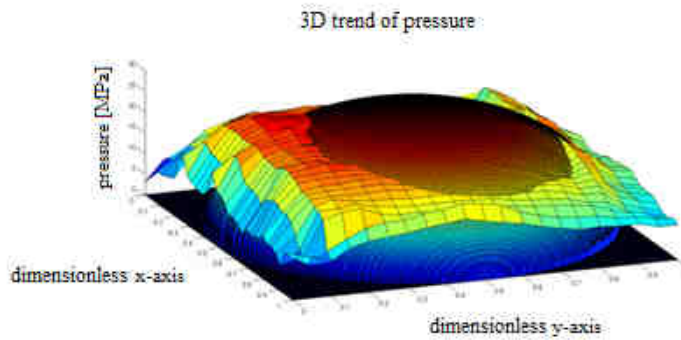


Figure 3.51: 3d trend pressure: experimental data (big mesh) and analytical model (fine mesh) for 700 [Nm] torque

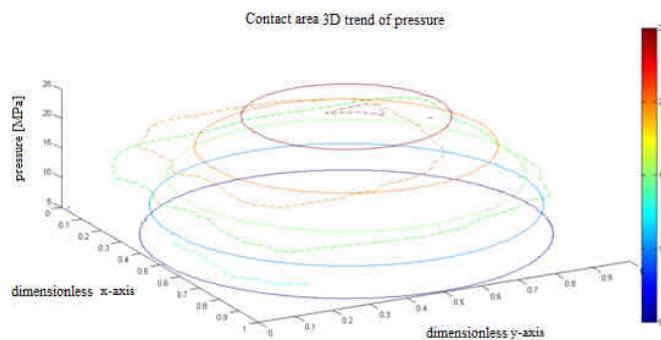


Figure 3.52: contact area: experimental data (dotted line) and analytical model (solid line) for 700 [Nm] torque

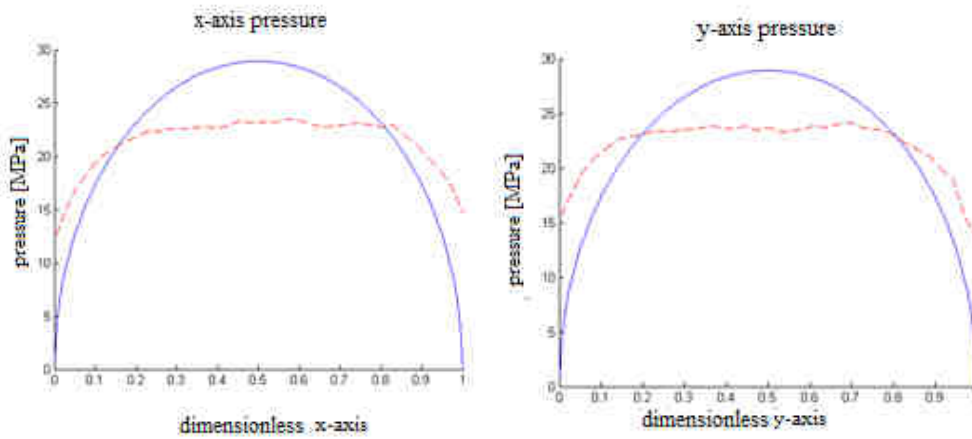


Figure 3.53: pressure comparison, x-axis(left) and y-axis (right); experimental data (red line) and analytical model (blue line) for 700 [Nm] torque

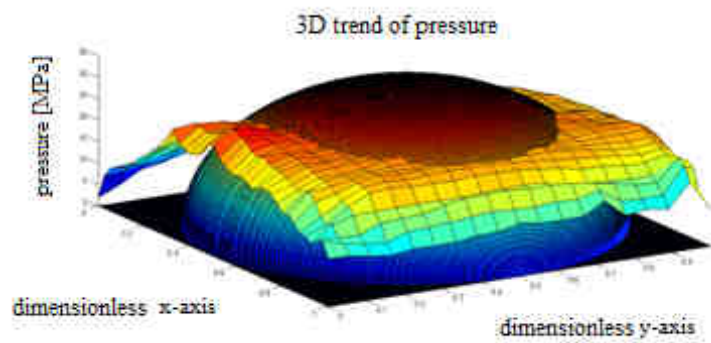


Figure 3.54: 3d trend pressure: experimental data (big mesh) and analytical model (fine mesh) for 1000 [Nm] torque

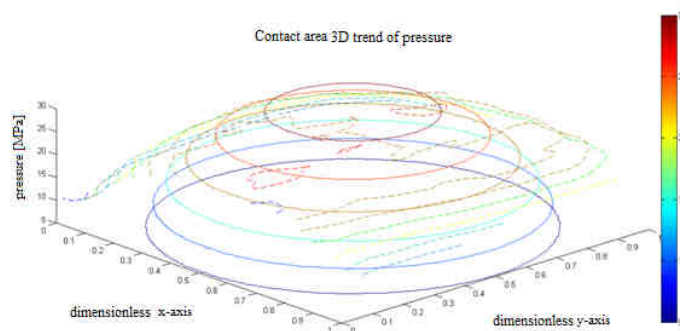


Figure 3.55: contact area: experimental data (dotted line) and analytical model (solid line) for 1000 [Nm] torque

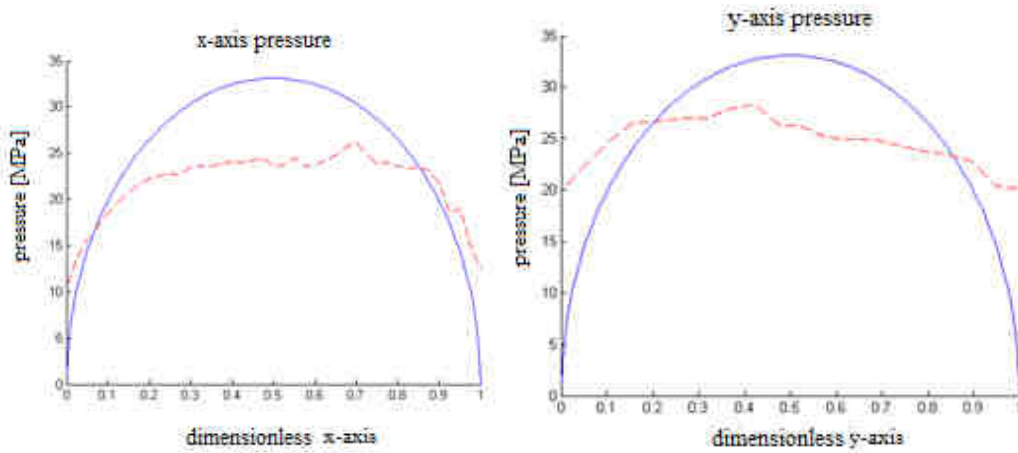


Figure 3.56: pressure comparison, x-axis(left) and y-axis (right); experimental data (red line) and analytical model (blue line) for 1000 [Nm] torque

Tables 3.12-3.20 show the comparison results between the analytical model and the experimental results for the values of the elliptic contact area principal axes, the percentage average difference between the axes and between the pressure and the values of the maximum pressure ( $\sigma_0$ ).

These comparison is done for three levels of torque.

1) Test result when it is applied 400 [Nm] torque in the test bench

Analytical principal axes values of the contact area [mm]	
2a	2b
7.73	15.42
Experimental principal axes of the contact area (average values) [mm]	
2a	2b
7.4	14.15

Table 3.12: contact area principal axes comparison for 400 [Nm] torque

Percentage difference %			
Tooth	2a (average)	2b (average)	Pressure
1	4.2	8.22	8.86
2	4.2	8.22	15.58
3	4.2	8.22	15.13
4	4.2	8.22	15.48
5	4.2	8.22	12.77
6	4.2	8.22	9.21
7	4.2	8.22	9.86

Table 3.13: percentage difference of the average values of the contact area principal axes and of the maximum value of contact pressure for 400 [Nm] torque

Maximum pressure value [Mpa]	
Experimental	Analytical
25.2	27.19

Table 3.14: comparison between the maximum values of the contact pressure for 400 [Nm] torque

2) Test result when it is applied 700 [Nm] torque in the test bench

Analytical principal axes values of the contact area [mm]	
2a	2b
9.74	19.45
Experimental principal axes of the contact area (average values ) [mm]	
2a	2b
9.37	17.77

Table 3.15: contact area principal axes comparison for 700 [Nm] torque

Percentage difference %			
Tooth	2b	2a	Pressure
1	3.78	8.63	2.8
2	3.78	8.63	10.48
3	3.78	8.63	8.2
4	3.78	8.63	15.2
5	3.78	8.63	6.35
6	3.78	8.63	13.5
7	3.78	8.63	14.42

Table 3.16: percentage difference of the average values of the contact area principal axes and of the maximum value of contact pressure for 700 [Nm] torque

Maximum pressure value [Mpa]	
Experimental	Analytical
28.51	29.26

Table 3.17: comparison between the maximum values of the contact pressure for 700 [Nm] torque

3) Test result when it is applied 1000 [Nm] torque in the test bench

Analytical principal axes values of the contact area [mm]	
2a	2b
10.9	20.76
Experimental principal axes of the contact area (average values) [mm]	
2a	2b
10	18.4

Table 3.18: contact area principal axes comparison for 1000 [Nm] torque

Percentage difference %			
Tooth	2a	2b	Pressure
1	8.20	11.33	14.24
2	8.20	11.33	15.3
3	8.20	11.33	4.08
4	8.20	11.33	9.38
5	8.20	11.33	13.1
6	8.20	11.33	19
7	8.20	11.33	4.46

Table 3.19: percentage difference of the average values of the contact area principal axes and of the maximum value of contact pressure for 1000 [Nm] torque

Maximum pressure value [Mpa]	
Experimental	Analytical
29.9	34.8

Table 3.20: comparison between the maximum values of the contact pressure for 1000 [Nm] torque

As it can be seen from what previously written the pressure code has been validated by comparisons with the experimental tests.

Particularly, it was observed that the analytical model is able to describe what happens in loaded teeth of a spline coupling, presenting the percentage minimum error of about 2.8% when it is applied 700 [Nm] torque and a maximum error vales of 15.58 when it is applied 400 [Nm] torque. These percentage errors are very good; in fact also the manufacturer provides a measurement error of the films that is about 10%.

Another important experimental result is shown in Table 3.21.

	Experimental axes [mm]		Analytical axes [mm]			
Torque [Nm]	2a	2b	2a	2b	$\sqrt[3]{F}$	Root ratio
400	7.4	14.15	7.73	15.42	7.36	
700	9.37	17.77	9.74	19.45	8.87	
1000	10	18.4	10.9	20.76	10	
	Experimental axes ratio		Analytical axes ratio			
700/400	1.26	1.25	1.26	1.26		1.2
1000/700	1.06	1.03	1.119	1.12		1.11

Table 3.21: cube root ratio between experimental and analytical values of the contact area principal axes

The Hertzian theory [71] shows how the principal axes of the contact area must change with the value  $\sqrt[3]{F}$  (eq. 3.5 - 3.7), where F is the force applied to the two bodies in contact.

To validate the values of the contact area provided by the analytical program, it is chosen to compare the cube root ratio.

As it can be seen in Table 3.21, the ratios of the experimental tests and the analytical model are very similar.

Once established both real contact area and pressure trend, it is possible to analyze another important factor responsible of the presence of the fretting wear.

### 3.5) CONTACT SLIP AMPLITUDE

The magnitude of contact slip has been shown to be a key parameter with respect to fretting wear, although it has persistently been challenging to experimentally determine. It is typically small and therefore prone to experimental error. Researchers have used linear-variable differential transformers (LVDTs) [44], and extensometers [74, 75] near the contact surfaces in an attempt to quantify its magnitude.

It is almost universally found that the measurements are significantly greater than the analytically or numerically-predicted values (e.g. by finite element analysis such as in Ref. [76]).

Nevertheless, Nishida et al. [77] obtained a good correlation with FE predicted values by utilizing a novel experimental approach. They used a test setup *in-situ* with scanning electron microscopy (SEM) to measure the displacement of a point on the fretting pads in relation to the fretting specimen. They found that their SEM measured displacements were significantly less than those measured using an extensometer.

It is generally accepted that a significant proportion of the discrepancy between measured and predicted displacements is due to the compliance of the testing fixture. Attempts have been made to include the compliance in the models, although the actual contributions from the individual test parts have not to date been fully modeled. Including more of the test fixtures in models will typically help to better quantify the compliance effects.

The three regimes that are used to describe the contact slip state are: complete stick, partial slip and full (gross) sliding. These are often plotted on a fretting map (FM) as shown, for example, in Figure 2.8.

The contact slip regime can be inferred from analysis of the dynamic experimental force-displacement loops. Figure 3.57 shows the characteristic shapes of the loops for each of the fretting regimes [38].

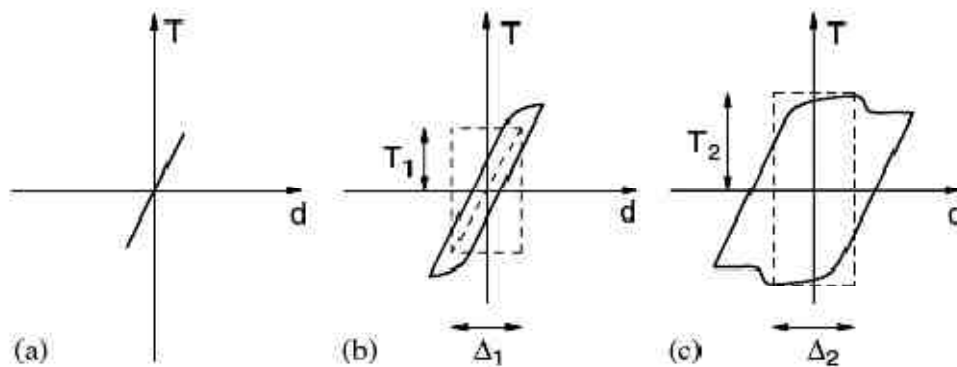


Figure 3.57: The characteristic shape of the fretting F- $\delta$  loops for a) stick b) partial slip c) gross sliding [38]

For complete stick, the relationship is linear. Under partial slip, a hysteresis loop is observed due to energy dissipation. For full sliding conditions, the hysteresis loop is opened up and portions of the curve are parallel to the displacement axis. A drawback of inferring the slip regime from bulk measurements is that the technique is unable to discern the variation of contact slip across the surface.

To overcome this, Jin and Mall used the FE method to discern the variation of the slip across the surface [78], calibrating it against the measured global relative displacements. An alternative method of determining the slip regime was offered by Varenberg [79], introducing a non-dimensional 'slip index'. It was argued that this provides a more accurate description of the fretting condition. However the approach has not, to date, received widespread use in the field.

Vingsbo and Soderberg [37] examined various experimental data from the literature for the cylinder-on-flat geometry. They usefully represented the effect of slip amplitude on FF life as in Figure 3.58.

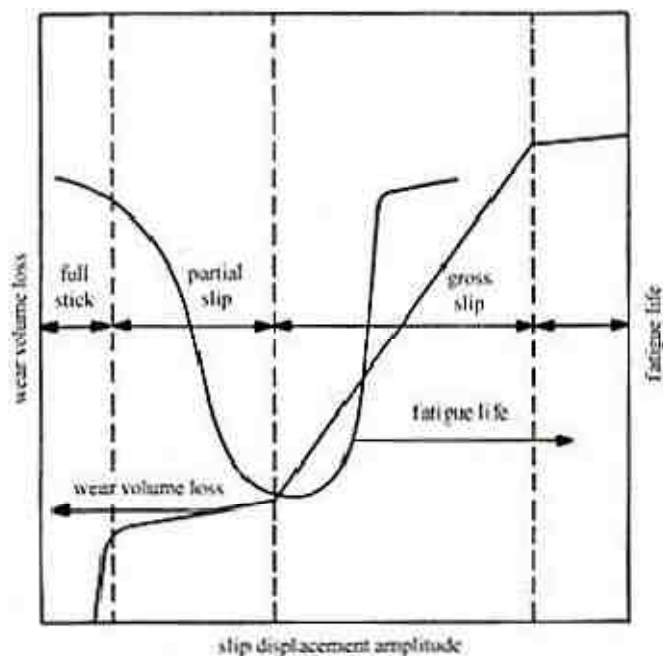


Figure 3.58: The effect of slip amplitude on fretting fatigue life and wear rate [37]

For complete stick behaviour, or low amplitude slip, component life may be interpreted as the plain fatigue life in the presence of a stress concentration and associated gradient. They crucially showed that there exists a critical slip amplitude which yields the minimum FW life. This is often in the partial slip regime. For larger slip amplitudes (gross sliding regime) the life is seen to recover, possibly due to wear mechanisms becoming more dominant.

An additional explanation was offered following a numerical wear simulation methodology [16, 80]. It was shown that the stress field is amplified during partial slip and attenuated during gross sliding conditions. The quantitative determination of the competition between fatigue cracking and wear mechanisms offers promise in the understanding of FW.

In this thesis a program has been realized to analyze the movement that the contact area of the spline coupling does during a complete rotation.

In fact to understand the fretting wear phenomenon on the splined coupling a test bench was created; this test bench, that will be explained in detail in the next chapter, has the peculiarity to maintain constant the misalignment between the hub and the shaft of the specimen (the spline coupling).

Starting from this assumption, a cinematic model is realized; analyzing the scheme in Figure 3.59, it is possible to observe how the contact area, when the spline coupling is perfectly aligned (red ellipse), changes its position (blue ellipse) when a misalignment of  $\beta$  angle is imposed.

This contact area translation happens in a half rotation; to analyze a complete rotation of the specimen, the same operation must be repeated in the opposite direction.

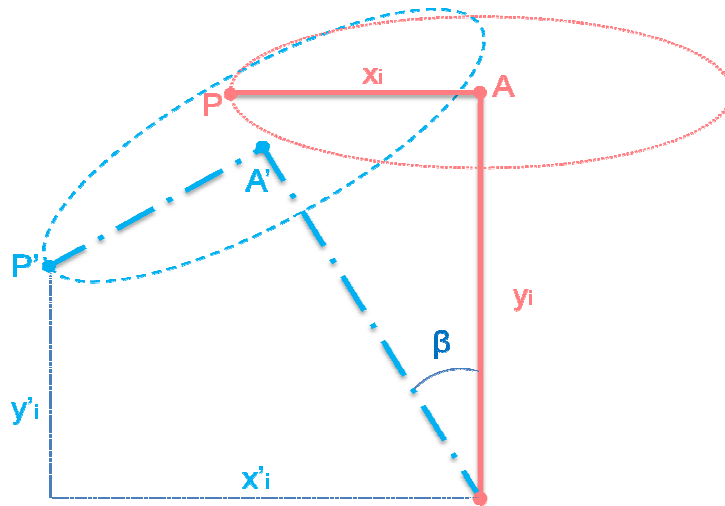


Figure 3.59: cinematic scheme of the contact area translation in a half rotation

Observing the scheme in Figure 3.59 is simple to obtain the displacement equations of the contact area points:

$$x'_i = y_i \cdot \sin \beta + x_i \cdot \cos \beta \quad (\text{eq.3.13})$$

$$y'_i = y_i \cdot \cos \beta - x_i \cdot \sin \beta \quad (\text{eq.3.14})$$

By combining the equation of the abscissa and of the ordinate coordinates, it is obtained the displacement matrix:

$$\begin{bmatrix} x'_i \\ y'_i \end{bmatrix} = \begin{bmatrix} x_i \\ y_i \end{bmatrix} \cdot \begin{bmatrix} \cos \beta & \sin \beta \\ -\sin \beta & \cos \beta \end{bmatrix}$$

Once that all the coordinates of the new contact area points are obtained (blue ellipse), it is simple to obtain the sliding points value:

$$\delta = \sqrt{(x'_i - x_i)^2 + (y'_i - y_i)^2} \quad (\text{eq. 3.15})$$

In Figure 3.60 it is shown the outputs of the sliding program considering 10 [°] of misalignment (in the left) and 15 [°] in the right; the maximum misalignment value that the test bench can provide is 10 [°]; the right part of the Figure 3.60 is represented to well understand the effective movement of the contact area.

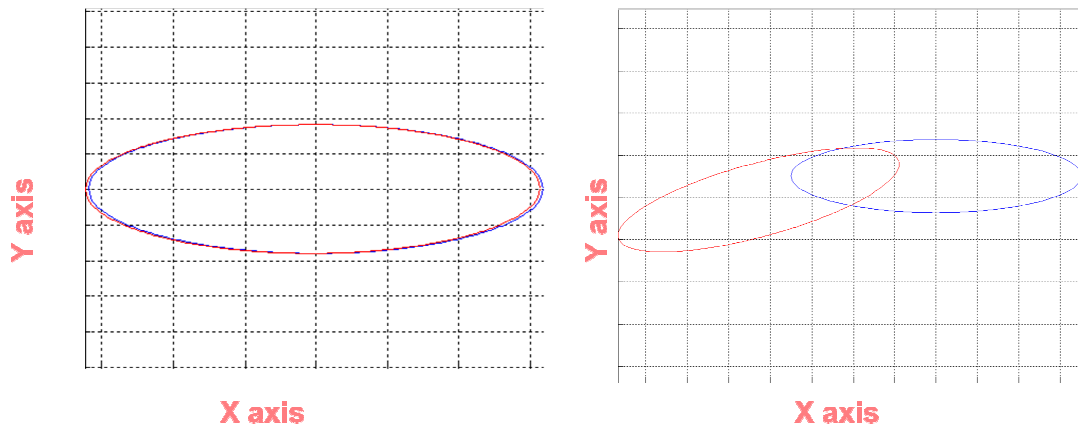


Figure 3.60: Representation of the contact area movements during a half rotation of the crowned spline coupling (specimen)

### 3.6) FRETTING MODELS

#### 3.6.1) Introduction

A methodology that is able to predict cracking location, the number of cycles to failure of fretted components or the wear damage after a certain number of cycles would allow the optimization of designs for components in contact. Fretting is influenced by the complex interaction of varying mechanisms that must be accounted for and the unification of these is critical.

It is clear that contact slip also induces surface damage [52]. One key barrier to be overcome in the solution of the fretting problem is the determination of the relative significances of stress gradient effects and surface damage effects. While there are a lot of model that predict the fretting fatigue, like the Smith-Watson-Topper (SWT) parameter [81, 82], the method proposed by Madge JJ. et al. [83], and the second Ruiz parameter [84] for predicting the presence of fretting wear the most important parameter is the first Ruiz one [84].

#### 3.6.2) Ruiz fretting fatigue parameters

The Ruiz parameters [84], initially formulated for fretting fatigue in dovetail applications, are considered here particularly for their emphasis on the slip amplitude as a key variable on fretting wear. There are two types of Ruiz parameters: one is  $R_1 = \tau \cdot \delta$  and  $R_2 = \sigma \cdot \tau \cdot \delta$ , where  $\tau = \mu \cdot P$  is the surface

shear traction (that is the multiplication between the COF and the pressure of the contact points),  $\delta$  is the relative slip amplitude between the two surfaces and  $\sigma$  is the subsurface tangential stress parallel to the surface.

In fact,  $R_1$  corresponds to the frictional work expended during a fretting cycle, whilst  $R_2$  corresponds to the combined effect of stress and frictional work.

The Ruiz parameters are calculated here along the spline axial direction (z-axis) and along the transverse tooth involute (x-axis).

The Ruiz parameter to determine fretting wear ( $R_1$ ) is a good parameter for determining the wear phenomenon although the physical interpretation of this is unclear; it is also a hybrid approach that measures two processes arbitrarily multiplying with the same weight.

The fact that  $R_1$  depends strongly on the stresses gives a consequent dependence on other parameters that make the results difficult to understand.

Thus, the results provided require a separate study that will not necessarily provide definitive answers; but, since the purpose of this thesis is the qualitative and not the quantitative wear determination, this model is highly appropriate and, as we shall see in the chapter of experimental results, it provides excellent results.

## CHAPTER 4: TEST BENCH DESIGN

### 4.1) INTRODUCTION

The splined couplings are used to connect two rotating parts; in the industrial sector, these components found several applications, particularly in the aerospace field.

One of the main causes of damage is the rubbing wear caused by the relative movement between the teeth in contact; this wear phenomenon is due by misalignment generated during working; this factor is critical in the design phase because of high loads on the teeth and moments of reaction.

The wear is very difficult to calculate in the design phase and often FEM programs are used: for this reason experimental tests are needed to understand and to evaluate how the misalignment can affect the presence of signs of wear.

In literature regarding this subject there isn't a sufficient discussion; for this reason a new test bench for splined couplings has been designed and realized.

The main feature of the test bench is to be able to apply and to monitor a specific angular misalignment between spline coupling and it is able to reproduce the real operating conditions.

Thanks to this new test bench it is possible to monitor a lot of experimental data (debris present in the oil, temperature and strain of the specimen, speed rotation, torque, etc..) and in particular the Ruiz parameter for fretting wear can be compared and calibrated.

### 4.2) TEST BENCH DESCRIPTION

The test bench type presented in this work is called: mechanical power recirculation; since the external power to be applied offsets only the power dissipated in friction.

The main advantage of this architecture is the use of reduced power motors which involve lower costs of production and low energy consumption.

The preliminary technical data of the test bench under review are shown in Table 4.1:

<b>Engine power</b>	6.3 [kW]
<b>Length</b>	2.5 [m]
<b>Depth</b>	1.5 [m]
<b>Weigh</b>	3.5 [t]
<b>Max torque</b>	5000 [Nm]
<b>Max rotating speed</b>	2000 [rpm]
<b>Max Lubrication temperature</b>	60 [°C]
<b>Max misalignment</b>	13 [°]
<b>Misalignment increments</b>	0.5 [°]

Table 4.1: technical data of the test bench

The working scheme is the following (Figure 4.1-4.2): there are two coaxial shafts, one inside (the yellow in Figure 4.2) and the other external (the blue in Figure 4.2), both are connected to a torque applicator T (the purple in Figure 4.2).

The inner shaft is made up of two parts connected through the splines (specimen) to be tested.

When torque is applied to the inner shaft, this through the spline passes to the outer shaft and returns to the generator T; that causes a torque loop that keeps the specimen under load.

The two shafts, as well as spline coupling, can rotate by mean of an electric motor M connected to the external shaft by a belt.

A lever device allows to create a misalignment between the hub and the shaft of spline coupling; this is made possible by using a laminated flexible joint (the black in Figure 4.2) between the outer shaft parts.

A homokinetic joint (the azure in Figure 4.2) decouples the hub (left part of specimen) so as to find a position of equilibrium during the course of the test.

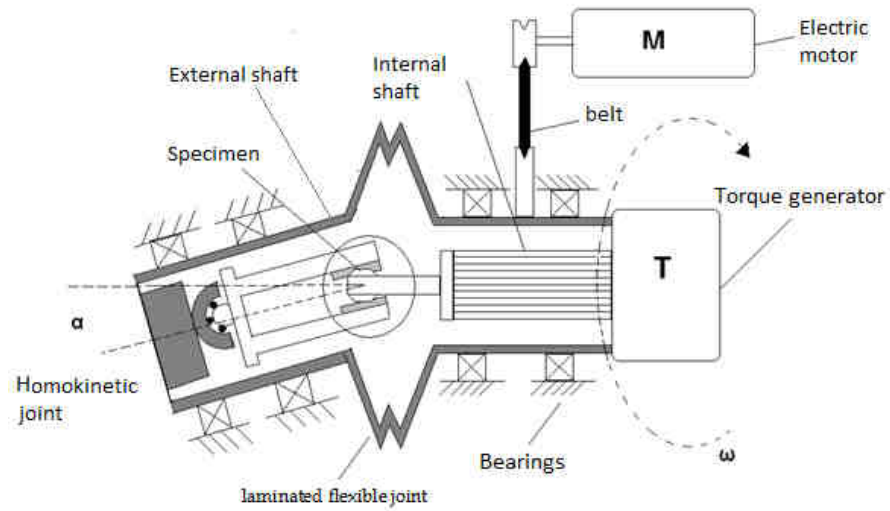


Figure 4.1: test bench scheme

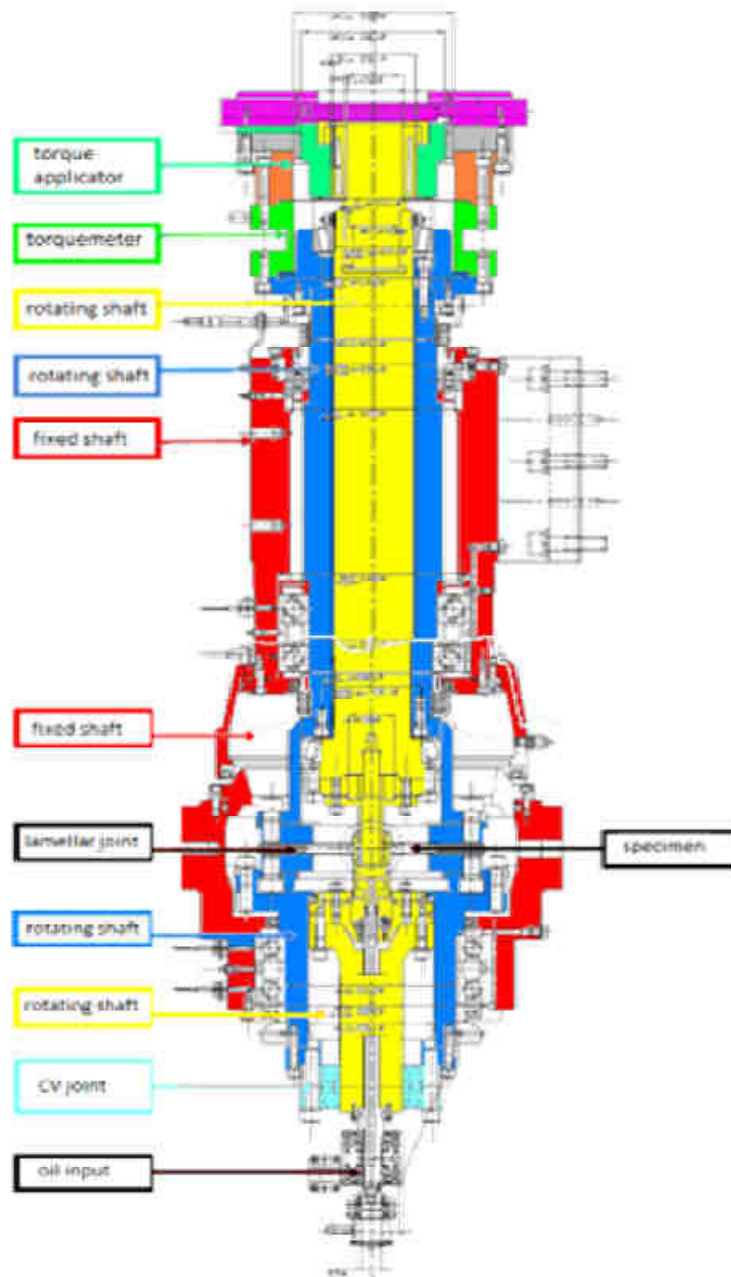


Figure 4.2: technical scheme of test bench

In Figure 4.3 and 4.4 are shown the test bench installed in the Laboratory of the Mechanical and Aeronautical department in the Politecnico di Torino.



Figure 4.3: front view of the test bench



Figure 4.4: lateral view of the test bench

#### 4.3) TEST BENCH CHARACTERISTICS

The test bench has been designed to replicate, as realistic as possible, the real operating conditions (in aerospace applications) under which a splined coupling is subjected.

The torque application system is mechanical, as shown in Figure 4.5.



Figure 4.5: mechanical torque applicator

The torque range is from 0 to 5000 Nm; it is constant during every test and at beginning is without transient. The accuracy about torque applied is of + / - 1%.

The number of cycles required for each test is 10M cycles, to be performed at the most in 5 days (24/24h) and including equipping times.

For this reason the minimum operating speed is 1500 rpm.

The speed rotation is produced by an electrical motor; the engine is vectorial with nominal power of 6.3 [kW]. The maximum speed that is able to manage is 2000 rpm. It is shown in Figure 4.6.



Figure 4.6: electrical motor

A forced lubrication system is present, it reproduces the operating lubrication conditions of splined couplings. It is provided a heating system for the oil so that it can lead to a maximum temperature of 60 ° C. The oil system and the admission of its is presented in Figure 4.7.



Figure 4.7: admission oil system (left) and system oil (right)

As explained above, it is possible to simulate the misalignment that may occur in the real case, the test bench allows a maximum inclination of 13' obtained by progressive increments of 0.5'.

#### 4.4) MEASURING INSTRUMENTS

During the working phases of the test bench are detected the levels of force, of torques circulating, of temperature, of speed and of inclination. For this reason, there are the following measuring instruments:

- a torque transducer (specially designed) with full scale of 5 [kNm] and a 1% error;
- a load cell type HBM with a full scale of 20 [kN] for the detection of loads due to misalignment;
- a load cell of the type HBM with full scale of 10 [kN] for the detection of calibration loads;
- some strain gauge mounted on the specimen;
- a thermocouple mounted on the specimen;
- temperature sensors mounted on the main bearings;
- two digital flow meters with adjustable threshold;

- an Oil Debris system that finds and analyzes the metal particles in the lubricant to monitor the wear phenomenon
- the conditioning modules for all sensors.

#### 4.5) CONTROL SYSTEM

The test bench is designed to perform the tests reported on Table 4.2:

Parameters to be checked:
Wear without misalignment
Wear with misalignment and with constant angle
Wear with variable misalignment
Reaction moment due to inclination
Stiffness of the spline coupling teeth
Max Lubrication temperature
Max misalignment
Misalignment increments

Table 4.2: parameters that the test bench is able to be checked

The signals acquired during the course of a test are:

- shaft speed (phonic wheel);
- electric motor rotation speed (encoder)
- torque (torque transducer);
- tilting support and misalignment between shaft and hub (LVDT);
- reaction force due to misalignment (load cell) ;
- flow rate oil to the sample and flow rate to the oil debris system (digital flow meters) ;
- bearing temperature (thermocouple);
- specimen temperature (thermocouple);
- specimen strain (strain gauge);
- metal particles in the oil (Oil Debris system);

#### 4.6) WEAR TEST

Each test consists of a sequence of cycles, to realize a wear test the duration of every test is of 10 M of cycles, that with a speed of 1500 rpm has a time period of about 5 days.

Every cycle is defined by the following parameters:

- misalignment set-point;
- speed set-point;
- system control during the cycle: torque, test article temperature and reaction force threshold ;
- test period (in cycles or in minutes);
- data acquisition frequency;
- pause at the end of one cycle;

The test bench must perform the following actions during the execution of the test:

1. set the inclination request
2. lead up the test article at required speed
3. continue the test for the set duration
4. acquire and save the output signals from the test bench
5. when a threshold is exceeded interrupt the test

Firstly to make a correct wear test on the bench, it is necessary to set a file allowing to insert all the operating parameters of the bench; this file (which will be considered as input in management and monitoring software of the bench) is used to simulate as close as possible the real operating conditions of the spline coupling.

This file is set using a graphical interface (see Figure 4.8); in particular it is possible to manage:

- rotating speed
- number of cycles
- test time





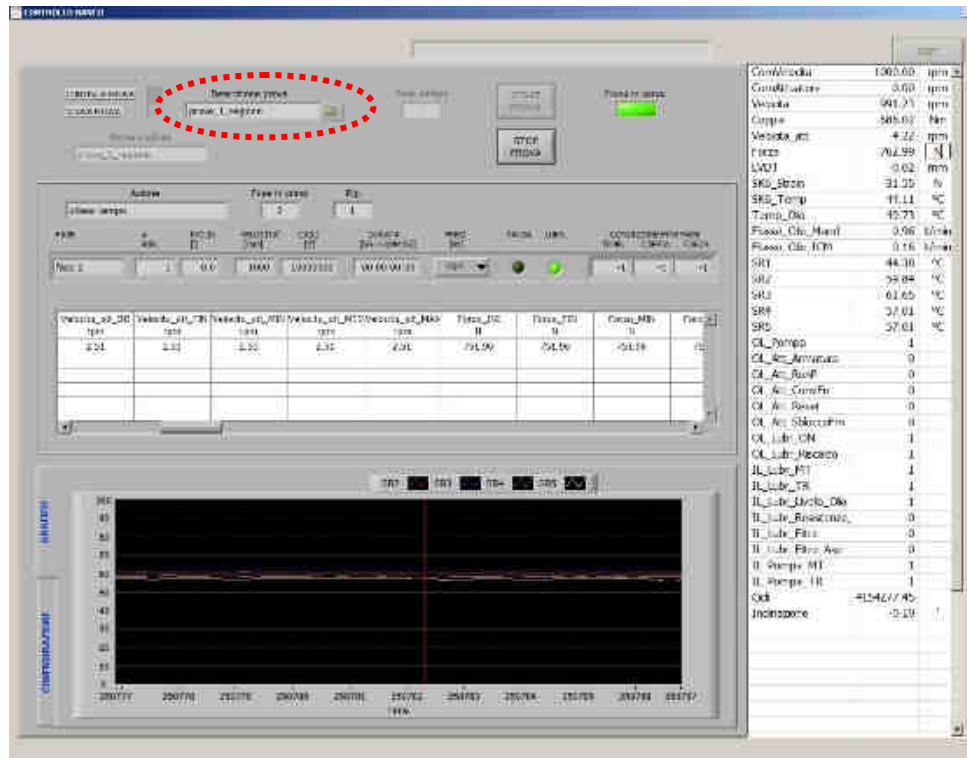


Figure 4.10: screen of the test management.

After importing the file description of the test and started the test itself, the software test bench is able to manage and to display in real-time a series of information listed below:

- speed input system (the speed to be reached during a single phase of the test);
- input speed of the actuator (it is used to create the misalignment between shaft and hub);
- actual speed of the system;
- torque;
- real speed of the actuator;
- force generated by misalignment;
- moving the lever arm that is created between the tilting system of the Test Article and the centerline of the face width of the shaft and the hub (LVDT);
- strain and temperature of the Test Article;
- lubricant temperature;

- oil supply flow;
- oil flow analyzed by the system Oil Debris;
- bearings temperature;
- number of cycles realized every test phase;
- real misalignment between shaft and hub.

In addition to these data, in the window (Figure 4.11) are represented a series of outputs which allow to identify whether a particular component of the test bench is actually working (represented by the number '1' in the value box) or not (represented by the number '0' in the value box)

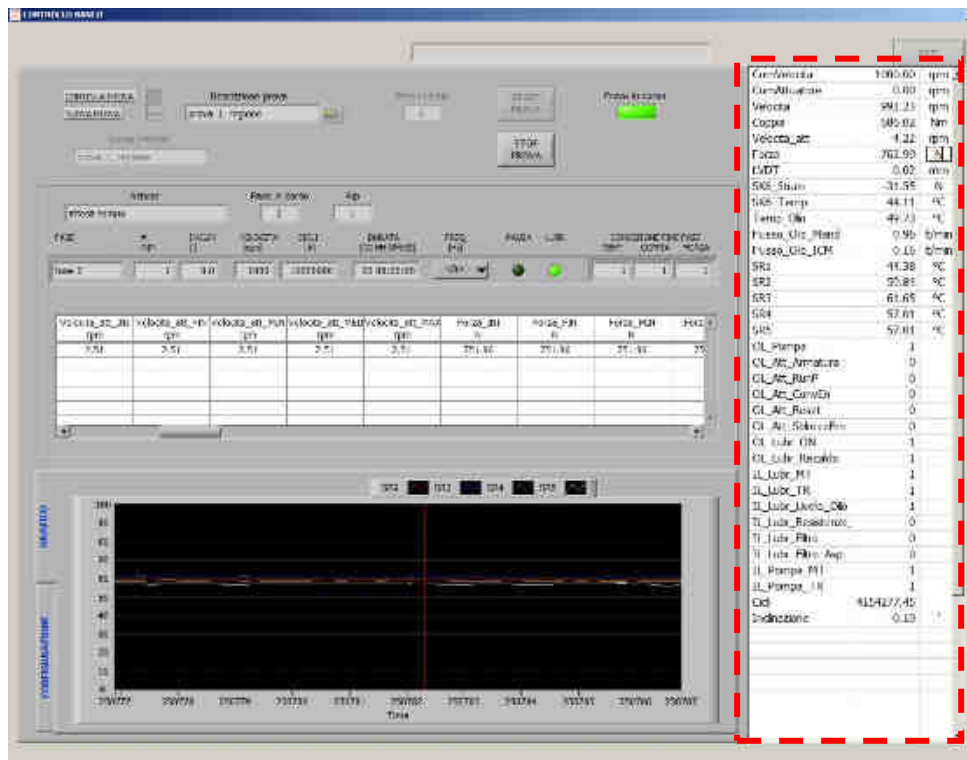


Figure 4.11: screen of the test management

Figure 4.11 shows a screenshot of the program management of tests and in particular it has been highlighted the window from which you can observe the progress of the test run.

#### 4.9) TESTS DESCRIPTION

In this work have been carried out four tests to evaluate the wear development on crowned splined couplings and then to calibrate the first Ruiz parameter.

The operation parameters of the bench for each test are reported in Table 4.3.

Test number	Torque [Nm]	Speed [rpm]	Misalignment [']	Lubrication	Number of cycles
1	700	1500	10	Yes	10M
2	700	1500	0	Yes	10M
3	700	1500	5	Yes	10M
4	700	1500	10	No	10M

Table 4.3: the operation parameters of the bench for the tests

As it can be seen in Table 4.3, the parameters changing in every tests are the misalignment and the presence of lubrication; it is due because, like as shown in the previous chapter, the most significant parameters for the fretting wear and then for the Ruiz method are the sliding and the shear traction that is the multiplication between the COF and the punctual pressure.

#### 4.10) TEST ARTICLE GEOMETRY

The T.A. used are two elements that form a crowned splined coupling; they are:

- a shaft with 26 teeth;
- a hub with 26 teeth.

The hub is the element which imposes an angular misalignment in order to make the test more similar to real conditions; the shaft is the drive element whose motion is provided by the electric motor by means of a transmission belt.

Both elements are constrained to the test bench by means of two flanges and ten screws.

The main features of the coupling are:

1. modulus: 1.27;
2. pressure angle: 30°;
3. number of teeth: 26;

4. material: 42CrMo4;
5. coating surface: nitrated;
6. crowned face width (curvature radius  $r_2$ ): 200 [mm].

The shaft is provided with an inner hole allowing an easy centering on a rod fixed to the test bench.

In the hub instead a series of small holes were obtained for electric cables passing for monitoring various signals during the tests.

The hub has also a circular housing for mounting an O-ring that prevents the leakage of oil in the external environment and creates a sort of dam which allows to have the teeth of the spline coupling always in an oil bath.

In Figure 4.12-4.14 are represented the CAD of the Test article:

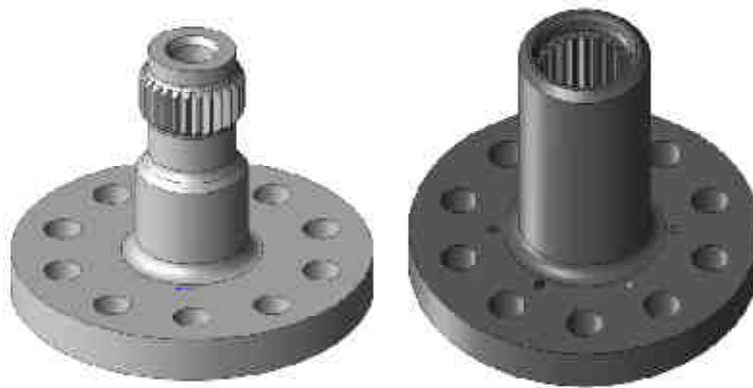


Figure 4.12: representation of the shaft (left) and of the hub (right)

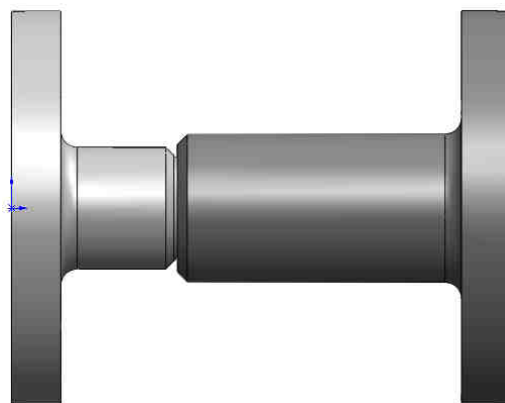


Figure 4.13: spline coupling mounted

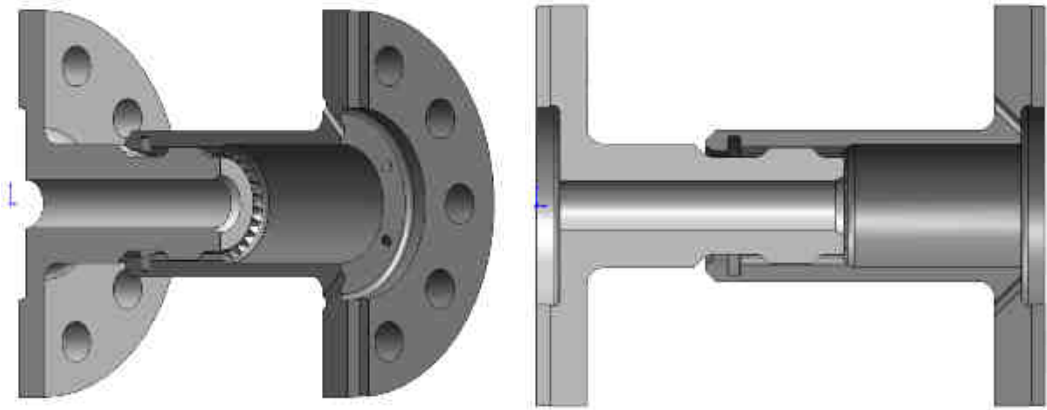


Figure 4.14: section of the Test Article

#### 4.10.1) Hub technical drawing

In Figure 4.15-4.4.17 are reported the technical drawing of the specimen hub.

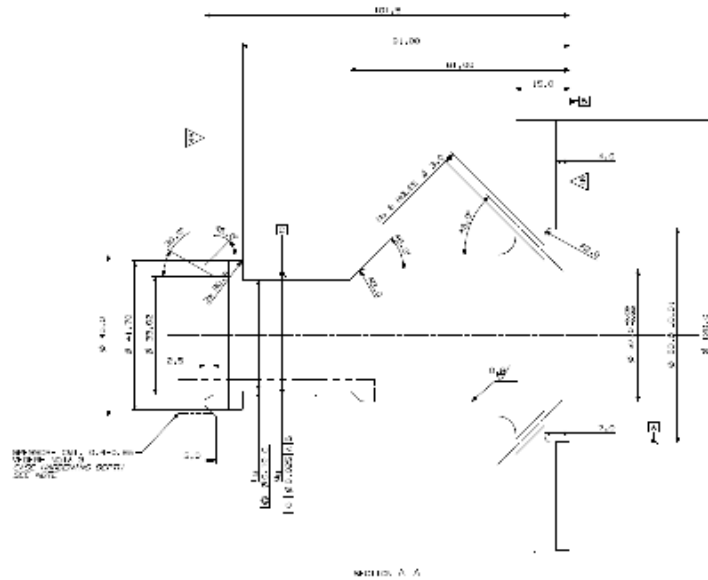


Figure 4.15: technical lateral drawing of the specimen hum

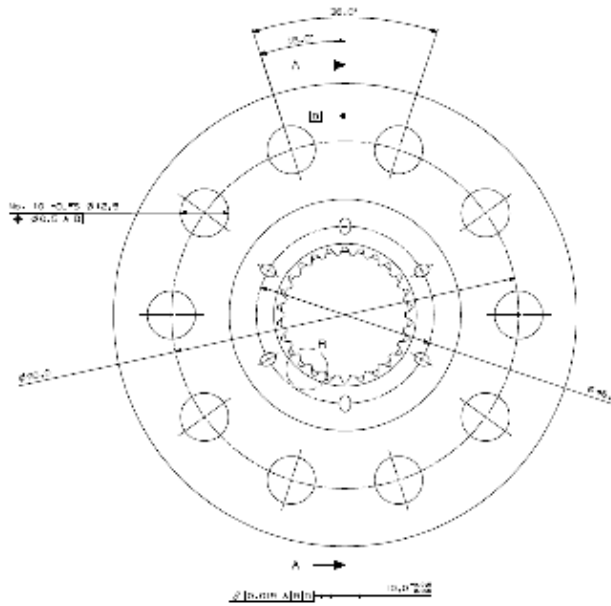


Figure 4.16: technical frontal drawing of the specimen hum

SCANALATO INTERNO	Y	
INTERNAL SPLINE		
CLASSE (SEC. SPEC. "F") (INF.)		5
CLASS (PER SPEC. ) (REF.)		
CENTRAGGIO SUI FIANCHI		
SIDE FIT		
TIPO DI SCANALATO		FILLET ROOT
SPLINE TYPE		
NUMERO DI DENTI		26
NUMBER OF TEETH		
PASSO DIAMETRALE		20/30
DIAMETRAL PITCH		
MODULO		1.27
MODULE		
ANGOLO DI PRESSIONE		30°
PRESSURE ANGLE		
DIAMETRO PRIMITIVO	M.Y.	33.020
PITCH DIA.		
DIAMETRO DI BASE		28.5963
BASE DIA.		
DIAMETRO ESTERNO		35.281+ 35.789
MAJOR DIA.		
DIAMETRO INIZIO EVOLVENTE		34.874 MIN.
FORM DIA.		
DIAMETRO INTERNO	LY.	31.318+ 31.445
MINOR DIA.		
FONDO DENTE A PIENO RACCORDO DI RAGGIO MIN.		0.279
FULL FILLET ROOT WITH MIN RADIUS		
AMPIEZZA CIRCOLARE VANO	{ MIN EFFICACE MIN EFFECTIVE MAX REALE MAX ACTUAL	1.994
CIRCULAR SPACE WIDTH		2.068
LARGHEZZA DI FASCIA		VED. DIS.
FACE WIDTH	TY.	SEE DWG.
QUOTA TRA 2 RULLINI		28.914+ 28.983
MEASUREMENT UNDER 2 PINS		
DIAMETRO RULLINO		2.5
PIN DIA.		
TOLLERANZE:		
TOLERANCES:		
MAX ERRORE DI DIVISIONE ACCUMULATO		0.041
MAX ACCUMULATED SPACING ERROR		
MAX ERRORE INCLINAZIONE DENTI		0.010
MAX LEAD ERROR		
ERRORE DI PROFILO SUL DIAMETRO ESTERNO		+0.005/-0.010
PROFILE ERROR "TIP"		
LARGHEZZA BANDA DI ONDULAZIONE LUNGO L'EVOLVENTE		0.005
WIDTH OF WAVINESS BAND ALONG INVOLUTE		
ERRORE DI PROFILO SUL DIAMETRO DI INIZIO EVOLVENTE		+0.005/-0.010
PROFILE ERROR "TIF"		
ACCOPPIAMENTO SCORREVOLE CON PARTICOLARE		SCANALATO ESTER.
LOOSE FIT WITH PART		EXTERNAL SPLINE

Figure 4.17: Geometrical characteristics of the hub

#### 4.10.2) Shaft technical drawing

In Figure 4.18-4.4.20 are reported the technical drawing of the specimen shaft.

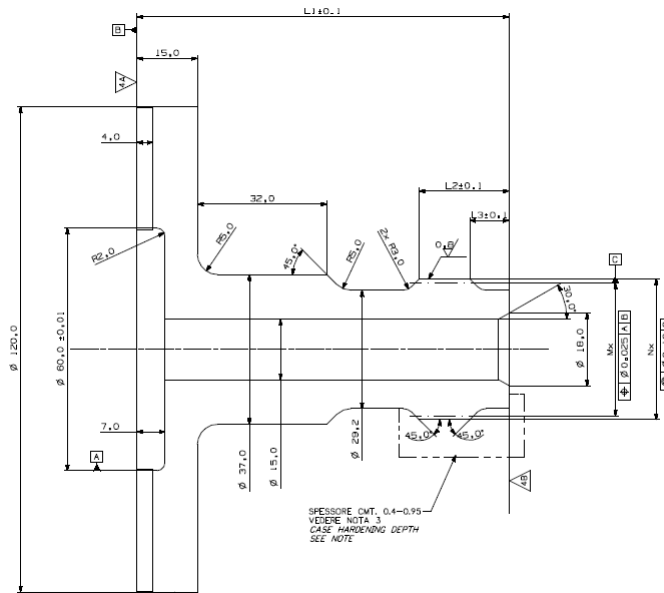


Figure 4.18: technical lateral drawing of the specimen shaft

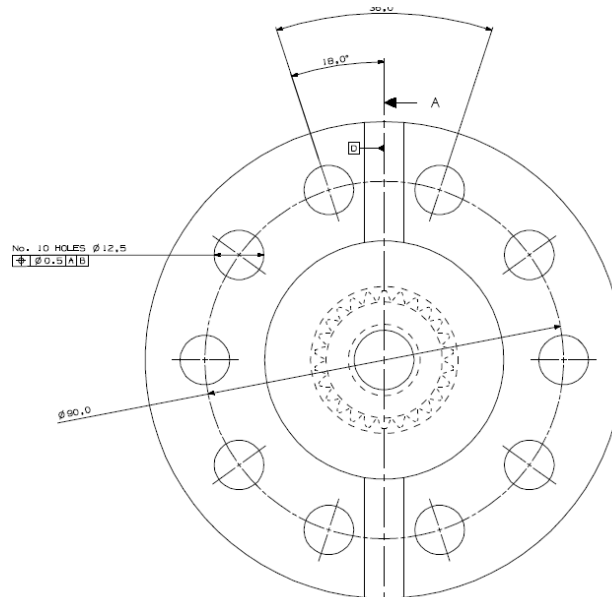


Figure 4.19: technical frontal drawing of the specimen shaft

SCANALATO ESTERNO X	
EXTERNAL SPIRE X	
CENTRAGGIO SUI FIANCHI	
SIDE FIT	
NUMERO DI DENTI	26
NUMBER OF TEETH	
PASSO DIAMETRIALE	20.730
DIAMETRAL PITCH	
ANGOLO DI PRESSIONE	30°
PRESSURE ANGLE	
DIAM. EST. PRIMITIVO	Mx 33.020
PRIM. DIA.	
DIAM. EST. DI BASE	28.896.3
BASE DIA.	
DIAM. EST. LS. UNICO	Nx 34.378 34.727
UNIQUE DIA.	
DIAM. UNO UNICO ESTERNO	31.746
UNIQUE DIA.	
DIAM. EST. INTERNO	22.272 22.600
INT. DIA.	
FONDO DENT. A RIF. RAGGIO DI RAGGIO MIN.	0.005
TOOTH ROOT WITH MIN. RADIUS	
MAX. TITOLAZ.	1.800
MAX. DEGREE	
SPESORE CIRCOLARE DENTE	
CIRCULAR TOOTH THICKNESS	
MAX. RAGGIO	1.636
MAX. RADIUS	
LARGHEZZA DI FASCIA	VED. DISEGNO
FACE WIDTH	SEE DRG.
QUOTA TRA 2 RULLING	36.856 36.858
SPACING OVER 2 ROLLING	
DIAMETRO RULLING	25
ROLLING DIA.	
TOLLERANZE:	
TOLERANCES:	
MAX. ERRORE DI QUOTAZIONE ACCUMULATO	0.041
MAX. ACCUMULATED QUOTING ERROR	
MAX. ERRORE INCLINAZIONE DEN.	0.020
MAX. LEAD ERROR	
ERRORE DI PROFILLO SUL DENTE HO ES. ERRORE	+0.005/ 0.010
PROFILE ERROR HO	
AVV. ZER. BANDA DI DENT. AZIONE UNICO 1. VERTICALE	0.005
ROLLING ON RAISED BAND ALONG ANGLE	
ERRORE DI PROFILLO SUL DENTE HO DL. ERRORE UNICO 1. L	+0.005/ 0.010
PROFILE ERROR HO	
FORMA LRA. C. RING. AB. S. AMERICA	VED. TAB. 14.1
SYMMETRICAL CONTOUR SYSTEM	SEE TABLE 1
ACCORDO SUI N. D. SCHEMI VO. 1 CON PARTI VO. 2	SCHEMA C. D. IN L. 100
COORD. TO DRAWINGS	INTERNAL CODE

Figure 4.20: geometrical characteristics of the shaft

#### 4.10.3) Material of the Test Article

The alloyed steel 42CrMo4 is a heat-treatable steel of average hardenability, suitable for hot purposes until the temperature of 500 [°C], and also has a good adaptability to the nitrating treatment.

Typically the quenched and tempered steels are used for the construction of mechanical parts subjected to static and dynamic loads; they are widely used in mechanical, for shafts of any type, axles, connecting rods, linkages, levers, rods for power hammers, presses columns.

The wide variety of uses, of size and shape of the mechanical parts to which the quenched and tempered steels are intended, requires a careful choice of steel according to the particular stresses to which it will be subjected.

Therefore it is of fundamental importance to know the characteristics of hardenability.

Table 4.4 and table 4.5 shown the characteristic of the material of the Test article

Chemical composition 42CrMo4					
C	Mn	Si	Cr	Ni	Mo
.38-.45	.60-.90	<.40	.90-1.20	Yes	.15-.30

Table 4.4: chemical composition 42CrMo4

D [mm]	R <sub>min</sub> [N/mm <sup>2</sup> ]	R <sub>m</sub> [N/mm <sup>2</sup> ]	A <sub>min</sub> [%]
<16	900	1100-1300	10
16-40	750	1000-1200	11
40-100	650	900-1100	12
100-160	550	800-950	13
160-250	500	750-900	14

Table 4.5: mechanics characteristics of 42CrMo4

To increase the surface hardness, and therefore to have a greater resistance to wear, the splined was subjected to a gas nitrating process with a depth of 0.3-0.4 [mm]: the process consists in bringing the steel at about 500 [°C] and then to introduce nitrogen, which is absorbed by the ferrite on the metal surface and form nitrides, mainly Fe<sub>4</sub>N.

## CHAPTER 5: SPECIMEN SURFACE TOPOGRAPHY

### 5.1) INTRODUCTION

Surface roughness evaluation is very important for many fundamental problems such as friction, contact deformation, heat and electric current conduction, tightness of contact joints and positional accuracy. For this reason surface roughness has been the subject of experimental and theoretical investigations for many decades. The real surface geometry is so complicated that a finite number of parameters cannot provide a full description. If the number of parameters used is increased, a more accurate description can be obtained.

Surface roughness parameters are normally categorized into three groups according to its functionality. These groups are defined as amplitude parameters, spacing parameters and hybrid parameters.

This chapter illustrates the definitions and the mathematical *formulae* for the most important roughness parameters.

In this PhD thesis the main roughness parameters available in literature [85] are used to try to investigate how a specimen, subjected to a wear test, change its surface topography.

### 5.2) THE AMPLITUDE PARAMETERS

Amplitude parameters are the most important parameters to characterize surface topography. They are used to measure the vertical characteristics of the surface deviations. The following sections give a brief description for each parameter.

#### 5.2.1) Arithmetic average height ( $R_a$ )

The arithmetic average height parameter, also known as the centre line average (CLA), is the most universally used roughness parameter for general quality control. It is defined as the average absolute deviation of the roughness irregularities from the mean line over one sampling length as

shown in Figure 5.1. This parameter is easy to define, easy to measure, and gives a good general description of height variations. It does not give any information about the wavelength and it is not sensitive to small changes in profile. The mathematical definition of the arithmetic average height parameter are, respectively, as follows:

$$R_a = \frac{1}{l} \int_0^l |y(x)| dx \quad \text{eq. 5.1}$$

$$R_a = \frac{1}{n} \sum_{i=1}^l |y_i| \quad \text{eq. 5.2}$$

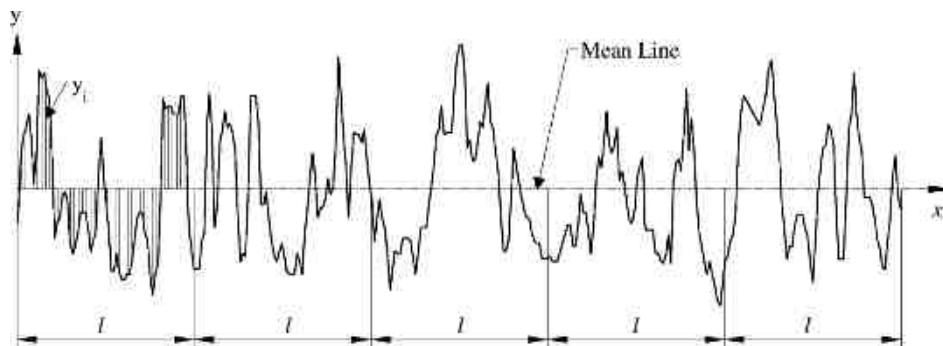


Figure 5.1: definition of the arithmetic average height ( $R_a$ ) [85]

### 5.2.2) Root mean square roughness ( $R_q$ )

This parameter is also known as RMS. It represents the standard deviation of the distribution of surface heights, so it is an important parameter to describe the surface roughness by statistical methods. This parameter is more sensitive than the arithmetic average height ( $R_a$ ) to large deviation from the mean line.

The mathematical definition of this parameter are as follows:

$$R_q = \sqrt{\frac{1}{l} \int_0^l \{y(x)\}^2 dx} \quad \text{eq. 5.3}$$

$$R_q = \sqrt{\frac{1}{n} \sum_{i=1}^l (y_i)^2} \quad \text{eq. 5.4}$$

The RMS mean line is the line that divides the profile so that the sum of the squares of the deviations of the profile height from it is equal to zero.

### 5.2.3) Ten-point height ( $R_z$ )

This parameter is more sensitive to occasional high peaks or deep valleys than  $R_a$ . It is defined by two methods according to the definition system. The International ISO system defines this parameter as the difference in height between the average of the five highest peaks and the five lowest valleys along the assessment length of the profile.

The German DIN system defines  $R_z$  as the average of the summation of the five highest peaks and the five lowest valleys along the assessment length of the profile. Figure 5.2 shows the definition of the ten-point height parameter.

The mathematical definitions of the two types of  $R_z$  are as follows:

$$R_{z(ISO)} = \frac{1}{n} (\sum_{i=1}^n p_i - \sum_{i=1}^n v_i) \quad \text{eq. 5.5}$$

$$R_{z(DIN)} = \frac{1}{2n} (\sum_{i=1}^n p_i + \sum_{i=1}^n v_i) \quad \text{eq. 5.6}$$

where  $n$  is the number of samples along the assessment length.

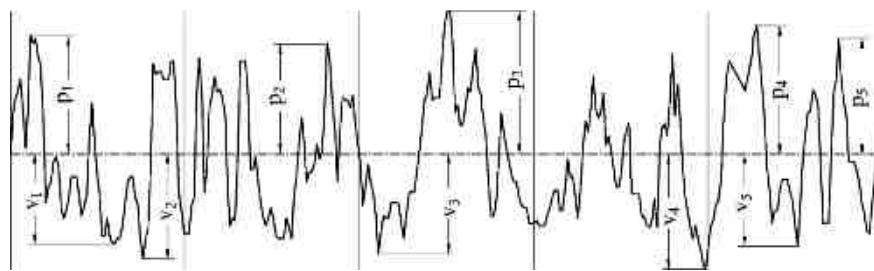


Figure 5.2: definition of the ten-point height parameters ( $R_{z(ISO)}$ ,  $R_{z(DIN)}$ ) [85]

### 5.2.4) Maximum height of peaks ( $R_p$ )

$R_p$  is defined as the maximum height of the profile above the mean line within the assessment length as in Figure 5.3. In the Figure,  $R_{p3}$  represents the  $R_p$  parameter.

### 5.2.5) Maximum depth of valleys ( $R_v$ )

$R_v$  is defined as the maximum depth of the profile below the mean line within the assessment length as shown in Figure 5.3. In the Figure  $R_{v4}$  represents the  $R_v$  parameter.

### 5.2.6) Mean height of peaks ( $R_{pm}$ )

$R_{pm}$  is defined as the mean of the maximum height of peaks ( $R_p$ ) obtained for each sampling length of the assessment length as shown in Figure 5.3. This parameter can be calculated from the following equation:

$$R_{pm} = \frac{1}{n} (\sum_{i=1}^n R_{pi}) \quad \text{eq. 5.7}$$

where n is the number of samples along the assessment length of the profile. From Figure 5.3,  $R_{pm} = (R_{p1} + R_{p2} + R_{p3} + R_{p4} + R_{p5}) / 5$ .

### 5.2.7) Mean depth of valleys ( $R_{vm}$ )

$R_{vm}$  is defined as the mean of the maximum depth of valleys ( $R_v$ ) obtained for each sampling length of the assessment length as shown in Figure 5.3. This parameter can be calculated from the following equation:

$$R_{vm} = \frac{1}{n} (\sum_{i=1}^n R_{vi}) \quad \text{eq. 5.8}$$

where n is the number of samples along the assessment length of the profile. From Figure 5.3,  $R_{vm} = (R_{v1} + R_{v2} + R_{v3} + R_{v4} + R_{v5}) / 5$ .

### 5.2.8) Maximum height of the profile ( $R_t$ or $R_{max}$ )

This parameter is very sensitive to the high peaks or deep scratches.  $R_{max}$  or  $R_t$  is defined as the vertical distance between the highest peak and the lowest valley along the assessment length of the profile. From Figure 5.3,  $R_{max} = R_p + R_v = R_{p3} + R_{v4}$ .

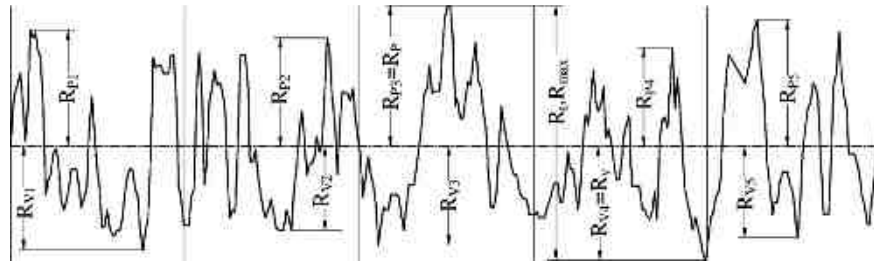


Figure 5.3: definitions of the parameters:  $R_p$ ,  $R_v$ ,  $R_{pm}$ ,  $R_{vm}$ ,  $R_t$  ( $R_{max}$ ) [85]

### 5.2.9) Maximum peak to valley height ( $R_{ti}$ )

$R_{ti}$  is the vertical distance between the highest peak and the lowest valley for each sampling length of the profile. As the assessment length is divided into five sampling lengths, the maximum peak to valley height ( $R_{ti}$ ) can be defined, as shown in Figure 5.4, as follows:

$$R_{ti} = R_{pi} + R_{vi} \quad \text{eq. 5.9}$$

where  $i$  ranges from 1 to 5. From the Figure 5.4,  $R_{t1} = R_{p1} + R_{v1}$ ,  $R_{t2} = R_{p2} + R_{v2} + \dots$  etc.

### 5.2.10) Mean of maximum peak to valley height ( $R_{tm}$ )

$R_{tm}$  is defined as the mean of all maximum peak to valley heights obtained within the assessment length of the profile. From Figure 5.4, the mathematical definition of this parameter is as follows:

$$R_{tm} = \frac{1}{n} (\sum_{i=1}^n R_{ti}) \quad \text{eq. 5.10}$$

where  $n$  is the number of samples along the assessment length of the profile. From the Figure 5.4  $R_{tm} = (R_{t1} + R_{t2} + R_{t3} + R_{t4} + R_{t5}) / 5$ .

### 5.2.11) Largest peak to valley height ( $R_y$ )

This parameter is defined as the largest value of the maximum peak to valley height parameters ( $R_{ti}$ ) along the assessment length. From Figure 5.4,  $R_y = R_{t3}$

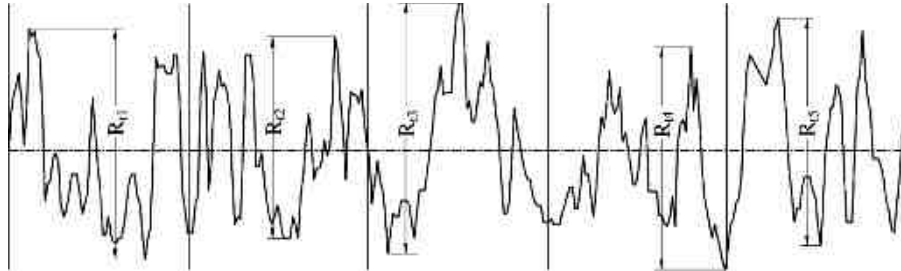


Figure 5.4: definition of the maximum peak to valley height parameters ( $R_{ti}$ ) [85]

### 5.2.12) Third point height ( $R_{3y}$ )

To calculate this parameter, the distance between the third highest peak and the third lowest valley is calculated for each sampling length, then the largest distance is considered as the third point height ( $R_{3y}$ ). From Figure 5.5 the third point height parameter ( $R_{3y}$ ) is the maximum value of the five values of  $R_{3y1}$ ,  $R_{3y2}$ ,  $R_{3y3}$ ,  $R_{3y4}$ ,  $R_{3y5}$ , that is  $R_{3y5}$ .

### 5.2.13) Mean of the third point height ( $R_{3z}$ )

This parameter is the mean of the five third point height parameters ( $R_{3y1}$ ,  $R_{3y2}$ ,  $R_{3y3}$ ,  $R_{3y4}$ , and  $R_{3y5}$ ). As shown in Figure 5.5  $R_{3z}$  is equal to  $(R_{3y1} + R_{3y2} + R_{3y3} + R_{3y4} + R_{3y5})/5$ . The mathematical definition of this parameter is as follows:

$$R_{3z} = \frac{1}{5} (\sum_{i=1}^5 R_{3yi}) \quad \text{eq. 5.11}$$

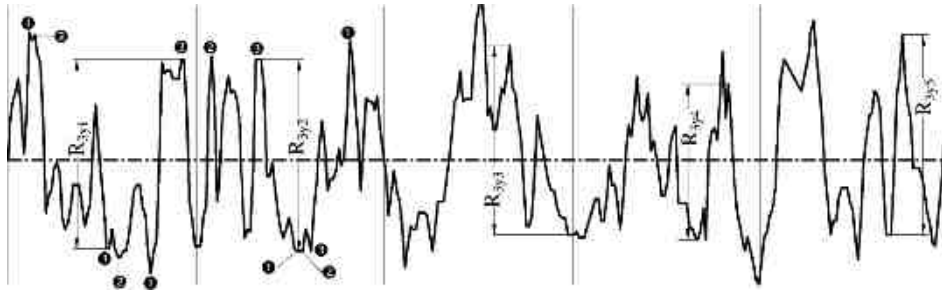


Figure 5.5: definitions of the third point height parameters ( $R_{3y}$ ,  $R_{3z}$ ) [85]

#### 5.2.14) Profile solidity factor ( $k$ )

The profile solidity factor ( $k$ ) is defined as the ratio between the maximum depth of valleys and the maximum height of the profile. The mathematical definition of this parameter is as follows:

$$k = \frac{R_v}{R_{max}} \quad \text{eq. 5.12}$$

#### 5.2.15) Skewness ( $R_{sk}$ )

The skewness of a profile is the third central moment of profile amplitude probability density function, measured over the assessment length. It is used to measure the symmetry of the profile about the mean line. This parameter is sensitive to occasional deep valleys or high peaks. A symmetrical height distribution, i.e. with as many peaks as valleys, has zero skewness. Profiles with peaks removed or deep scratches have negative skewness. Profiles with valleys filled in or high peaks have positive skewness. This is shown in Figure 5.6. The skewness parameter can be used to distinguish between two profiles having the same  $R_a$  or  $R_q$  values but with different shapes.

The value of skewness depends on whether the bulk of the material of the sample is above (negative skewed) or below (positive skewed) the mean line as shown in Figure 5.6. The mathematical formulas used to calculate the skewness of a profile, which has number of points  $N$ , are as follows:

$$R_{sk} = \frac{1}{R_q^3} \int_{-\infty}^{\infty} y^3 p(y) dy \quad \text{eq. 5.13}$$

$$R_{sk} = \frac{1}{NR_q^3} (\sum_{i=1}^N Y_i^3) \quad \text{eq. 5.14}$$

where  $R_q$  is the RMS roughness parameter and  $Y_i$  the height of the profile at point number  $i$ .

The skewness parameter can be used to differentiate between surfaces, which have different shapes and have the same value of  $R_a$ . In Figure 5.6, although the two profiles may have the same value of  $R_a$ , they have different shapes.

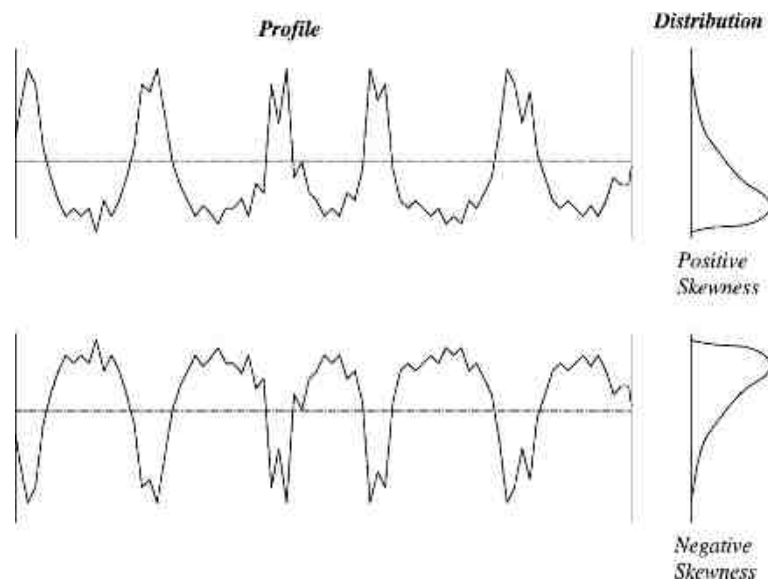


Figure 5.6: definition of skewness ( $R_{sk}$ ) and the amplitude distribution curve [85]

#### 5.2.16) Kurtosis ( $R_{ku}$ )

Kurtosis coefficient is the fourth central moment of profile amplitude probability density function, measured over the assessment length. It describes the sharpness of the probability density of the profile.

If  $R_{ku} < 3$  the distribution curve is said to be platykurtic and has relatively few high peaks and low valleys.

If  $R_{ku} > 3$  the distribution curve is said to be leptokurtic and has relatively many high peaks and low valleys. Figure 5.7 shows these two types of kurtosis.

The mathematical formula used to calculate the kurtosis of a profile with a number of points  $t$  are as follows:

$$R_{ku} = \frac{1}{R_q^4} \int_{-\infty}^{\infty} y^4 p(y) dy \quad \text{eq. 5.15}$$

$$R_{ku} = \frac{1}{NR_q^4} (\sum_{i=1}^N Y_i^4) \quad \text{eq. 5.16}$$

where  $R_q$  is the RMS roughness parameter and  $Y_i$  the height of the profile at point number  $i$ .

The skewness parameter can also be used to differentiate between surfaces, which have different shapes and have the same value of  $R_a$ . In Figure 5.7, although the two profiles may have the same value of  $R_a$ , they have different shapes.

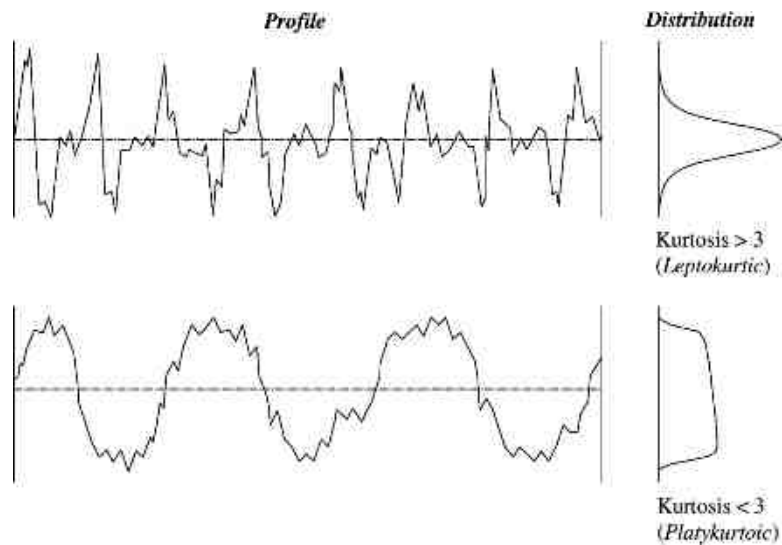


Figure 5.7: definition of kurtosis ( $R_{ku}$ ) parameter [85]

### 5.2.17) Amplitude density function (ADF)

The term amplitude density corresponds exactly to the term probability density in statistics. The ADF represents the distribution histogram of the profile heights. It can be found by plotting the density of the profile heights

on the horizontal axis and the profile heights itself on the vertical axis as shown in Figure 5.8.

To calculate the density of the profile heights, the amplitude scale is divided into small parts  $\delta_y$ . The measure of the amplitude values found within  $\delta_y$ , can be made by calculating all amplitude values between  $y$  and  $y + \delta_y$  relative to the assessment length of the profile. The Amplitude density is hence defined by the following equation:

$$p(y) = \lim_{\delta_y \rightarrow 0} \frac{P(y, y + \delta_y)}{\delta_y} \quad \text{eq. 5.17}$$

For surfaces produced by a truly random process, the ADF would be a Gaussian distribution of surface heights given by the following equation:

$$ADF(y) = \sqrt{2\pi R_q^2} \exp\left(\frac{-y^2}{2R_q^2}\right) \quad \text{eq. 5.18}$$

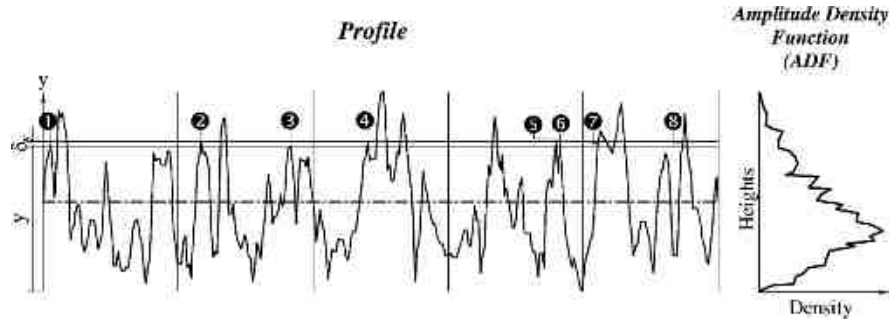


Figure 5.8: the ADF [85]

### 5.2.18) Auto correlation junction (ACF)

The ACF describes the general dependence of the values of the data at one position to their values at another position. It is considered a very useful tool for processing signals because it provides basic information about the relation between the wavelength and the amplitude properties of the surface. The ACF can be considered as a quantitative measure of the similarity between a laterally shifted and an unshifted version of the profile. The mathematical representations of this function are as follows:

$$ACF(\delta_x) = \frac{1}{L} \int_0^L y(x)y(x + \delta_x) dx \quad \text{eq. 5.19}$$

$$ACF(\delta_x) = \frac{1}{N-1} \sum_{i=1}^N y_i y_{i+1} \quad \text{eq. 5.20}$$

where  $\delta_x$  is the shift distance and  $y_i$  the height of the profile at point number  $i$ .

The ACF can be normalized to have a value of unity at a shift distance of zero. This suppresses any amplitude information in the ACF but allows a better comparison of the wavelength information in various profiles.

#### 5.2.19) Correlation length ( $\beta$ )

This parameter is used to describe the correlation characteristics of the ACF. It is defined as the shortest distance in which the value of the ACF drops to a certain fraction, usually 10% of the zero shift value. Points on the surface profile that are separated by more than a correlation length may be considered as uncorrelated, i.e. portions of the surface represented by these points were produced by separate surface forming events. Correlation lengths may range from the infinite correlation length for a perfectly periodic wavelength to zero for a completely random waveform.

#### 5.2.20) Power spectral density (PSD)

The PSD function is an important function for characterizing both the asperity amplitudes and spacing. It is calculated by Fourier decomposition of the surface profile into its sinusoidal component spatial frequency ( $f$ ).

For a 2D surface profile it can be calculated from the following equation:

$$PSD(f) = \frac{1}{L} \left| \int_0^L y(x) \exp(-i2\pi f x) dx \right|^2 \quad \text{eq. 5.21}$$

$$PSD(f) = \frac{1}{N-1} \left[ \sum_{i=0}^{N-1} y_i e^{\frac{-j2\pi\beta i}{N}} \right]^2 \quad \text{eq. 5.22}$$

where  $\beta$  is the correlation length.

### 5.3) THE SPACING PARAMETERS

The spacing parameters are those which measure the horizontal characteristics of the surface deviations. The spacing parameters are very important in some manufacturing operations, such as pressing sheet steel. In such case, evaluating the spacing parameters is necessary to obtain consistent lubrication when pressing the sheets, to avoid scoring and to prevent the appearance of the surface texture on the final product. One of the spacing parameter is the *peak spacing*, which can be an important factor in the performance of friction surfaces.

#### 5.3.1) High spot count (HSC):

The HSC parameter is defined as the number of high regions of the profile above the mean line, or above a line parallel to the mean line, per unit length along the assessment length. Figure 5.9 shows how to calculate the HSC parameter above a selected level. The profile shown in the Figure has eight HSC.

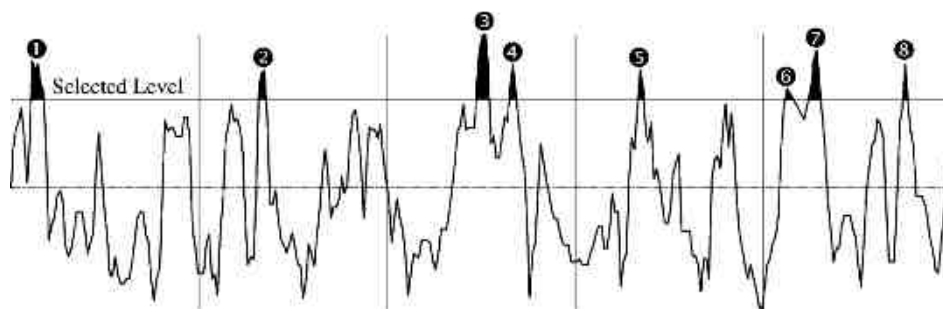


Figure 5.9: calculating HSC above a selected level [85]

#### 5.3.2) Peak count ( $P_c$ )

The importance of the peak count parameter appears in some manufacturing processes such as forming, painting, or coating surfaces. It is defined as the number of local peaks, which is projected through a selectable band located above and below the mean line by the same distance. The number of peak

count is determined along the assessment length and the result is given in peaks per centimeter. If the assessment length is less than 1 cm, the results should be multiplied by a factor to get the peak count per centimeter.

As shown in Figure 5.10 the peak count is determined only for the closed areas of the profile, in which the profile intersects each the upper and the lower bands in two points at least. The profile shown in the Figure 5.10 has four peak counts.

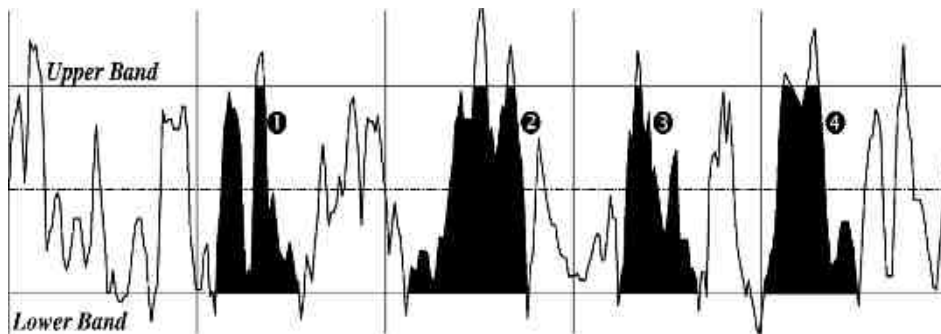


Figure 5.10: calculating the peak count ( $P_c$ ) parameter within a selected band [85]

### 5.3.3) Mean spacing of adjacent local peaks (S)

This parameter is defined as the average spacing of adjacent local peaks of the profile measured along the assessment length. The local peak is defined as the highest part of the profile measured between two adjacent minima and is only measured if the vertical distance between the adjacent peaks is greater than or equal to 10% of the  $R_t$  of the profile. Figure 5.11 shows how to measure this parameter. This parameter can be calculated from the following equation:

$$S = \frac{1}{N} \sum_{i=1}^n S_i \quad \text{eq. 5.23}$$

where N is the number of local peaks along the profile.

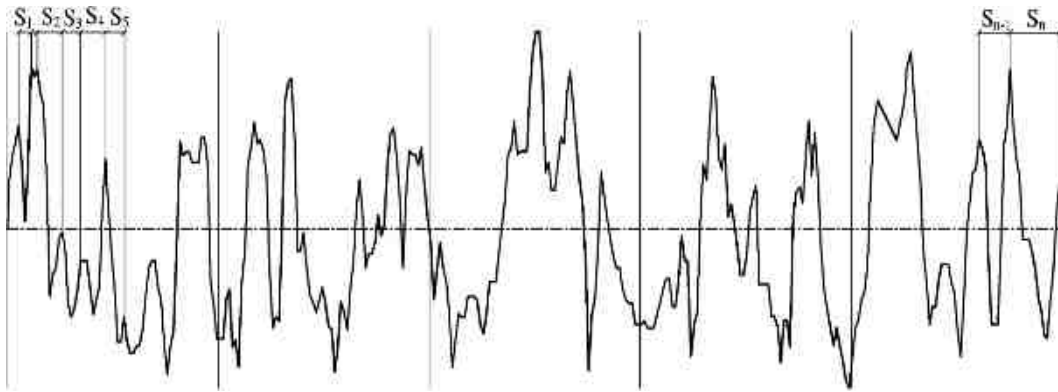


Figure 5.11: calculating the mean spacing of adjacent local peaks (S) [85]

#### 5.3.4) Mean spacing at mean line ( $S_m$ )

This parameter is defined as the mean spacing between profile peaks at the mean line and is denoted as ( $S_m$ ). The profile peak is the highest point of the profile between upwards and downwards crossing the mean line. Figure 5.12 shows how to measure the mean spacing at mean line parameter.

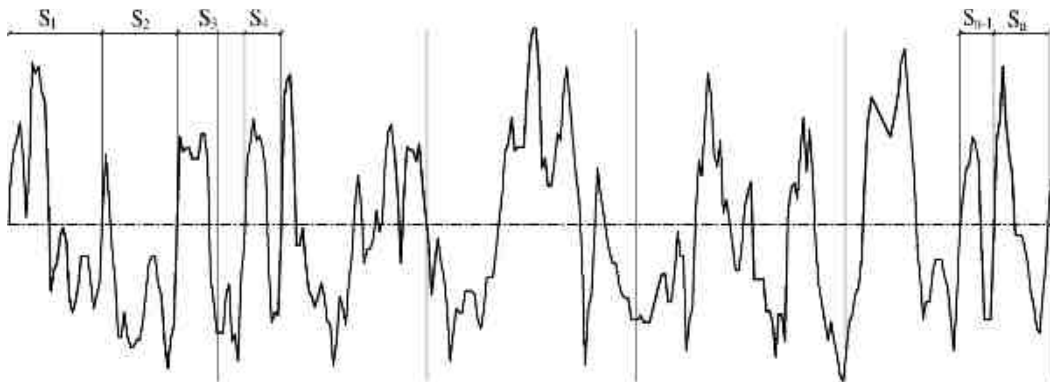


Figure 5.12: calculating the mean spacing at mean line ( $S_m$ ) [85]

This parameter can be calculated from the following equation:

$$S_m = \frac{1}{N} \sum_{i=1}^n S_i \quad \text{eq. 5.24}$$

where N is the number of profile peaks at the mean line.

The difference between the two types of mean spacing parameters, S and  $S_m$ , is that the first parameter (S) is measured at the highest peaks of the profile, whilst the second parameter ( $S_m$ ) is measured at the intersection of the profile

with the mean line.

### 5.3.5) Number of intersections of the profile at the mean line ( $n_{(0)}$ )

This parameter calculates the number of intersections of the profile with the mean line measured for each centimeter length of the profile. As shown in Figure 5.13, the number of intersections of the profile at the mean line can be calculated from the following equation:

$$n_{(0)} = \frac{1}{L} \sum_{i=1}^n c_i \quad \text{eq. 5.25}$$

where L is the profile length (in cm).

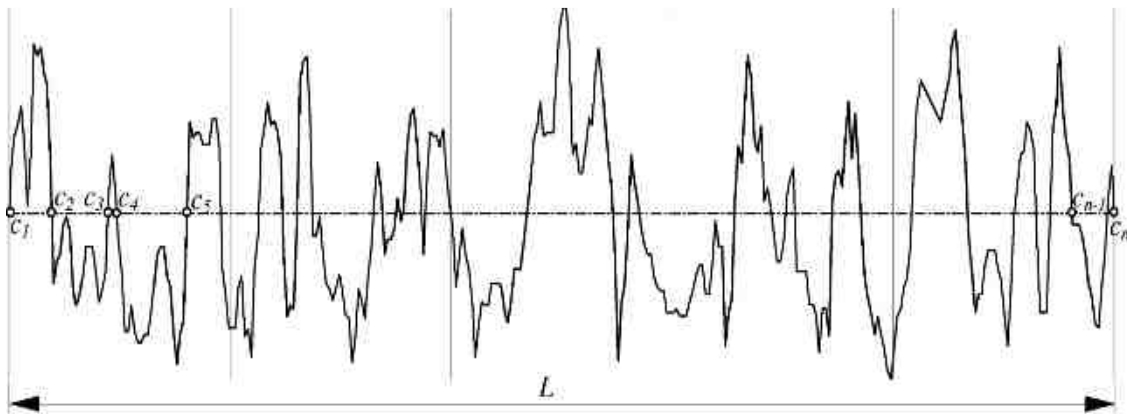


Figure 5.13: calculating the number of intersections of the profile at mean line  
[85]

### 5.3.6) Number of peaks in the profile (m)

This parameter calculates the number of peaks of the profile per unit length (centimeter). Peaks are counted only when the distance between the current peak and the preceding one is greater than 10% of the maximum height of the profile ( $R_t$ ). In Figure 5.14 the three little peaks, which follow the peaks  $m_2$ ,  $m_3$  and  $m_4$  are neglected because the distance between each peak and the preceding one is too small.

The number of peaks can be calculated from the following equation:

$$m = \frac{1}{L} \sum_{i=1}^n m_i \quad \text{eq. 5.26}$$

where L is the profile length (in cm).

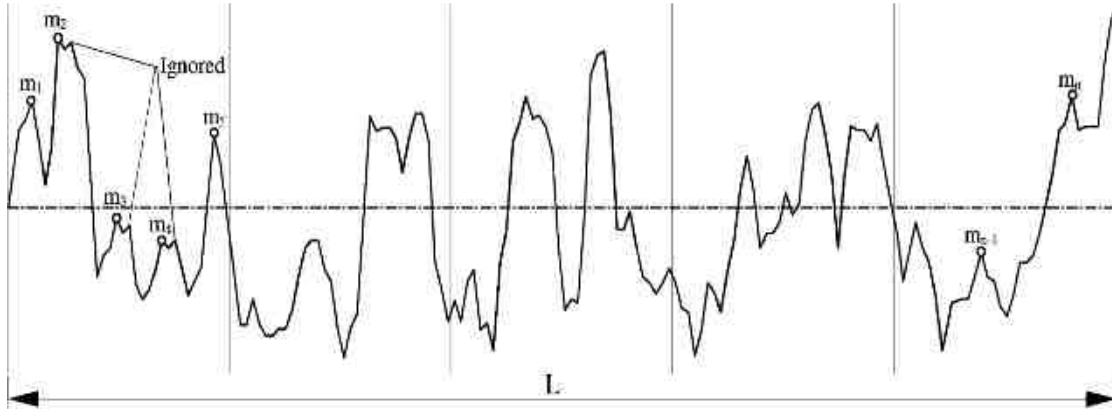


Figure 5.14: calculating the number of peaks along the profile [85]

### 5.3.7) Number of inflection points (g)

This parameter calculates the number of inflection points of the profile per unit length (centimeter). An inflection point occurs when the profile changes its direction at any point as shown in Figure 5.15. This parameter can be calculated from the following equation:

$$g = \frac{1}{L} \sum_{i=1}^n g_i \quad \text{eq. 5.27}$$

where L is the profile length (in cm).

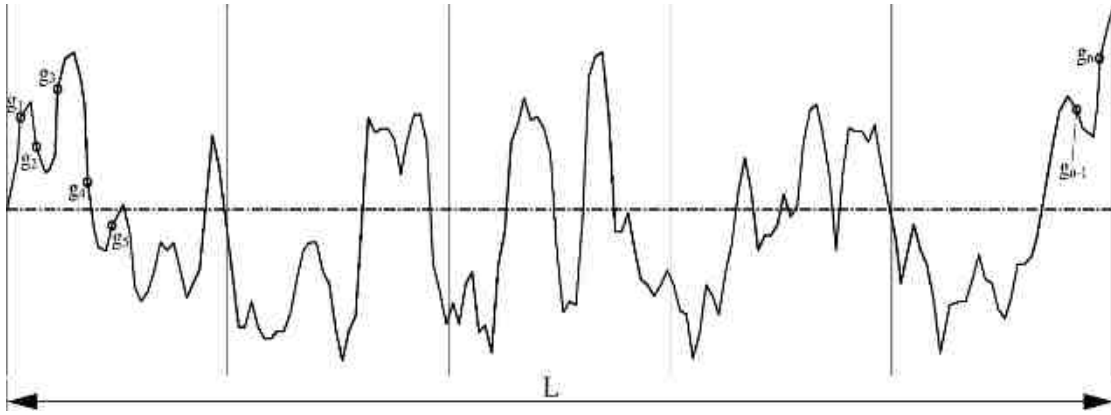


Figure 5.15: calculating the number of inflection points along the profile [85]

### 5.3.8) Mean radius of asperities ( $r_p$ )

The mean peak radius of curvature parameter is defined as the average of the principle curvatures of the peaks within the assessment length. This parameter can be calculated by calculating the radius of curvature for each peak along the profile, then calculating the average of these radii of curvatures.

The radius of curvature for a peak ( $r_{pi}$ ) can be calculated from the following equation:

$$r_{pi} = \frac{2y_i - y_{i-1} - y_{i+1}}{l^2} \quad \text{eq. 5.28}$$

where  $y_i$  is the height of the peak at which the peak radius of curvature ( $r_{pi}$ ) is to be calculated,  $y_{i-1}$  the height of the preceding peak, and  $y_{i+1}$  the height of the next peak. The mean peak radius of curvature ( $r_p$ ), then can be calculated from the following equation:

$$r_p = \frac{1}{n-2} \sum_{i=1}^{n-2} \frac{1}{r_{pi}} \quad \text{eq. 5.29}$$

#### 5.4) THE HYBRID PARAMETERS

The hybrid property is a combination of amplitude and spacing. Any changes, which occur in either amplitude or spacing, may have effects on the hybrid property. In tribology analysis, surface slope, surface curvature and developed interfacial area are considered to be important factors, which influence the tribological properties of surfaces. The following sections describe the most common hybrid parameters.

##### 5.4.1) Profile slope at mean line ( $\gamma$ )

This parameter represents the profile slope at the mean line. It can be calculated by calculating the individual slopes of the profile at each intersection with mean line, then calculating the average of these slopes as shown in Figure 5.16. The numerical equation for calculating the profile slope at the mean line is as follows:

$$\gamma = \frac{1}{n-2} \sum_{i=1}^{n-1} \tan^{-1} \left( \frac{\delta y_i}{\delta x_i} \right) \quad \text{eq. 5.30}$$

where n is the total number of intersections of the profile with the mean line along the assessment length.

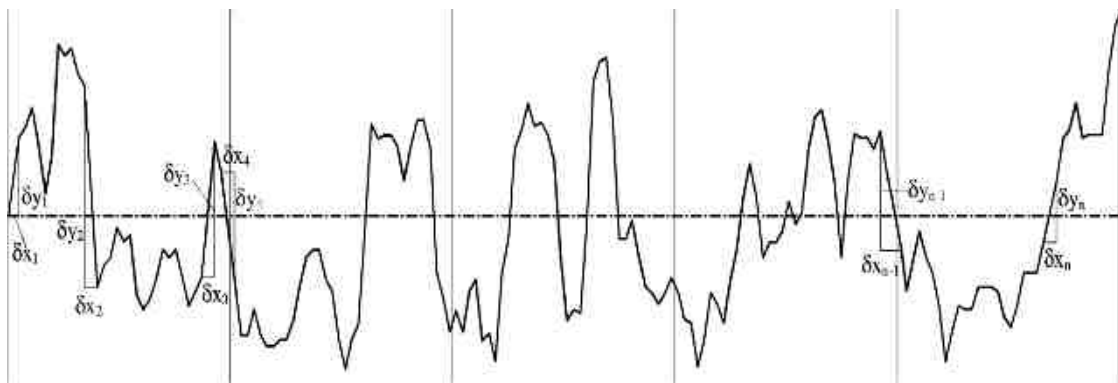


Figure 5.16: calculating the profile slope at mean line [85]

##### 5.4.2) Mean slope of the profile ( $\Delta_a$ )

This parameter is defined as the mean absolute profile slope over the

assessment length. Many mechanical properties such as friction, elastic contact, reflectance, fatigue crack initiation and hydrodynamic lubrication affect this parameter. This parameter can be calculated by calculating all slopes between each two successive points of the profile, then calculating the average of these slopes. As shown in Figure 5.17, the mathematical formulas of calculating the mean slope parameter are as follows:

$$\Delta_a = \frac{1}{L} \int_0^L \left| \frac{dy}{dx} \right| dx \quad \text{eq. 5.31}$$

$$\Delta_a = \frac{1}{n-1} \sum_{i=1}^{n-1} \frac{\delta_{yi}}{\delta_{xi}} \quad \text{eq. 5.32}$$

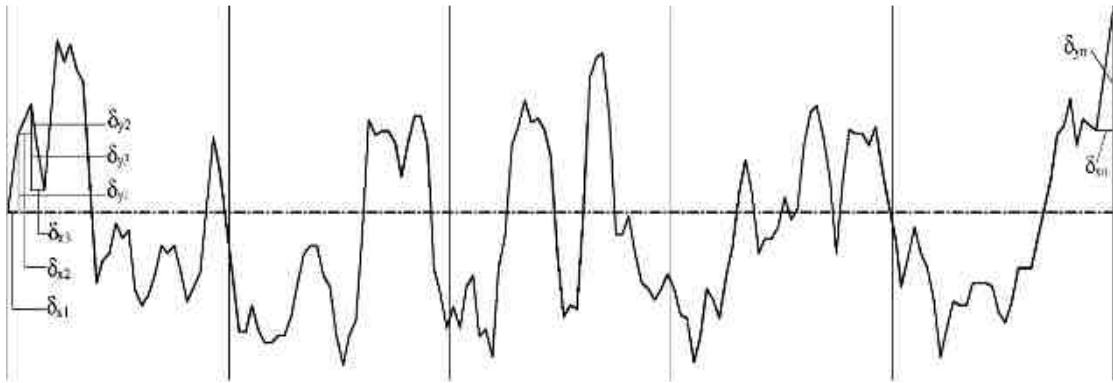


Figure 5.17: calculating the mean slope of the profile [85]

#### 5.4.3) RMS slope of the profile ( $\Delta_q$ )

This parameter is the root mean square of the mean slope of the profile. The mathematical formulas for calculating this parameter are as follows:

$$\Delta_q = \sqrt{\frac{1}{L} \int_0^L (\vartheta(x) - \bar{\vartheta})^2 dx} \quad \text{eq. 5.33}$$

$$\bar{\vartheta} = \frac{1}{L} \int_0^L \vartheta(x) dx \quad \text{eq. 5.34}$$

$$\Delta_q = \sqrt{\frac{1}{n-1} \sum_{i=1}^{n-1} \left( \frac{\delta_{yi}}{\delta_{xi}} - \theta_m \right)^2} \quad \text{eq. 5.35}$$

$$\theta_m = \frac{1}{n-1} \sum_{i=1}^{n-1} \left( \frac{y_i - y_{i-1}}{x_i - x_{i-1}} \right) \quad \text{eq. 5.36}$$

#### 5.4.4) Average wavelength ( $\lambda_a$ )

The average wavelength parameter is a measure of the spacing between local peaks and valleys, taking into consideration their relative amplitudes and individual spatial frequencies.

This parameter can be calculated from the following equation:

$$\lambda_a = \frac{2\pi R_a}{\Delta_a} \quad \text{eq. 5.37}$$

where  $R_a$  is the arithmetic average height and  $\Delta_a$  the mean slope of the profile.

#### 5.4.5) RMS wave length ( $\lambda_q$ )

The RMS wavelength parameter is similar to the average wavelength ( $\lambda_a$ ) parameter. It is defined as the root mean of the measure of the spacing between local peaks and valleys, taking into consideration their relative amplitudes and individual spatial frequencies. It can be calculated from the following equation:

$$\lambda_q = \frac{2\pi R_q}{\Delta_q} \quad \text{eq. 5.38}$$

#### 5.4.6) Relative length of the profile ( $l_0$ )

The relative length of the profile ( $l_0$ ) is estimated by calculating the lengths of the individual parts of the profile then dividing the summation of these lengths by the assessment length as shown in Figure 5.18. This parameter can be calculated from the following equation:

$$l_0 = \frac{1}{L} \sum_{i=1}^n l_i \quad \text{eq. 5.39}$$

where  $l_i$  is the length of line number  $i$  in the profile, and it can be calculated from the following equation:

$$l_i = \sqrt{(y_{i+1} - y_i)^2 + \delta_{xi}^2} \quad \text{eq. 5.40}$$

where  $y_i$  is the profile height at point number  $i$ , and  $\delta_{xi}$  the horizontal distance between each two successive points.

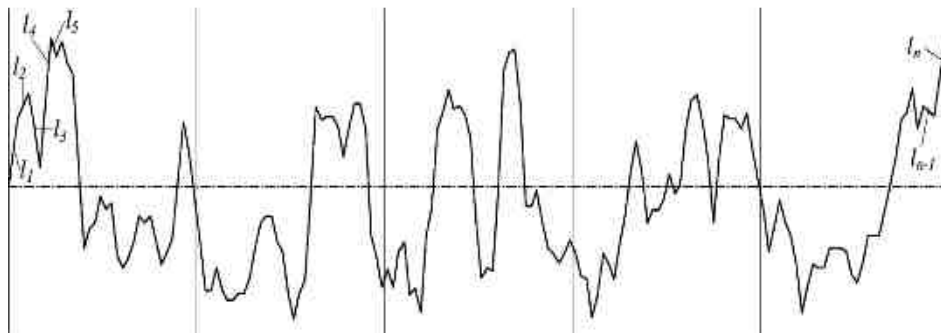


Figure 5.18: calculating the relative length the profile ( $l_0$ ) [85]

#### 5.4.7) Bearing area length ( $t_p$ ) and bearing area curve

The bearing line length parameter is defined as the percentage of solid material of the profile lying at a certain height. This parameter is a useful indicator of the effective contact area as the surface wear. From Figure 5.19, the bearing area length can be calculated from the following equation:

$$l_0(\%) = \frac{1}{L} \sum_{i=1}^n l_i \quad \text{eq. 5.41}$$

where  $L$  is the assessment length of the profile.

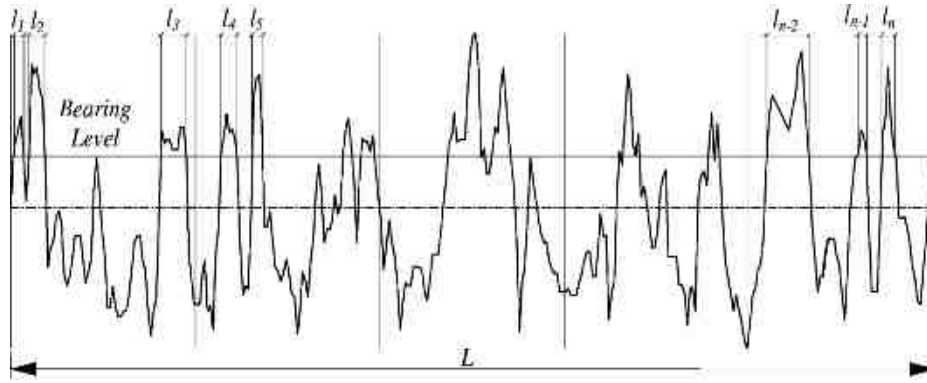


Figure 5.19: calculating the bearing area length ( $t_p$ ) of the profile [85]

By calculating the bearing line length at different heights of the profile, the bearing area curve (BAC) can be drawn, as shown in Figure 5.20.

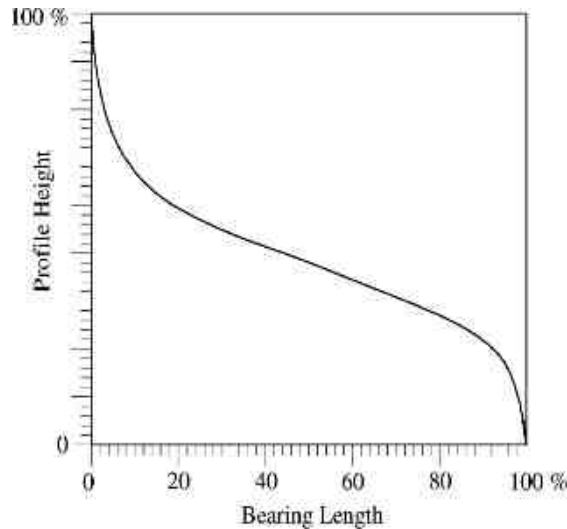


Figure 5.20: the BAC of a profile [85]

The horizontal axis represents the bearing area lengths as a percent from the total assessment length the profile and the vertical axis represents the heights of the profile.

The interpretation of the BAC is that if the surface worn down to a certain height the appropriate Figure would represent the fraction of solid contact at that height.

The bearing curve has the S-shape appearance for many surfaces. It represents the cumulative form of the height distribution histogram.

#### 5.4.8) Steepness factor of the profile ( $S_f$ )

The steepness factor of the profile is defined as the ratio between the arithmetic average height ( $R_a$ ) and the mean spacing of the profile ( $S_m$ ). It can be calculated from the following equation:

$$S_f = \frac{R_a}{S_m} \quad \text{eq. 5.42}$$

#### 5.4.9) Waviness factor of the profile ( $W_f$ )

The Waviness factor of the profile is defined as the ratio between the total range of the entire profile and the arithmetic average height ( $R_a$ ). From Figure 5.18 this parameter can be calculated from the following equation:

$$W_f = \frac{1}{R_a} \sum_{i=1}^{n-1} l_i \quad \text{eq. 5.43}$$

where  $n$  is the number of points along the profile.

#### 5.4.10) Roughness height uniformity ( $H_u$ )

The roughness height uniformity of a profile ( $H_u$ ) is defined as the standard deviations of the individual height values of the profile constituting the arithmetic average height ( $R_a$ ). To calculate this parameter the standard deviation is calculated for the profile heights in each sampling length, then the average of the standard deviations is taken. With reference to Figure 5.1, the ( $H_u$ ) parameter can be calculated from the following equation:

$$H_u = \frac{1}{NS} \sum_{i=0}^{NS-1} S.D. (y_{i \cdot NPS+1}, y_{i \cdot NPS+2}, y_{i \cdot NPS+3}, \dots, y_{i \cdot NPS+NPS}) \quad \text{eq. 5.44}$$

where  $NS$  is the number of samples along the assessment length,  $NPS$  the number of points in each sample,  $y_{i \cdot NPS+\dots}$  the profile's height at point number ( $i \cdot NPS + NPS$ ).

#### 5.4.11) Roughness height skewness ( $H_s$ )

The roughness height skewness ( $H_s$ ) of a profile is defined as the median of the histogram height values divided by the arithmetic average height ( $R_a$ ). To calculate this parameter the median is calculated for the profile heights in each sampling length, then the average of the medians is taken and divided by  $R_a$ .

With reference to Figure 5.1, the ( $H_s$ ) parameter can be calculated from the following equation:

$$H_s = \frac{1}{NS R_a} \sum_{i=0}^{NS-1} \text{median}(y_{i \cdot NPS+1}, y_{i \cdot NPS+2}, y_{i \cdot NPS+3}, \dots, y_{i \cdot NPS+NPS}) \quad \text{eq. 5.45}$$

where NS, NPS,  $y_{i \cdot NPS+\dots}$  are defined as in the previous section.

#### 5.4.12) Roughness pitch uniformity ( $P_u$ )

The roughness pitch uniformity ( $P_u$ ) of a profile is defined as the standard deviation of the individual mean spacing values constituting the mean spacing parameter ( $S_m$ ). With reference to Figure 5.12, the roughness pitch uniformity parameter can be calculated from the following equation:

$$P_u = S.D. (S_1, S_2, S_3, \dots, S_n) \quad \text{eq. 5.46}$$

#### 5.4.13) Roughness pitch skewness ( $P_s$ )

The roughness pitch skewness ( $P_s$ ) of a profile is defined as the median of the mean spacing values, along the profile, divided by the mean spacing parameter ( $S_m$ ).

With reference to Figure 5.12, the roughness pitch skewness parameter can be calculated from the following equation:

$$P_s = \text{median}(S_1, S_2, S_3, \dots, S_n) \quad \text{eq. 5.47}$$

### 5.5) SURFACE ROUGHNESS TESTER ALPA-SM RT 70

The surface roughness tester (Figure 5.21) is an instrument that allows the measurement of micro irregularities which presents a surface relative to its nominal profile.

It is composed by three parts:

- Electric unit
- Translator
- touch probe



Figure 5.21: surface roughness tester RT-70

#### 5.5.1) Profile acquisition

Once the measurement by the surface roughness tester is finished, the data is ready to be acquired by the software.

To acquire the data obtained by the touch probe, a dedicated software was used.

Thanks to it, it is possible to analyze the surface profile (filtered or not), the bearing area curve (BAC) and several roughness parameters (Figure 5.22).

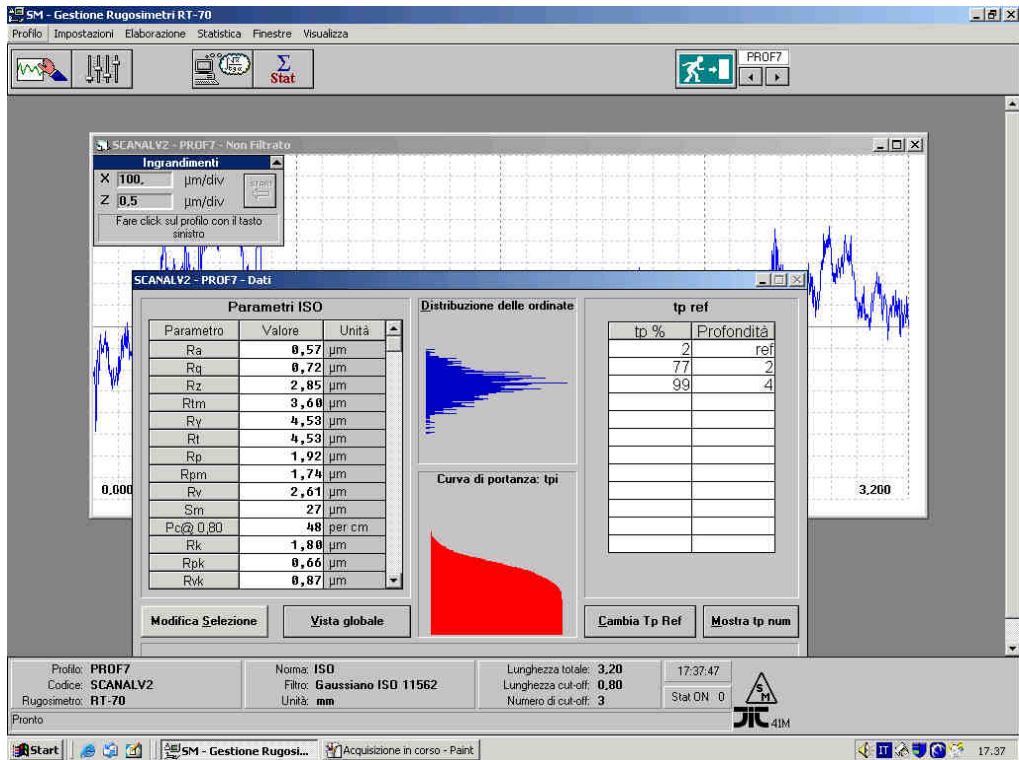


Figure 5.22: RT-70 software

### 5.5.2) Profile exportation

When the profile acquisition is ended, it is possible to analyze the data by the software of the roughness tester or it is possible to export the data (Figure 5.23), by a file.dat, and use them with another program, like Excel.



Figure 5.23: profile exportation

### 5.5.3) Profile data elaboration

To compare and to analyze the topography of the teeth surface of the Test Article before and after a wear test, a dedicated Excel sheet was created (Figure 5.24).

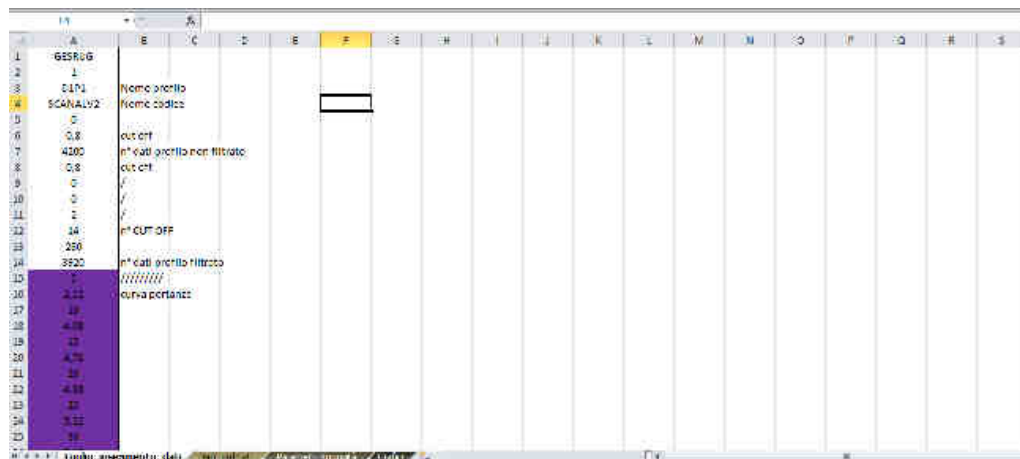


Figure 5.24 Inserimento dati su foglio di calcolo

Once entered the roughness tester data, automatically roughness parameters given by the instrument and calculated by the equations shown previously will be displayed (Figure 5.25).

	Parametri	da Rugosimetro	Calcolati
Altezza media aritmetica	Ra [ $\mu\text{m}$ ]	1,47	1,48
Radice quadratica media della rugosità	Rq [ $\mu\text{m}$ ]	2,16	2,16
Altezza dei dieci punti	Rz(ISO) [ $\mu\text{m}$ ]	0	/
Media dei picchi massimi in riferimento alle valli	Rtm [ $\mu\text{m}$ ]	8,61	/
Picco più alto rispetto alla valle	Ry [ $\mu\text{m}$ ]	17,16	/
Massima altezza del profilo	Rt [ $\mu\text{m}$ ]	17,43	17,43
Altezza massima dei picchi	Rp [ $\mu\text{m}$ ]	6,27	6,27
Altezza media dei picchi	Rpm [ $\mu\text{m}$ ]	3,9	3,90
Massima profondità delle valli	Rv [ $\mu\text{m}$ ]	11,16	11,16
Spaziatura media rispetto alla linea media	Sm [ $\mu\text{m}$ ]	0,59	/
Conto dei picchi	Pc [picchi/cm]	43	/
Profondità della rugosità della zona di lavoro	Rk [ $\mu\text{m}$ ]	3,3	/
Altezza dei picchi ridotta	Rpk [ $\mu\text{m}$ ]	3,42	/
Profondità delle valli ridotta	Rvk [ $\mu\text{m}$ ]	4,23	/
	Mr1 (%)	12	/
	Mr2 (%)	84	/
Asimmetria	Rsk	-0,72	-0,69
	Rku	/	6,15
RMS della pendenza del profilo	$\Delta q$ [rad]	/	0,197
Pendenza media del profilo	$\Delta a$ [rad]	/	0,007
Fattore di solidità del profilo	k	/	0,64
Rilevamento della lunghezza dell'area e della curvatura dell'area	tp (%)	/	0,07

Figure 5.25: roughness parameters comparison

With the Excel sheet is possible to analyze the filtered and the non filtered profile, the bearing area curve and the undulation as shown in Figure 5.26.

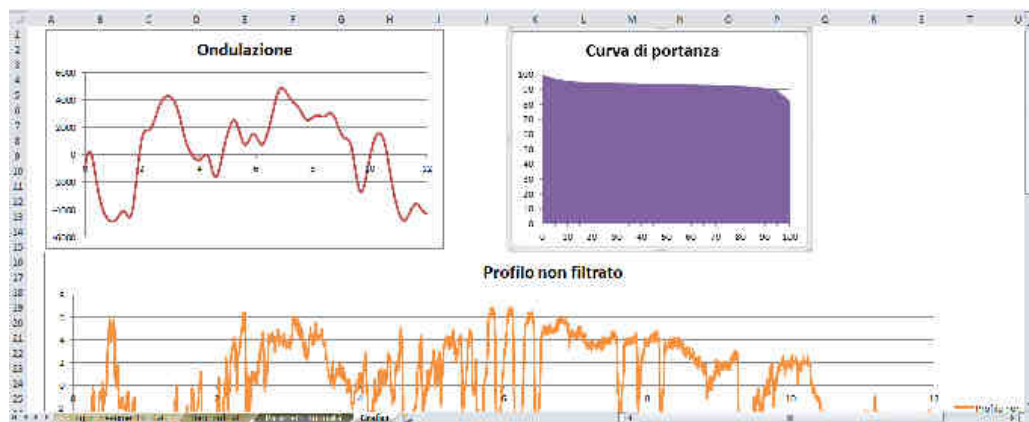


Figure 5.26: Excel sheet

The Excel sheet is a usefully instrument for analyzing the profile data; in fact while the roughness tester software isn't able to compare the roughness parameters between two different acquisition, thanks this sheet was possible to do that; another important thing is that, thanks to this sheet, is possible to compare the roughness parameters trend between all the 26 teeth of a Test Article.

## CHAPTER 6: EXPERIMENTAL RESULTS

### 6.1) INTRODUCTION

The performance increasing in torque transmission by means of splined couplings make very important to preview the materials characteristics together with the wear-limiting conditions. This chapter experimentally investigates both of these factors, by assessing the fretting performance of candidate spline materials by using specimens optimally reproducing the real component installed in an aircraft engine and subjected to the phenomenon of wear.

A number of representative fretting tests were conducted in different misalignment conditions and in presence or not of lubrication. The applied torque was the same in every tests and it reproduced the torque really applied on the component in the engine.

Results were analyzed on the basis of different experimental techniques; in particular, different roughness parameters were used to well understand the variation of the surface topography after wear test.

Finally, the Ruiz parameter ( $R_1$ ) was related to tests; to do that the analytical methods previously described are used and the results were compared with the worn surfaces of the teeth.

### 6.2) CATALOGING PHASE

Tests objectives are the following:

1. Investigation about how a spline coupling is worn;
2. Preliminary comparison of the Ruiz parameter for the wear phenomenon determination.

The inquiry method, chosen to determine the presence of wear, is mainly based on the comparison and on the measurement of parameters of the Test Article before and after tests.

In fact, the spline coupling teeth rubbing leads to a significant variation of surface parameters.

Before starting every tests, the specimens were cataloged according to the type of coupling and the type of tooth, like shown in Table 6.1:

<b>Shaft:</b>	M (male)	<b>Hub:</b>	F (female)
	B (crowning teeth)		B (crowning teeth)
	N° (test number)		N° (test number)

Table 6.1: specimen classification

For example the spline coupling MB1-FB1 is characterized by a shaft with crowned teeth and an hub with straight teeth.

In all tests the hub teeth are straight, the letter B indicate only the relative shaft to which is coupled.

The time of every test is about 5 days and is divided in:

- Assembly time of the specimen; it is shown in Figure 6.1 (it is approximately two hours);
- Duration of a test of 10M cycles (it is roughly 112 hours with a test bench speed of 1500 [rpm]).

By setting a 700 [Nm] operating torque, i.e. the one corresponding to the real operating case, the testing campaign was established as follows (like shown previously in Table 4.3):

Code tests	Torque [Nm]	Speed [rpm]	Misalignment [']	Lubrication	Number of cycles
<b>MB1</b>	700	1500	10	Yes	10M
<b>MB2</b>	700	1500	0	Yes	10M
<b>MB3</b>	700	1500	5	Yes	10M
<b>MB4</b>	700	1500	10	No	10M

Table 6.2: campaign tests

The variables of the tests have been chosen on the basis of a preliminary test phase.

The first tests, listed in Table 6.3, were:

Code tests	Torque [Nm]	Speed [rpm]	Misalignment [']	Lubrication	Number of cycles
MD1	700	1000	0	Yes	10M
MD2	700	1000	10	Yes	10M
MD3	700	1500	5	Yes	10M
MD4	700	1000	10	Yes	10M
MD5	700	1000	10	No	10M

Table 6.3: campaign tests for the splined couplings with straight teeth; for this reason the code test was changed from letter B (crowned) to D (straight)

Preliminary tests (straight teeth) allowed to understand some aspects and in particular that the rotation speed does not affect the surface damage.



Figure 6.1: Test Article mounted on the test bench; to the left there is the shaft and to the right there is the hub

### 6.3) RESULTS OF TEST 1

The first Test Article MB1 coupled with FB1 has worked for 10M cycles with a rotation speed of about 1500 [rpm], a torque of 700 [Nm] and with 10 ['] of misalignment.

This was the first test with a crowned spline coupling; for this reason it was chosen to impose the maximum misalignment value to understand how the specimen would be worn.

To identify the teeth before and after the test; it was chosen to mark the first tooth and continue the numeration in clockwise direction.

In Figure 6.2 it is shown a tooth before the test starting; it may be observe only little surface scratches are due to the machining process.



Figure 6.2: Image of the 19th tooth of the specimen MB1 before test

Figure 6.3 shows the same tooth of the Figure 6.2, but after the test.

As it can be immediately seen, a wear area appears; in particular, the central part of the tooth is worn.

The wear zone has an elliptic form, with the central part more damaged with respect the boundary one.

The black zones near the boundary of the ellipse are the amalgamation of debris due to the sliding of the contact area during a complete rotation of the spline coupling.



Figure 6.3: Image of the 19th tooth of the specimen MB1 after test

### 6.3.1) MB1 Roughness parameters

As seen in Chapter 5, a lot of different (amplitude, spacing, hybrid) roughness parameters used to characterized the surface topography are available in litterature.

From all parameters previously described (Chapter 5), in accordance with [11, 85], the following parameters were chosen to evaluate the changing of surface after the test:

- eleven amplitude parameters:  $R_a$ ,  $R_q$ ,  $R_z(ISO)$ ,  $R_t$ ,  $R_{tm}$ ,  $R_y$ ,  $R_v$ ,  $R_p$ ,  $R_{pm}$ ,  $R_{sk}$  and  $R_{ku}$ ;
- one spacing parameter:  $P_c$ ;

- one hybrid parameter:  $\Delta a$ .

To well understand the trend of the parameters on all 26 teeth, for each Test Article it has been chosen to represent them on a polar graph; in the graphs the quadrant is divided into 26 parts (corresponding to the number of teeth) and on the circle radius is represented the value of the single parameter.

In all polar graph are represented the trend of the parameter values before (blue line) and after (red line) the test; in this way, it is simple to understand how the parameters may vary according to the test type.

Figures 6.4 - 6.12 show the trend of some chosen parameters (more representative) for the specimen MB1.

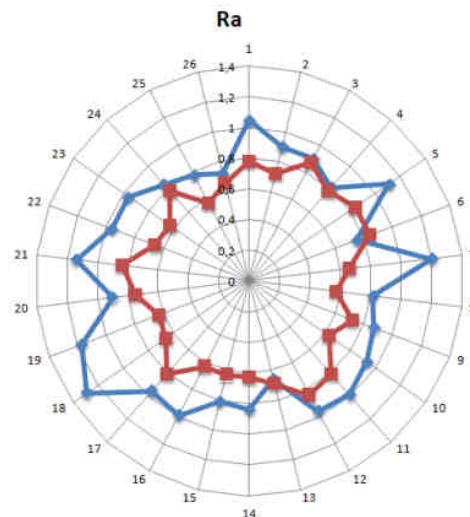


Figure 6.4: trend of the Arithmetic average height ( $R_a$ ) for MB1

Parameter  $R_a$  is defined as the average absolute deviation of the roughness irregularities from the mean line over one sampling length; the fact that diminishes after the test means that the height of the peaks and the deep of the valley have been reduced.

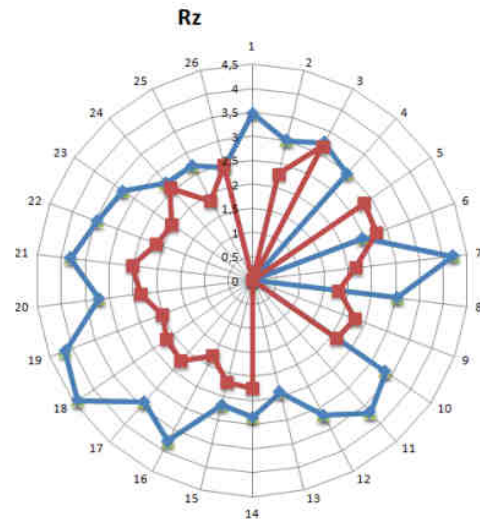


Figure 6.5: trend of the Ten-point height ( $R_{z(ISO)}$ ) for MB1

Parameter  $R_{z(ISO)}$  is defined by the International ISO system as the difference in height between the average of the five highest peaks and the five lowest valleys along the assessment length of the profile; the fact that diminishes after the test means that the five highest peaks and the five lowest valleys have reduced their amplitude.

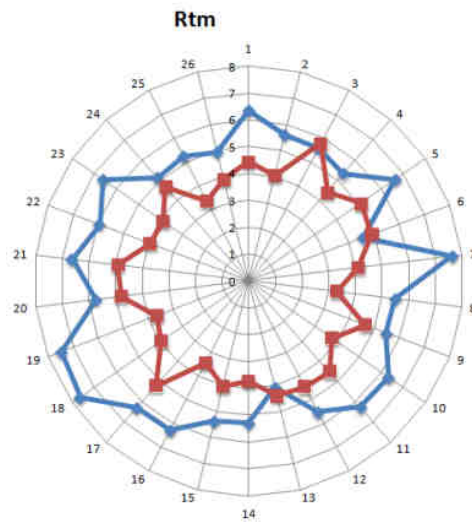


Figure 6.6: trend of the Mean of maximum peak to valley height ( $R_{tm}$ ) for MB1

Parameter  $R_{tm}$  is defined as the mean of all maximum peak to valley heights obtained within the assessment length of the profile; the fact that diminishes

after the test means that the maximum range from the peaks and the valleys has been reduced.

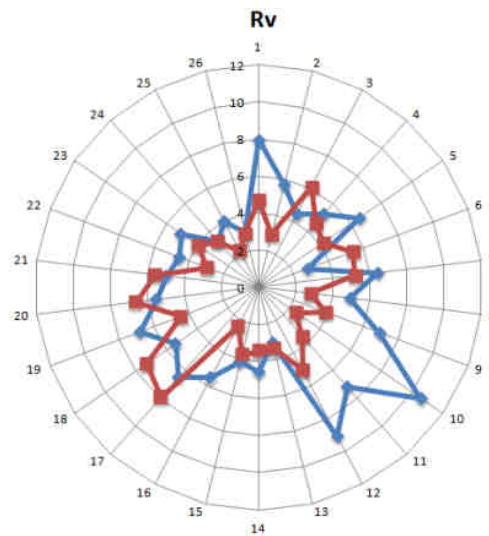


Figure 6.7: trend of the Maximum depth of valleys ( $R_v$ ) for MB1

Parameter  $R_v$  is defined as the maximum depth of the profile below the mean line within the assessment length; the fact that diminishes after the test means that the deep valleys has reduced their amplitude.

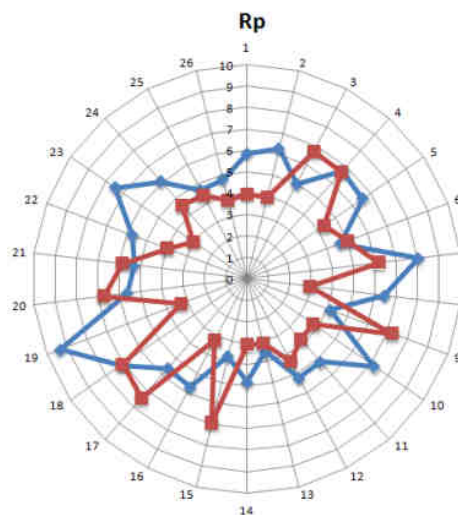


Figure 6.8: trend of the Maximum height of peaks ( $R_p$ ) for MB1

Parameter  $R_p$  is defined as the maximum height of the profile above the mean line within the assessment length; the fact that diminishes after the test means that the height of the peaks has been reduced.

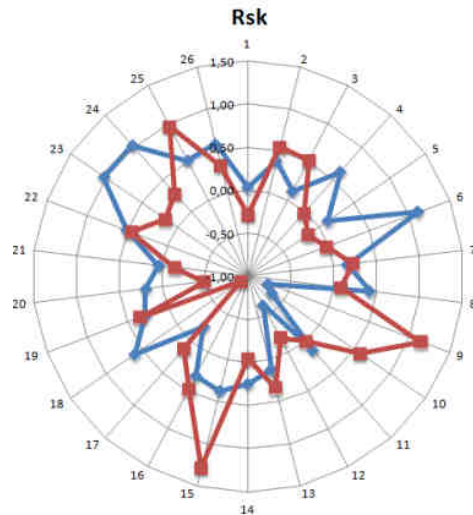


Figure 6.9: trend of the Skewness ( $R_{sk}$ ) for MB1

Parameter  $R_{sk}$  is sensitive to occasional deep valleys or high peaks; the fact that diminishes after the test means that a symmetrical distribution of peaks and valleys is obtaining.

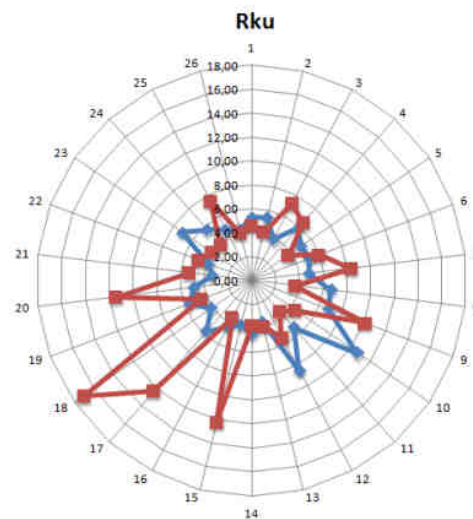


Figure 6.10: trend of the Kurtosis ( $R_{ku}$ ) for MB1

Parameter  $R_{ku}$  describes the sharpness of the probability density of the profile; the fact that diminishes after the test means that the trend of the profile roughness has less high peaks and less deep valley.

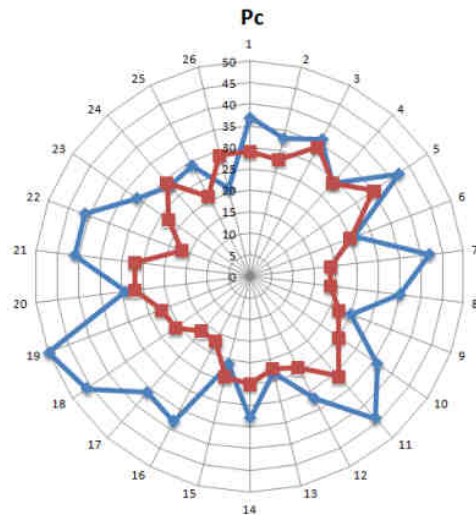


Figure 6.11: trend of the Peak count ( $P_c$ ) for MB1

Parameter  $P_c$  is determined along the assessment length and the result is given in peaks per centimeter; the fact that diminishes after the test means that the number of peaks for centimeter diminishes.

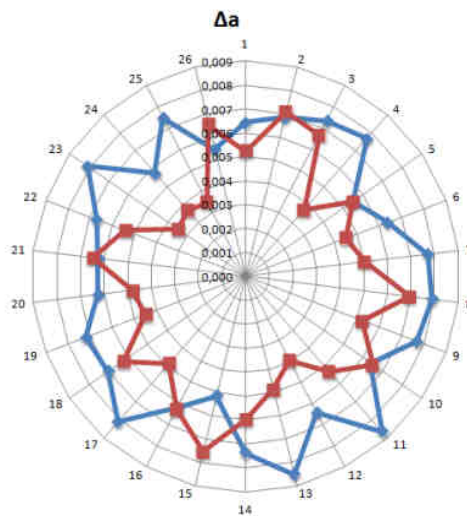


Figure 6.12: trend of the Mean slope of the profile ( $\Delta_a$ ) for MB1

Parameter  $\Delta_a$  is defined as the mean absolute profile slope over the assessment length; the fact that the slope of the profile decreases after the test means that there are many peaks with a less slope; how if a grinding phenomenon has been done.

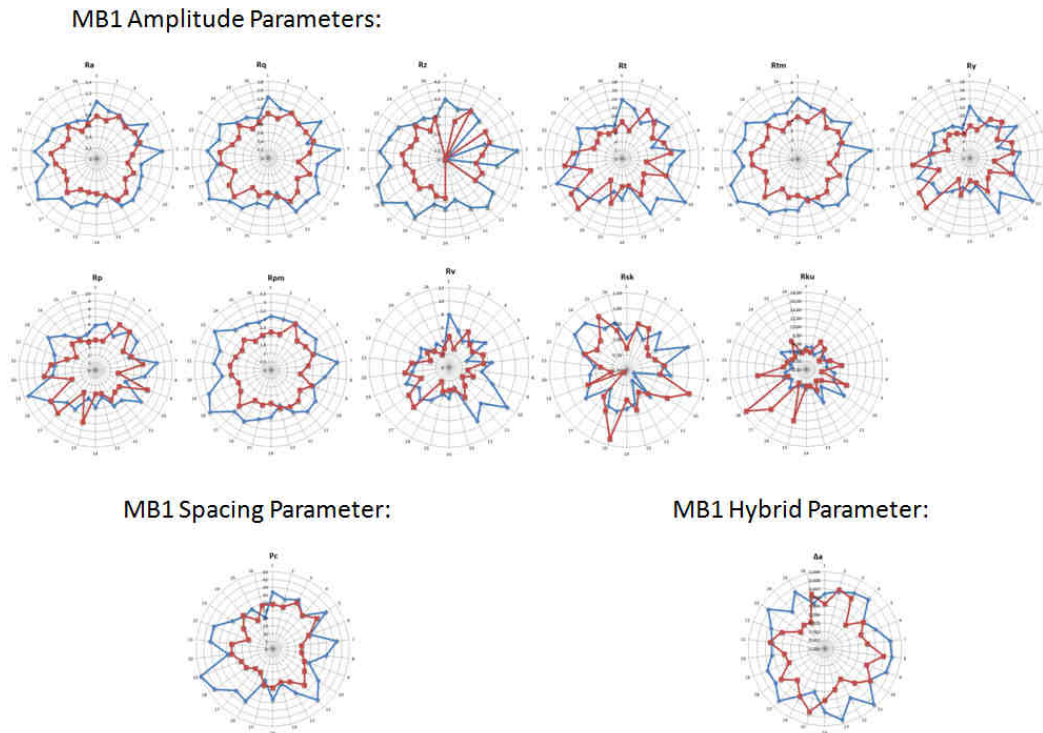


Figure 6.13: Roughness parameters summarized for MB1 test; (blue line is referred to before the test, and red line is referred to after the test)

Figure 6.13 summarizes the results related to all parameters. From the analysis of this Figure, it may be pointed out that all the roughness amplitude parameters decrease after the test (red line); this is due to the fact that, caused by the wear phenomenon, both peaks and valleys show a decreasing amplitude.

By the same way, the roughness spacing parameter decreases, because, like the amplitude, the number of peaks for centimeter diminishes (Figure 6.13).

By observing the hybrid parameter, it can be also seen how the slope of the profile decreases (Figure 6.13).

To well understand how the roughness parameters change after a test, two different graphs have been draft; the first represents the mean (respect the 26 teeth) variation on the parameter value before and after the test (Figure 6.14) and the second graph representing the area variation of the polar graphs (see previously) before and after the test (Figure 6.15).

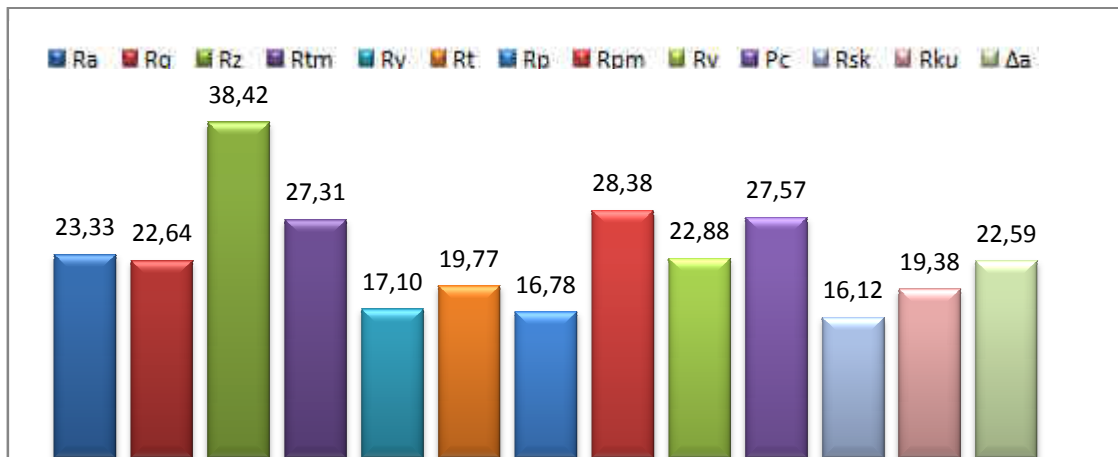


Figure 6.14: Difference percentage of mean roughness parameters values for MB1

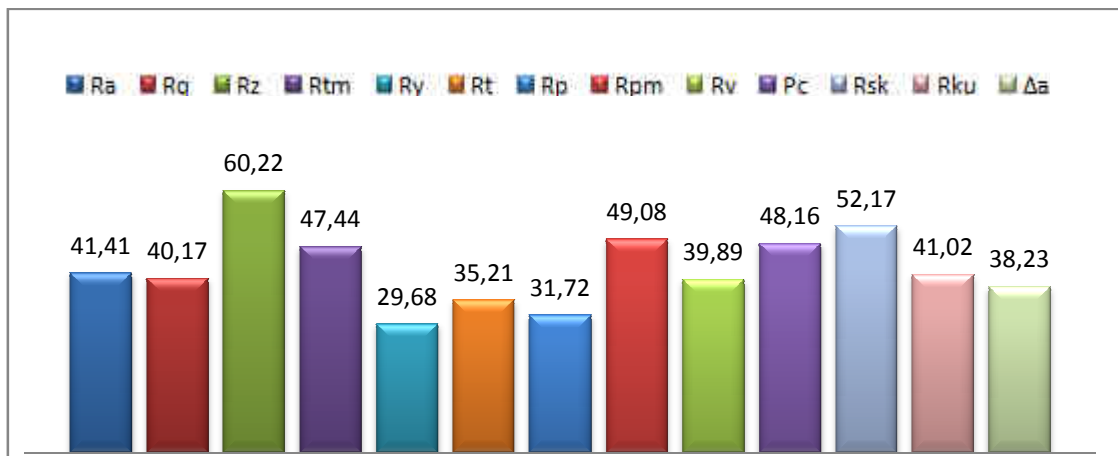


Figure 6.15: Difference percentage of polar graphs area values for MB1

As it can be observed from Figure 6.14, the decreasing order of percentage difference of mean values is:  $R_z$  (38.42%),  $R_{pm}$  (28.38%),  $P_c$  (27.57%),  $R_{tm}$  (27.31%),  $R_a$  (23.33%),  $R_v$  (22.88%),  $R_q$  (22.64%),  $\Delta a$  (22.59%),  $R_t$  (19.77%),  $R_{ku}$  (19.38%),  $R_y$  (17.1%),  $R_p$  (16.78%) and  $R_{sk}$  (16.12%).

For Figure 6.15, the decreasing order of percentage difference of polar graphs area values is:  $R_z$  (60.22%),  $R_{sk}$  (52.17%),  $R_{pm}$  (49.08%),  $P_c$  (48.16%),  $R_{tm}$  (47.44%),  $R_a$  (41.41%),  $R_{ku}$  (41.02%),  $R_q$  (40.17%),  $R_v$  (39.89%),  $\Delta a$  (38.23%),  $R_t$  (35.21%),  $R_p$  (31.72%) and  $R_y$  (29.68%).

### 6.3.2) Ruiz model for MB1 test

To compare the Ruiz analytical model previously described, it is used a dedicated program realized during my PhD activity.

To calculate the Ruiz parameter trend it is necessary to set up it by means of the geometric characteristic of the splined coupling (number of teeth, modulus, pitch diameter, major curvature of the shaft and of the hub), with the applied torque (700 [Nm]), the misalignment imposed (10 [°]) and a profile error (order of hundredth millimeters).

The program returns the following results: contact area, sliding of the contact area (Figure 6.16), pressure trend [MPa] (Figure 6.17) and Ruiz parameter trend (Figure 6.18).

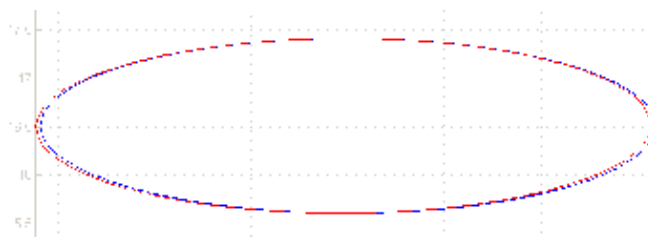


Figure 6.16: Representation of the area sliding with 10 [°] of misalignment, in blue the area without misalignment and in red the area with misalignment

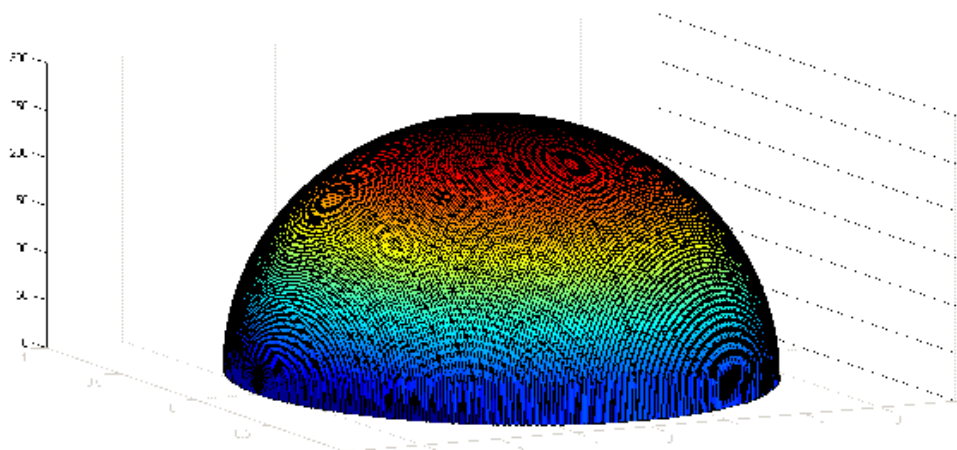


Figure 6.17: Pressure trend when it is applied 700 [Nm] torque

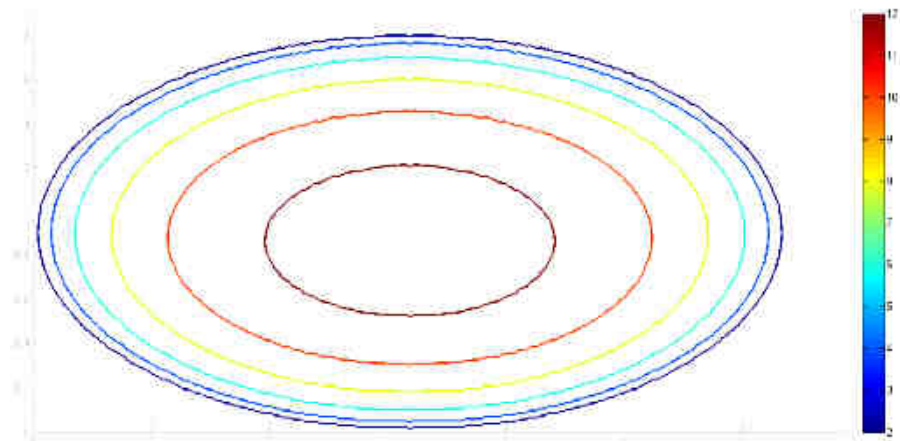


Figure 6.18: Ruiz parameter trend for the test MB1

It has been chosen to compare the Ruiz parameter trend with an image of the MB1 specimen tooth; in Figure 6.19 the overlap is shown.

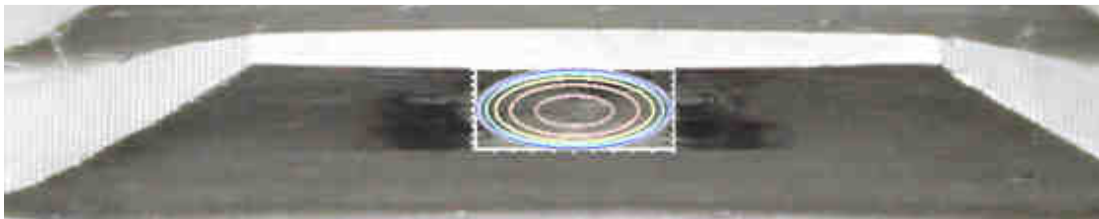


Figure 6.19: overlapping between Ruiz parameter and an image of a MB1 tooth

As it can be seen, there is a very good correlation between analytical and experimental results; in particular, the wear area is similar and the Ruiz parameter trend corresponds to the experimental test data; in fact, the higher value of the parameter is in the center of the ellipse, where the wear phenomenon is more present; the lower value of the parameter is in the boundary zone, where the wear phenomenon is less presents.

#### 6.4) RESULTS OF TEST 2

The second Test Article MB2 coupled with FB2 has worked for 10M cycles with a rotation speed of about 1500 [rpm], a torque of 700 [Nm] and without misalignment.

This was the second test with a crowned spline coupling; for this reason it was chosen to impose the minimum misalignment value (0 [']) to understand how the specimen would be worn when the hub is theoretically perfect aligned with the shaft.

To identify the teeth before and after the test it was chosen to mark the first tooth and continue the numeration in clockwise direction.

In Figure 6.20 it is shown a tooth before the test starting, as can be seen there isn't wear signs the only little surface scratches are due to the machining process.



Figure 6.20: Image of the 22th tooth of the specimen MB2 before test

In Figure 6.21 shows the same tooth of the Figure 6.20, but after the test.

There is maybe a little worn zone in the center of the face width and on the tooth head.



Figure 6.21: Image of the 22th tooth of the specimen MB2 after test

##### 6.4.1) MB2 Roughness parameters

Like the previous test (MB1) in Figure 6.22 - 6.30 are shown the trend of the roughness parameters.

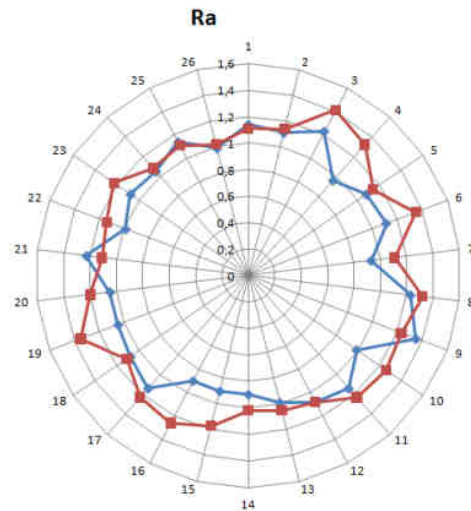


Figure 6.22: trend of the Arithmetic average height ( $R_a$ ) for MB2

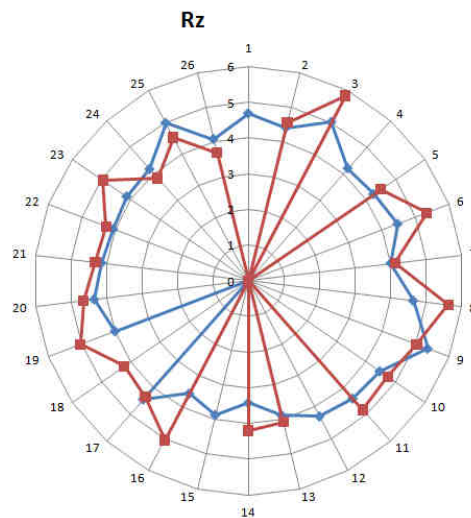


Figure 6.23: trend of the Ten-point height ( $R_{z(ISO)}$ ) for MB2

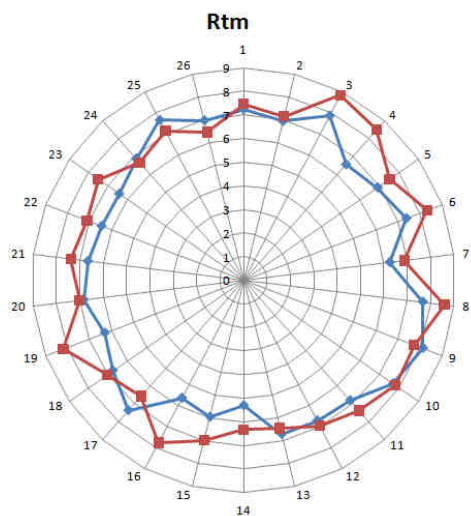


Figure 6.24: trend of the Mean of maximum peak to valley height ( $R_{tm}$ ) for MB2

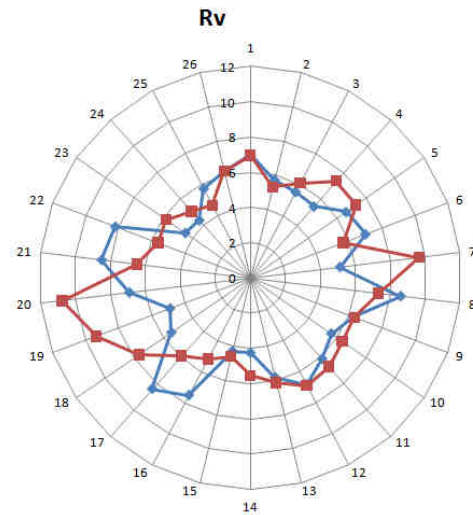


Figure 6.25: trend of the Maximum depth of valleys ( $R_v$ ) for MB2

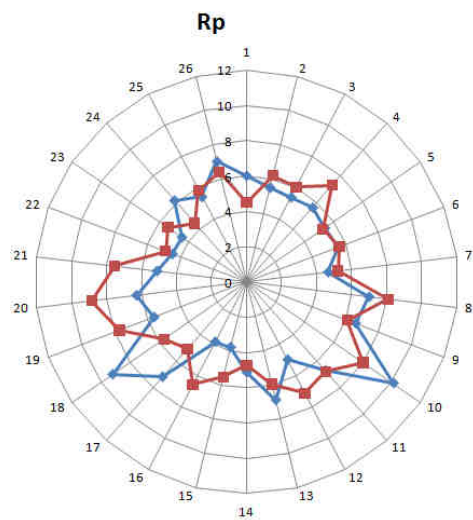


Figure 6.26: trend of the Maximum height of peaks ( $R_p$ ) for MB2

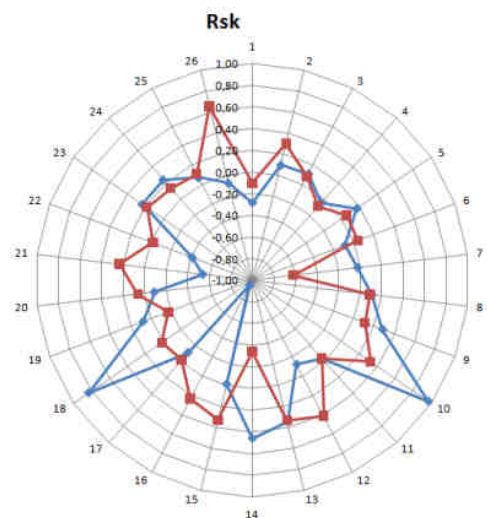


Figure 6.27: trend of the Skewness ( $R_{sk}$ ) for MB2

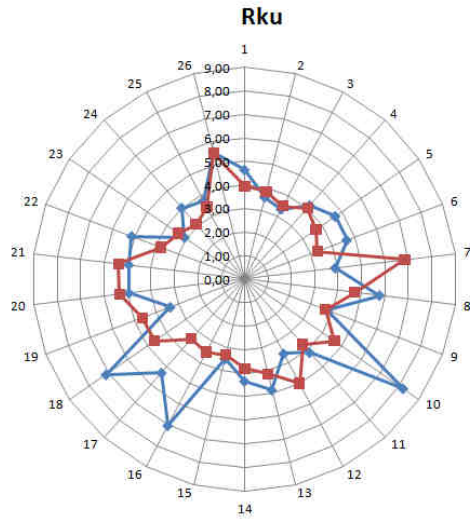


Figure 6.28: trend of the Kurtosis ( $R_{ku}$ ) for MB2

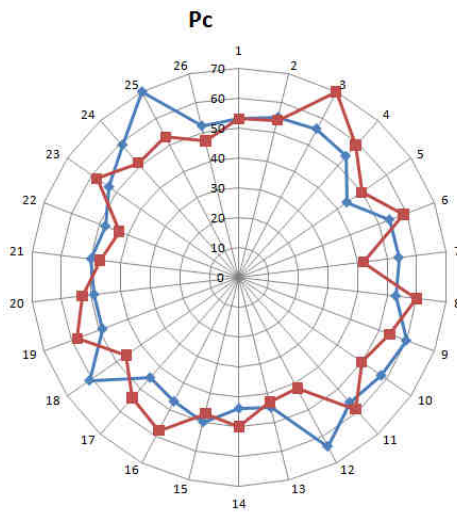


Figure 6.29: trend of the Peak count ( $P_c$ ) for MB2

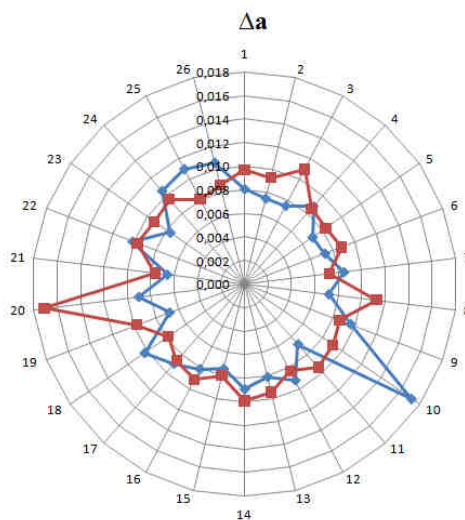


Figure 6.30: trend of the Mean slope of the profile ( $\Delta_a$ ) for MB2

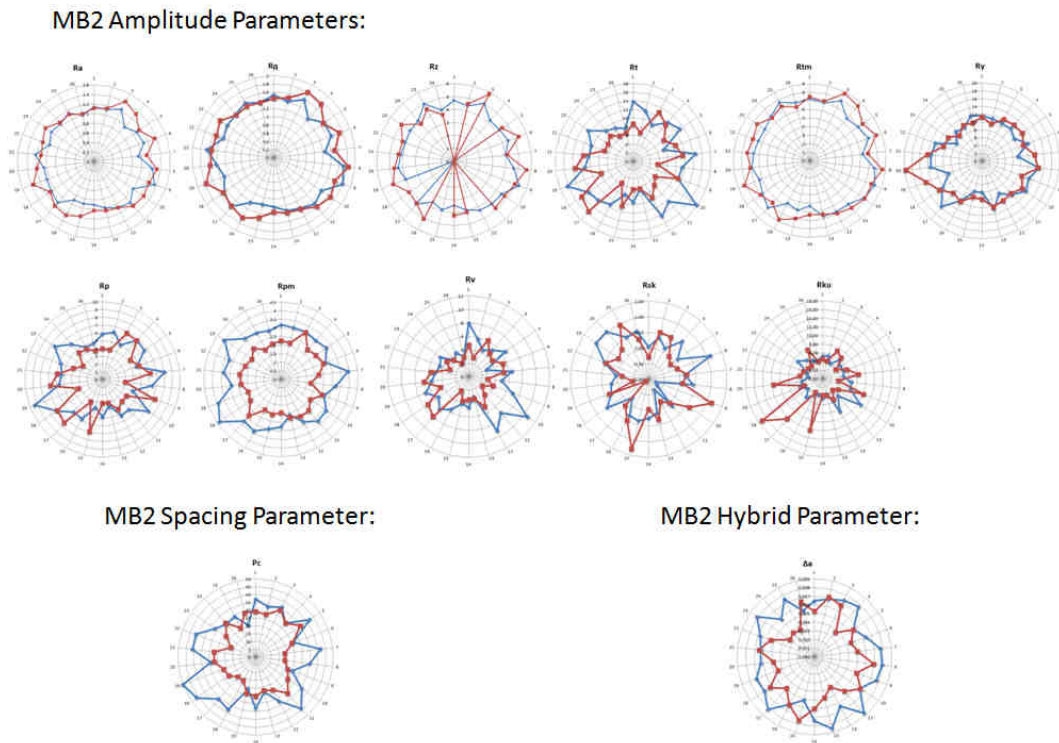


Figure 6.31: Roughness parameters summarized for MB2 test; (blue line is referred to before the test, and red line is referred to after the test)

As can be seen from the Figure 6.31 all the roughness amplitude parameters after the test (red line) are the same respect the parameters before the test (blue line); this is most likely due to the fact that there isn't a meaningful wear phenomenon.

At the same time, the roughness spacing parameter are also the same, like the amplitude ones (Figure 6.31).

By observing the hybrid parameter, it can be also see how the slope of the profile is substantially equal (Figure 6.31).

Also for the specimen MB2, Figure 6.32 and 6.33 show respectively the difference percentage of mean roughness parameters values and the difference percentage of polar graphs area values.

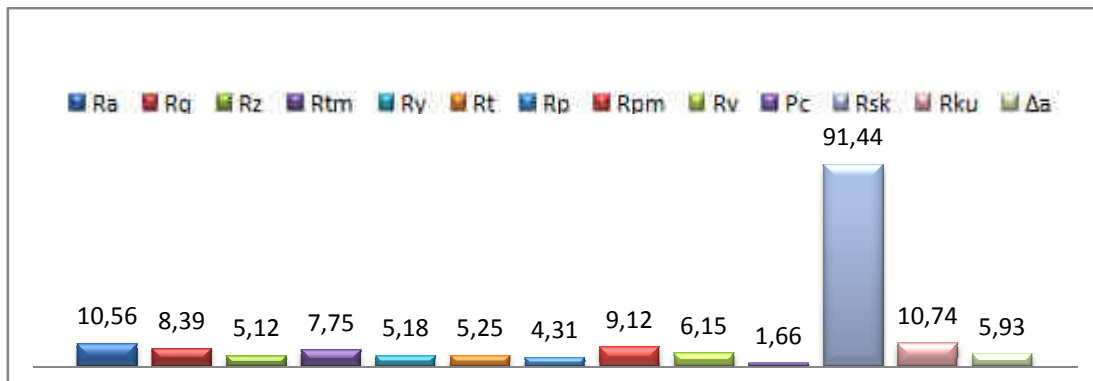


Figure 6.32: Difference percentage of mean roughness parameters values for MB2

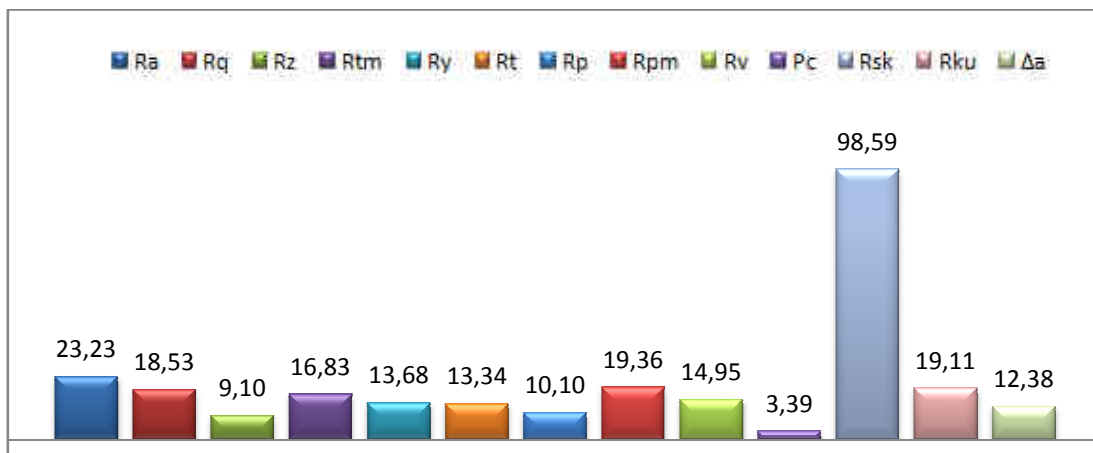


Figure 6.33: Difference percentage of polar graphs area values for MB2

As it can be seen from Figure 6.32, the decreasing order of difference percentage of mean values is:  $R_{sk}$  (91.44%),  $R_{ku}$  (10.74%),  $R_a$  (10.56%),  $R_{pm}$  (9.12%),  $R_q$  (8.39%),  $R_{tm}$  (7.75%),  $R_v$  (6.15%),  $\Delta a$  (5.93%),  $R_t$  (5.25%),  $R_y$  (5.18%),  $R_z$  (5.12%),  $R_p$  (4.31%) and  $P_c$  (1.06%).

Figure 6.33 shows the decreasing order of difference percentage of polar graphs area values is:  $R_{sk}$  (98.49%),  $R_a$  (23.23%),  $R_{ku}$  (19.11%),  $R_{pm}$  (19.36%),  $R_q$  (18.53%),  $R_{tm}$  (16.83%),  $R_v$  (14.95%),  $R_y$  (13.68%),  $R_t$  (13.34%),  $\Delta a$  (12.38%),  $R_p$  (10.1%),  $R_z$  (9.1%) and  $P_c$  (3.39%).

#### 6.4.2) Ruiz model for MB2 test

For this test is impossible to compare the analytical model and the experimental results because the Ruiz parameter is a multiplication between the surface shear traction and the relative slip amplitude that with 0 [°] of misalignment angle is equal to zero.

#### 6.5) RESULTS OF TEST 3

The third Test Article MB3 coupled with FB3 has worked for 10M cycles with a rotation speed of about 1500 [rpm], a torque of 700 [Nm] and with 5 [°] of misalignment.

This was the third test and for this reason it was chosen to impose a middle misalignment value respect the previously tests (MB1 and MB2) to understand how the specimen would be worn.

In Figure 6.34 it is shown a tooth before the test starting.



Figure 6.34: Image of the 23th tooth of the specimen MB3 before test

Figure 6.35 shows the same tooth of the Figure 6.34, but after the test.

As it can be immediately seen, wear area appears; in particular, the upper part of the tooth is worn; this is probably due to a profile error causing the translation of the contact area on the upper part of the face width.

The wear zone has an elliptic form, with the central part more damaged than the boundary part.

The black zones near the boundary of ellipse are the amalgamation of debris due to the sliding of the contact area during a complete rotation of the spline coupling.



Figure 6.35: Image of the 23th tooth of the specimen MB3 after test

### 6.5.1) MB3 Roughness parameters

Like the previous tests (MB1, MB2) in Figures 6.36 - 6.44 are shown the trend of some parameters for the specimen MB3; after these Figure is shown the trend of all the parameters analyzed .

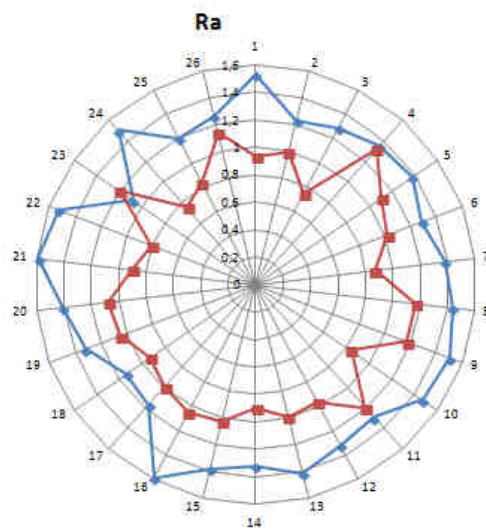


Figure 6.36: trend of the Arithmetic average height ( $R_a$ ) for MB3

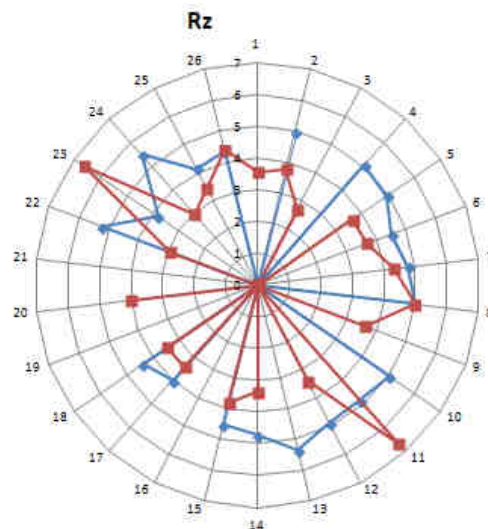


Figure 6.37: trend of the Ten-point height ( $R_{z(ISO)}$ ) for MB3

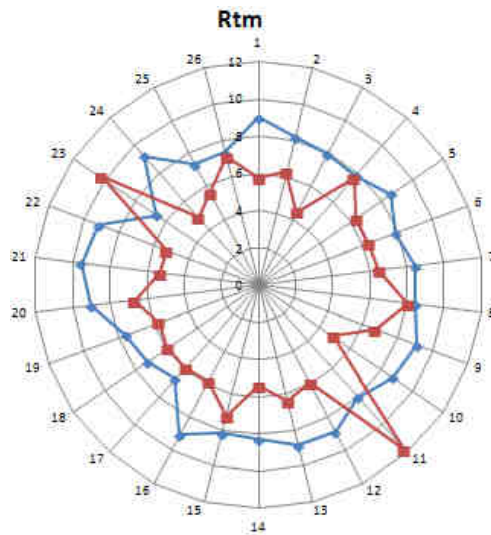


Figure 6.38: trend of the Mean of maximum peak to valley height ( $R_m$ ) for MB3

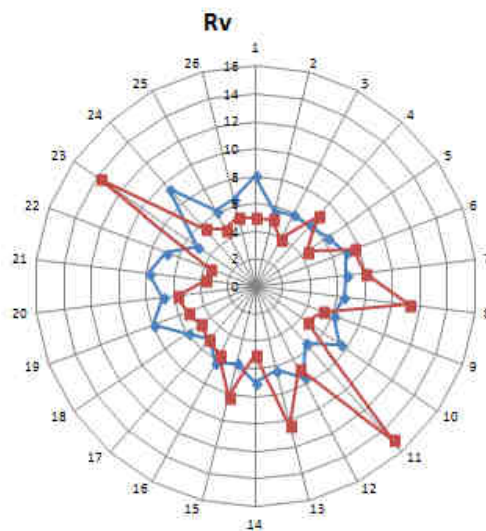


Figure 6.39: trend of the Maximum depth of valleys ( $R_v$ ) for MB3

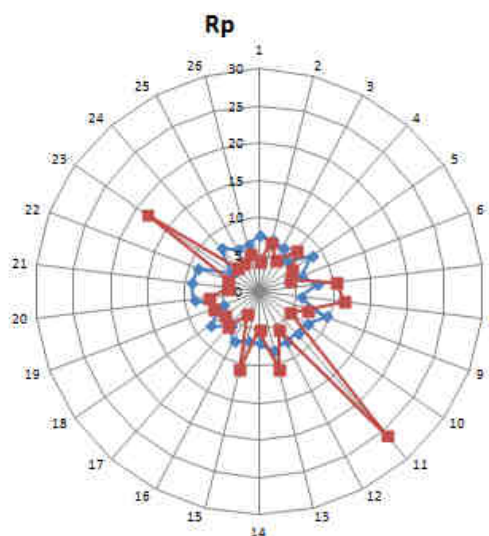


Figure 6.40: trend of the Maximum height of peaks ( $R_p$ ) for MB3

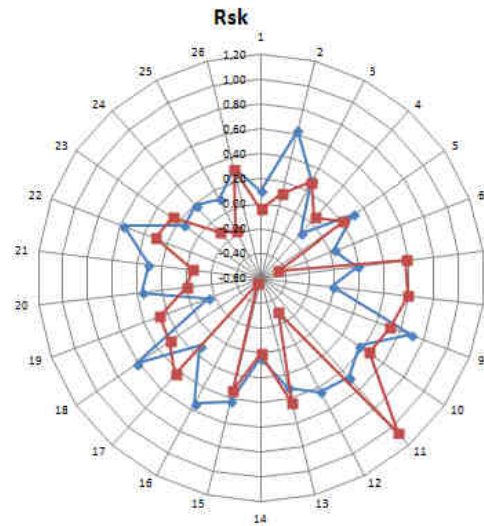


Figure 6.41: trend of the Skewness ( $R_{sk}$ ) for MB3

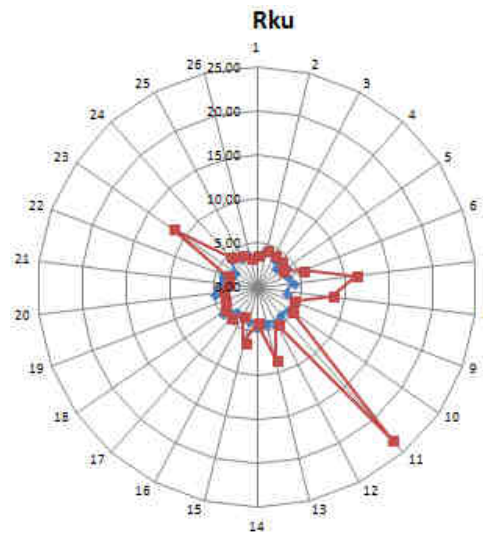


Figure 6.42: trend of the Kurtosis ( $R_{ku}$ ) for MB3

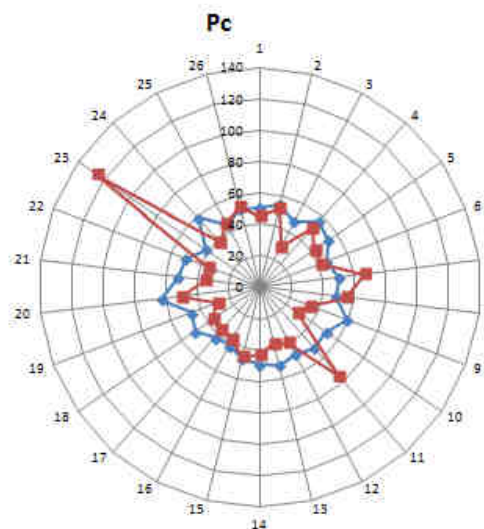


Figure 6.43: trend of the Peak count ( $P_c$ ) for MB3

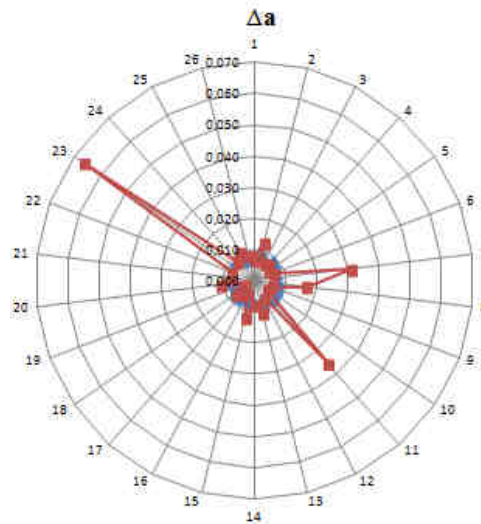
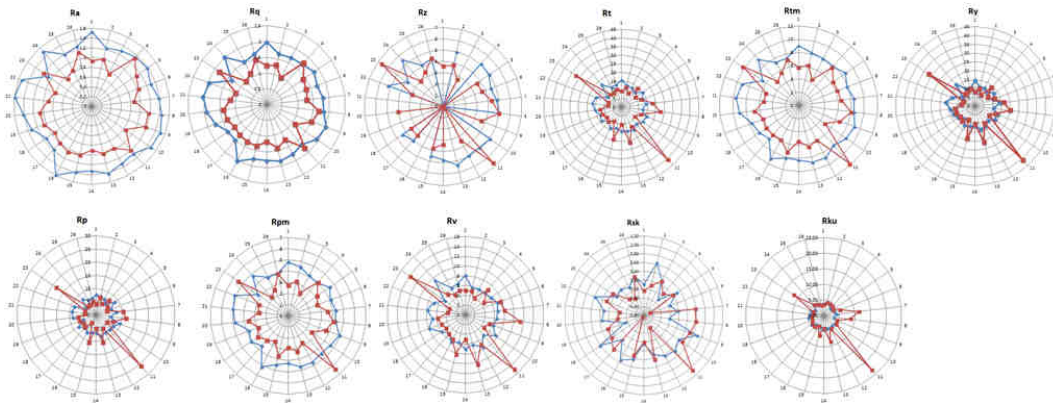
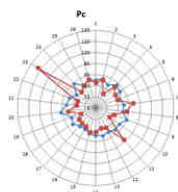


Figure 6.44: trend of the Mean slope of the profile ( $\Delta a$ ) for MB3

MB3 Amplitude Parameters:



MB3 Spacing Parameter:



MB3 Hybrid Parameter:

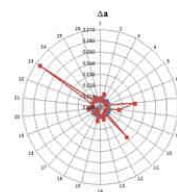


Figure 6.45: Roughness parameters summarized for MB3 test; (blue line is referred to before the test, and red line is referred to after the test)

Figure 6.45 shows that all the roughness amplitude parameters after the test (red line) decrease; this is most likely due to the wear phenomenon: both peaks and valleys present an amplitude decreasing.

At the same time, the roughness spacing parameter decreases; the number of peaks for centimeter diminish (Figure 6.45).

By observing the hybrid parameter it can be also seen how the slope of the profile decreases (Figure 6.45).

Figure 6.46 and 6.47 show respectively the difference percentage of mean roughness parameters values and the difference percentage of polar graphs area values.

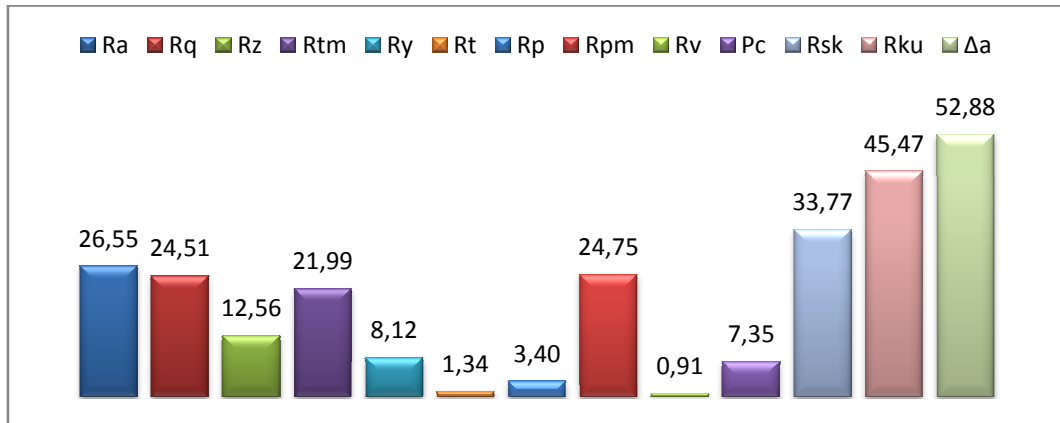


Figure 6.46: Difference percentage of mean roughness parameters values for MB3

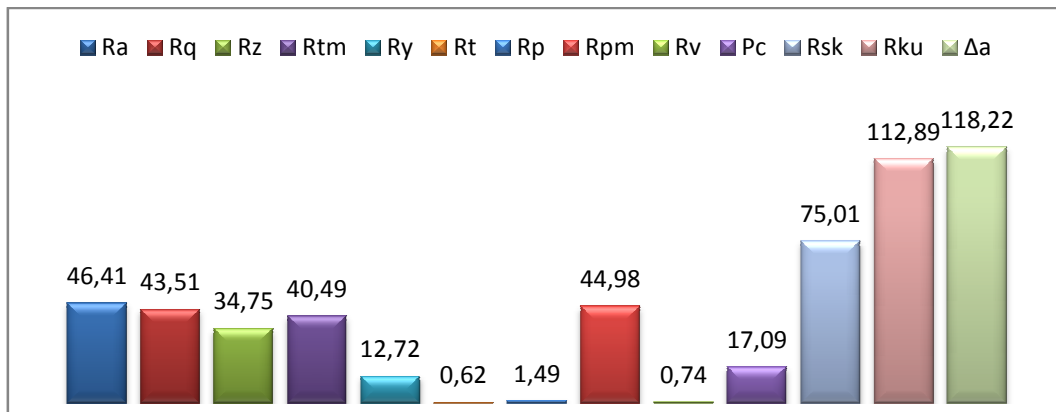


Figure 6.47: Difference percentage of polar graphs area values for MB3

As can be seen from Figure 6.46 the decreasing order of difference percentage of mean values is:  $\Delta a$  (52.88%),  $R_{ku}$  (45.47%),  $R_{sk}$  (33.77%),  $R_a$  (26.55%),  $R_{pm}$  (24.75%),  $R_q$  (24.51%),  $R_{tm}$  (21.99%),  $R_z$  (8.12%),  $R_y$  (8.12%),  $P_c$  (7.35%),  $R_p$  (3.4%),  $R_t$  (1.34%) and  $R_v$  (0.91%).

Figure 6.47 shows the decreasing order of difference percentage of polar graphs area values is:  $\Delta a$  (118.22%),  $R_{ku}$  (112.89%),  $R_{sk}$  (75.01%),  $R_a$  (46.41%),  $R_{pm}$  (44.98%),  $R_q$  (43.51%),  $R_{tm}$  (40.49%),  $R_z$  (34.75%),  $P_c$  (17.09%),  $R_y$  (12.72%),  $R_p$  (1.49%),  $R_v$  (0.74%) and  $R_t$  (0.62%).

### 6.5.2) Ruiz model for MB3 test

To calculate the Ruiz parameter trend it is set up with the geometric characteristic of the splined coupling (number of teeth, modulus, pitch diameter, major curvature of the shaft and of the hub), with the applied torque (700 [Nm]), with the misalignment imposed (5 [°]) and with a profile error (order of hundredth millimeters).

The program returns the following results: contact area, sliding of the contact area (Figure 6.48), pressure trend [MPa] (Figure 6.49) and Ruiz parameter trend (Figure 6.50).

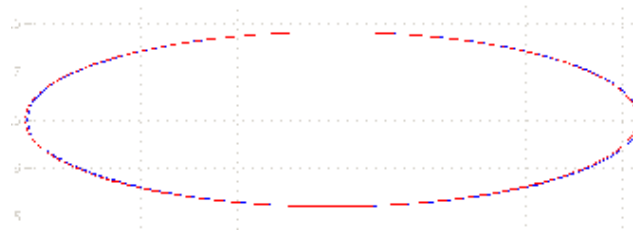


Figure 6.48: Representation of the area sliding with 5 [°] of misalignment, in blue the area without misalignment and in red the area with misalignment

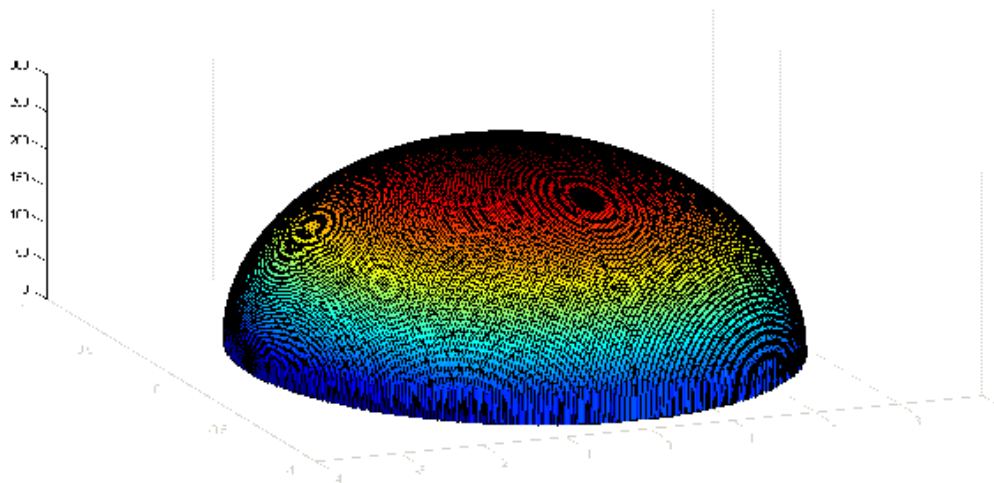


Figure 6.49: Pressure trend when it is applied 700 [Nm] torque

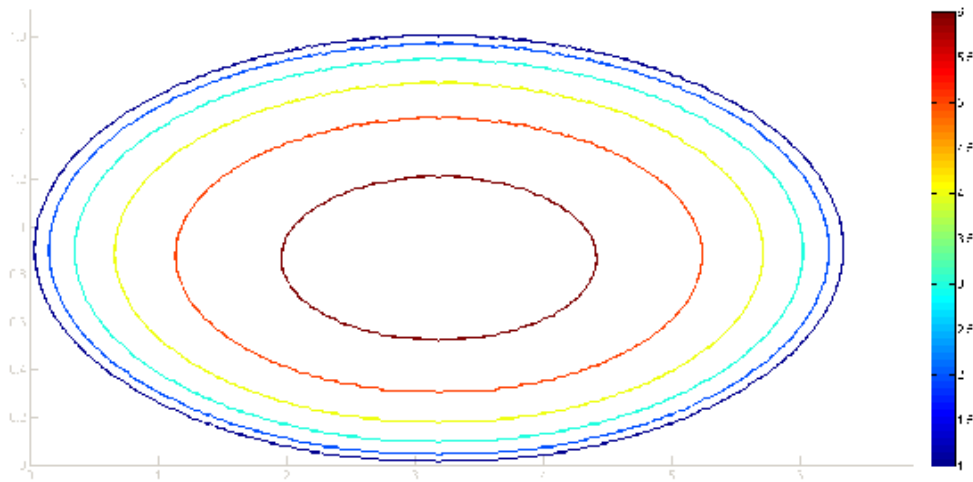


Figure 6.50: Ruiz parameter trend for the test MB3

It has been chosen to compare the Ruiz parameter trend with an image of the MB3 specimen tooth; in Figure 6.51 there is shown the overlap.

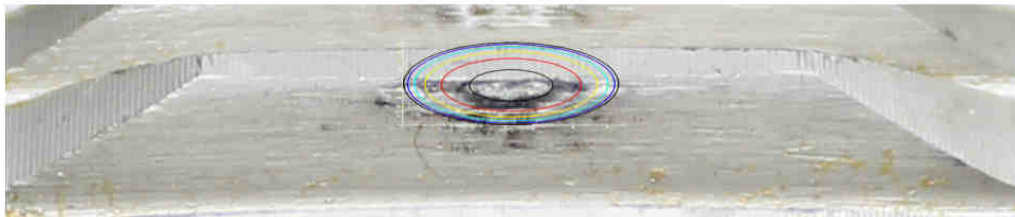


Figure 6.51: overlapping between Ruiz parameter and an image of a MB3 tooth

As it can be seen, there is a very good correlation between analytical and experimental results; in particular the wear area is similar and Ruiz parameter trend corresponds to the experimental test data.

There is only a translation of the effective contact area, that (as seen previously) it is due to a manufacture error.

## 6.6) RESULTS OF TEST 4

The last Test Article MB4 coupled with FB4 has worked for 10M cycles with a rotation speed of about 1500 [rpm], a torque of 700 [Nm], with 10 ['] of misalignment and without lubrication.

It is decided to disable the lubrication to obtain the worst operating condition.

In Figure 6.52 it is shown a tooth before the test starting.



Figure 6.52: Image of the 16th tooth of the specimen MB4 before test

Figure 6.53 shows the same tooth of the Figure 6.52, but after the test.

As it can be immediately seen, there is wear area (the largest of all the tests carried out); in particular the tooth is worn from the pith diameter to the upper part; this is probably due to a profile error that has caused the translation of the contact area on the upper part of the face width.

The wear zone has an elliptic form, despite the adverse conditions (absence of lubrication and profile error), with the central part more damaged than the boundary part.

The red zones near the ellipse boundary are the oxidation phenomena that are created due to the absence of oil.



Figure 6.53: Image of the 22th tooth of the specimen MB2 after test

### 6.6.1) MB4 Roughness parameters

Like the previous tests (MB1-MB2-MB3) in Figure 6.54 - 6.62 are shown the trend of the roughness parameters.

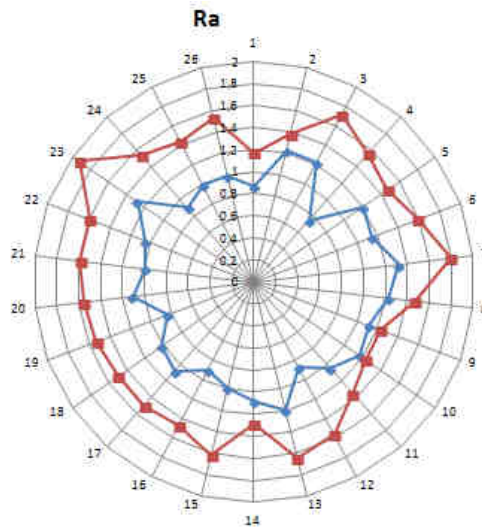


Figure 6.54: trend of the Arithmetic average height ( $R_a$ ) for MB4

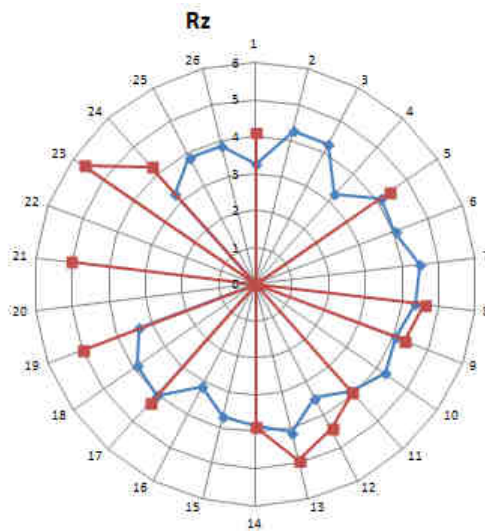


Figure 6.55: trend of the Ten-point height ( $R_{z(ISO)}$ ) for MB4

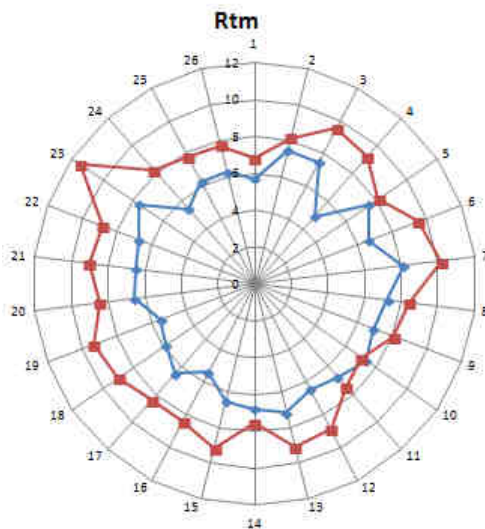


Figure 6.56: trend of the Mean of maximum peak to valley height ( $R_{tm}$ ) for MB4

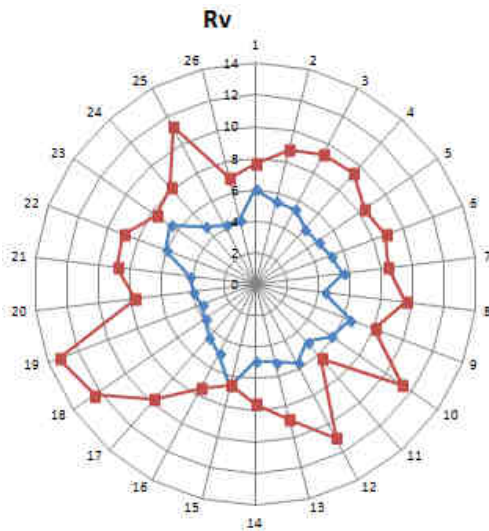


Figure 6.57: trend of the Maximum depth of valleys ( $R_v$ ) for MB4

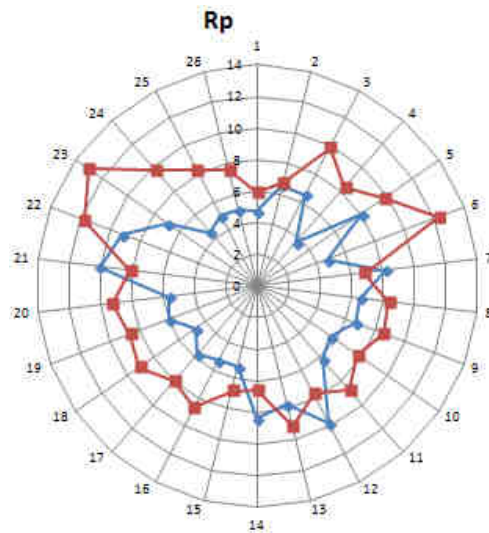


Figure 6.58: trend of the Maximum height of peaks ( $R_p$ ) for MB4

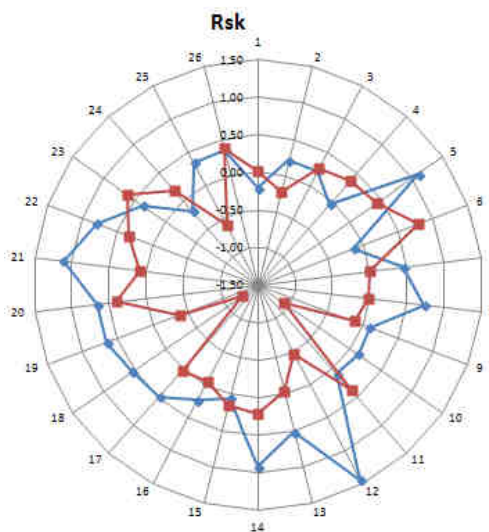


Figure 6.59: trend of the Skewness ( $R_{sk}$ ) for MB3

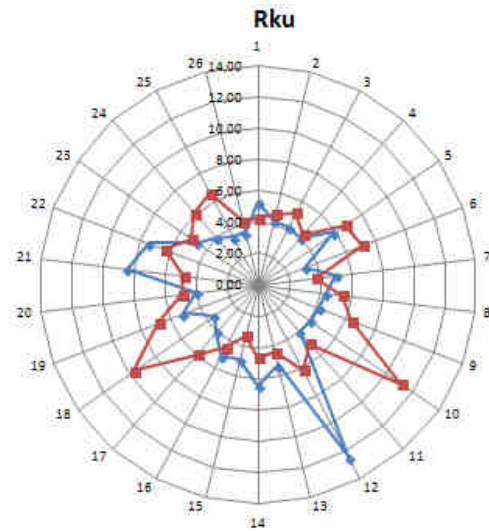


Figure 6.60: trend of the Kurtosis ( $R_{ku}$ ) for MB4

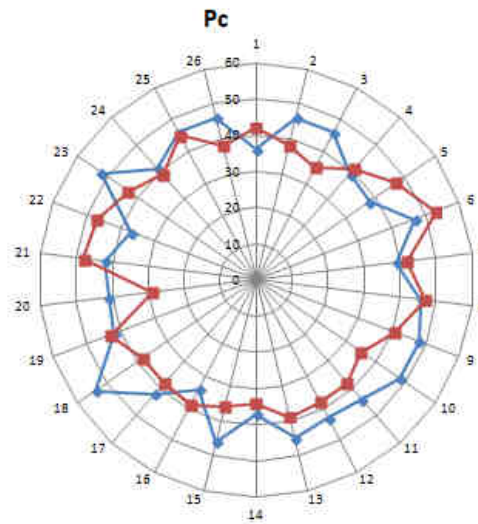


Figure 6.61: trend of the Peak count ( $P_c$ ) for MB4

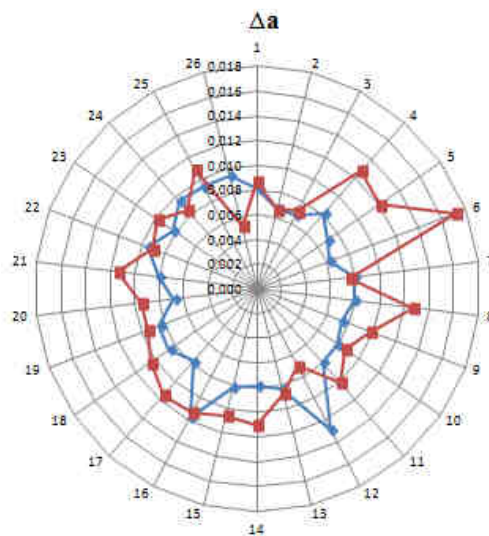


Figure 6.62: trend of the Mean slope of the profile ( $\Delta_a$ ) for MB4

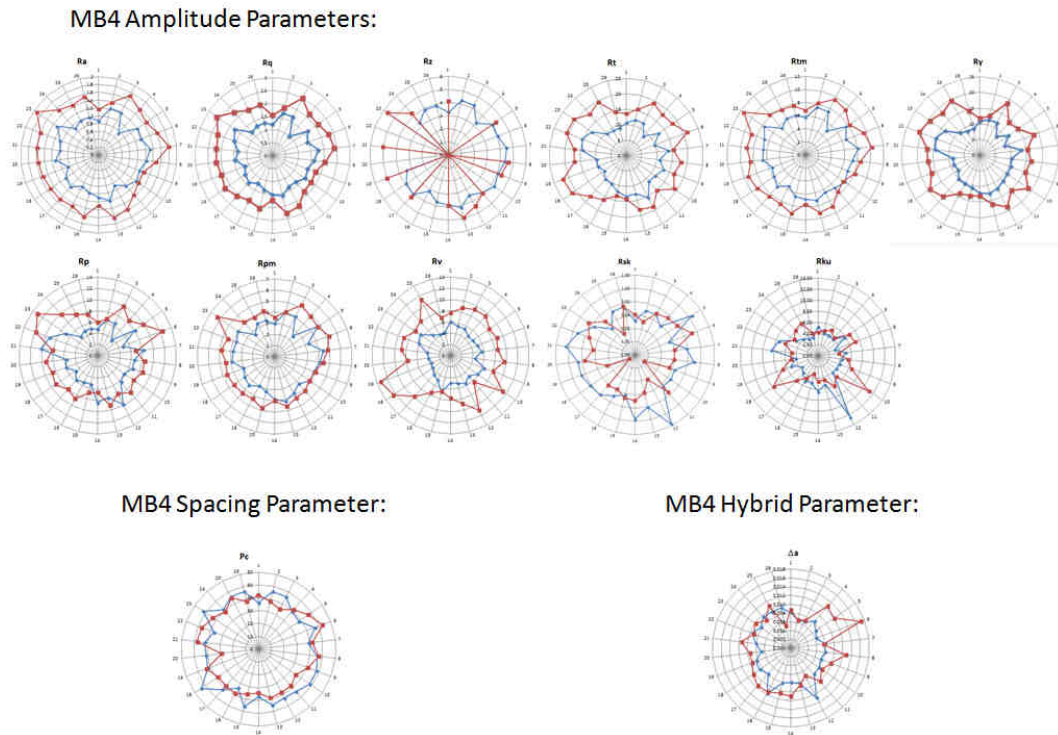


Figure 6.63: Roughness parameters summarized for MB4 test; (blue line is referred to before the test, and red line is referred to after the test)

As can be seen from Figure 6.63 all the roughness amplitude parameters increase after the test (red line); this is due to the fact that, caused by to wear phenomenon, both peaks and valleys show a increasing amplitude; this phenomena is accentuated by the absence of oil.

By the same time, the roughness spacing parameter increases, because, like the amplitude, the number of peaks for centimeter increases (Figure 6.63).

By observing the hybrid parameter, it can be also seen how the slope of the profile increases (Figure 6.63).

Figure 6.64 and 6.65 show respectively the difference percentage of mean roughness parameters values and the difference percentage of polar graphs area values.

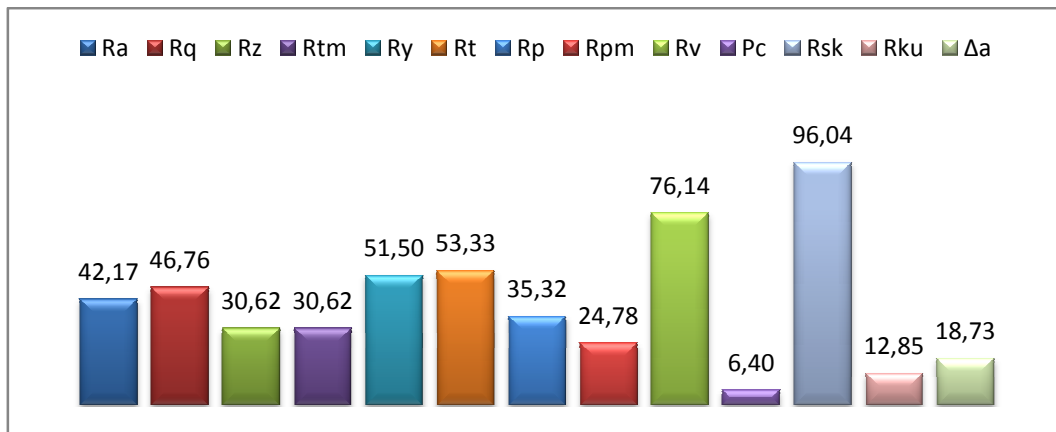


Figure 6.64: Difference percentage of mean roughness parameters values for MB4

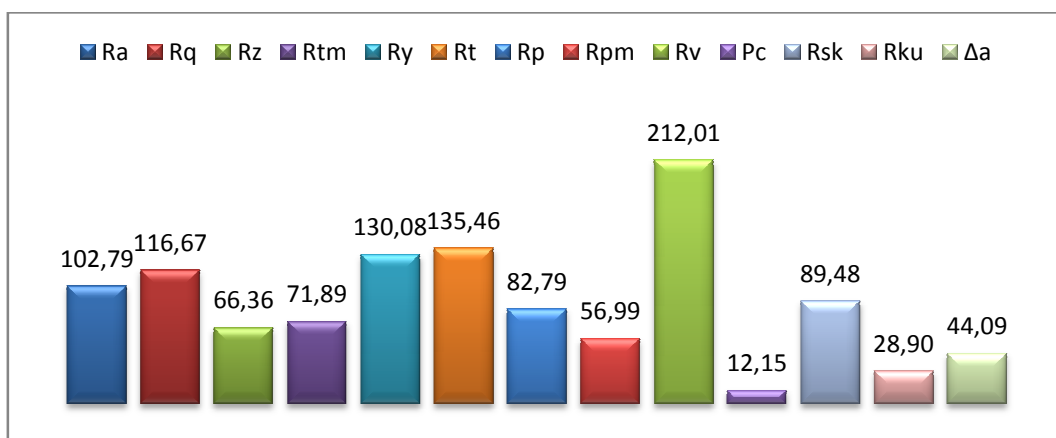


Figure 6.65: Difference percentage of polar graphs area values for MB4

As it can be observed from Figure 6.64, the decreasing order of percentage difference of mean values is:  $R_{sk}$  (94.04%),  $R_v$  (76.14%),  $R_t$  (53.33%),  $R_y$  (51.5%),  $R_q$  (46.76%),  $R_a$  (42.17%),  $R_p$  (35.32%),  $R_z$  and  $R_{tm}$  (30.63%),  $R_{pm}$  (24.78),  $\Delta a$  (18.73%),  $R_{ku}$  (12.85%) and  $P_c$  (6.4%).

While for Figure 6.65, the decreasing order of percentage difference of polar graphs area values is:  $R_v$  (212.01%),  $R_t$  (135.46%),  $R_y$  (130.08%),  $R_q$  (116.67%),  $R_a$  (102.79%),  $R_{sk}$  (89.48%),  $R_p$  (82.79%),  $R_{tm}$  (71.89%),  $R_z$  (66.36%),  $R_{pm}$  (56.99%),  $\Delta a$  (44.09%),  $R_{ku}$  (28.9%), and  $P_c$  (12.15%).

### 6.6.2) Ruiz model for MB4 test

No comparison is presented for this test, due to the difficulties in the determination of the friction coefficient.

### 6.7) DISCUSSION

As it can be observed from Figures 6.14, 6.15, 6.32, 6.33, 6.46, 6.47, 6.64 and 6.65, the representation of the roughness parameters variation by means of the percentage difference of subtended area values many better emphasize the topography changing of specimens surface before and after the tests.

Different graphs were made to understand how the roughness parameters vary according to of the misalignment increasing; in particular, it has been point out that two roughness parameters,  $R_z$  and  $R_{sk}$ , have a linear trend with increasing wear conditions (Figure 6.66 - 6.67).

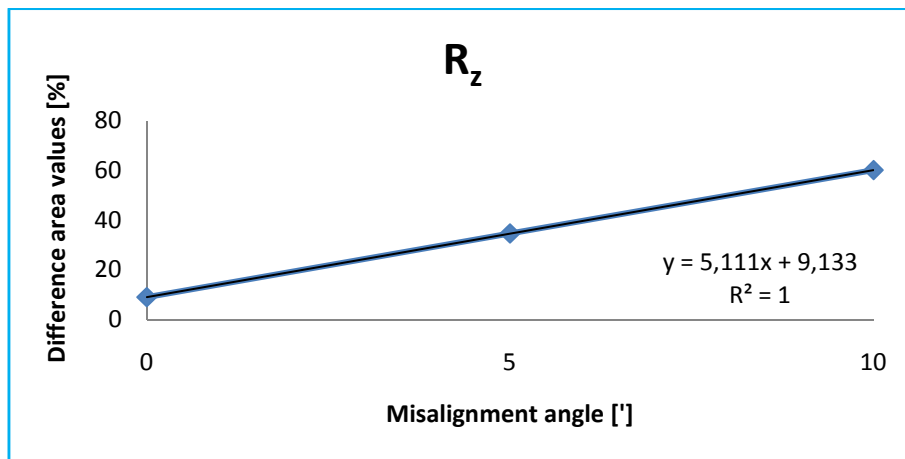


Figure 6.66:  $R_z$  trend versus misalignment

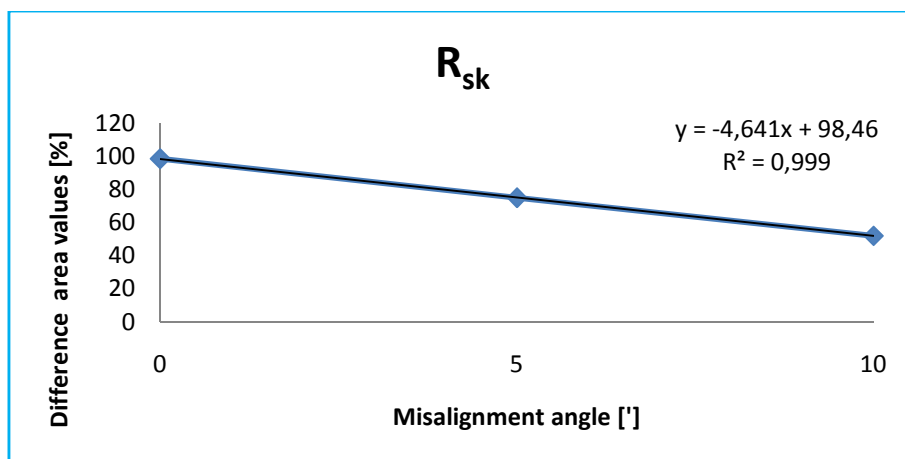


Figure 6.67:  $R_{sk}$  trend versus misalignment

$R_z$  parameter represents the difference in height between the average of the five highest peaks and the five lowest valleys along the assessment length of the profile; the fact that this parameter has a linear course indicates that there is a correlation between the misalignment increasing and the worsening of wear phenomenon.

In fact, like previously described (Chapter 2), being fretting an adhesive wear phenomenon, due a greater sliding (it is proportionally with the misalignment increasing), a higher number of "cold welding" are created, they creating new high peaks when break.

At the same time, being fretting also an abrasive wear phenomenon, due to the debris mixed with the pressurized oil, new increasingly deep valleys are created.

By observing Figure 6.67, it is possible to note the roughness parameter  $R_{sk}$  has a decreasing trend.

The fact that it linearly decreases with the misalignment increasing suggests how this parameter is sensitive to the change of the inclination between the shaft and the hub of the specimen.

It is possible to note that  $R_{sk}$  changes its value; in fact it passes from a value major than zero to one near to zero; this means that, increasing fretting wear, an equal number of peaks and valleys will be created.

This result is very important, because it demonstrates how fretting wear is, at the same time, an adhesive wear (more peaks) and an abrasive wear (more valleys) phenomenon.

Another important aspect that was to be taken into account is that the roughness parameters for the tests MB3 and MB1 (misalignment 5 ['] and 10 [']) decrease, while for the tests MB2 and MB4 (misalignment 0 ['] and 10 ['] but without lubrication) increases.

MB2 trend roughness results are similar to the corresponding of MB4 test; when the shaft (with crowned teeth) is perfectly aligned to the hub (with

straight teeth), probably gaps between the teeth are created and the oil pass from these.

This oil passage doesn't create the lubrication conditions on the contact surface present in the other tests and this is the reason for the similar results of MB2 and MB4 tests; this hypothesis, however, requires further experimental tests in order to be validated.

## CHAPTER 7: CONCLUSION

The aim of my PhD thesis is to better investigate the phenomena involved in real working conditions of aerospace spline couplings; above all the fretting wear has to be taken into account.

This research activity has been carried on from both experimental and theoretical point of view.

Firstly, a specific test bench has been realized. The peculiarity of this test rig is the capability to apply to the test article both torque (by means of a torque generator) and angular misalignments in order to reproduce the real working conditions of spline couplings.

The test bench was initially calibrated with a series of preliminary tests in order to determine the best set up for the wear characterization in the case of crowned splined couplings.

Then, four wear tests to investigate the influence of misalignment (MB1, Mb2 and MB3) and of lubrication conditions (MB4) were carried out.

In order to quantify the damage entity, it was decided to compare the results in term of teeth surface topography, before and after the test.

To do this, roughness parameters available in literature have been used.

In order to evaluate the trend of these parameters, the percentage difference of the polar areas has been chosen, being more sensitive to the corresponding variation.

Among all parameters, it has been noted that both  $R_z$  and  $R_{sk}$  present a linear trend relative to the increasing sliding between the surfaces in contact.

Concurrently to this, an analytical study has been carried on: to this aim different dedicated models (and software) have been developed in order to predict the wear phenomenon.

In particular, the first software allows to determine (as a function of geometry, torque and construction and assembly errors) the real number of engaging teeth in a spline coupling.

This program has been validated by some FEM models (described in Chapter 3).

In addition to this a software, the calculation of the effective contact area and therefore the contact pressure on a crowned spline coupling has been realized; this model has been validated with experimental tests that demonstrate the program reliability, allowing to validate the Hertzian theory (the contact area varies with the cube root of the applied load).

It has also carried out a sliding program that, taking into account the contact area of the surfaces, allows to determine its shifting during a complete rotation of a splined coupling misaligned conditions.

This program has been validated by means of experimental wear tests carried out on the test rig.

Finally, a fretting wear prediction program has been realized using the first parameter of Ruiz.

The comparison between prediction and experimental tests emphasizes a very good correlation.

This thesis has shed further light on the fretting wear behaviour of splined couplings, but it has also raised areas meriting additional research. Ruiz first parameter provided a qualitative description of the wear effect on these components even if further investigations are necessary to better understand this parameter capacity.

In particular, more tests must be done changing the misalignment values and a very great attention must be paid to the effect of the coefficient of friction. To do this, a specify test rig would be realized, to identify the values of the COF respect to the type of lubrication used.

Further advances in knowledge could be obtained by the application of additional computational simulation techniques to compare with the results of this thesis. As an example, FE-based wear simulations.

# Bibliography:

- [1] Cuffaro V. *Calcolo analitico delle sollecitazioni e deformazioni in un accoppiamento scanalato*. Master Thesis, Politecnico di Torino (in Italian), 2009.
- [2] R. Giovannozzi, *Costruzione di Macchine*, Volume 1, Pàtron Editore, Bologna, Terza Edizione, 1980 – Capitolo VIII, “*Chiavette longitudinali, tangenziali e trasversali; linguette, accoppiamenti scanalati; dentature Hirth; spine*”
- [3] Dudley, “*When splines need stress control*”, *Product Engineering*, December 1957, 56-61
- [4] Barrot, “*Analyse et modélisation du comportement des liaisons cannelées – Mise en place des bases d’un outil d’assistance à la conception*”, INSA Thesis, November 2006
- [5] Niemann, Winter, *Elementi di Macchine*, Volume 1, Edizioni Scienza e Tecnica, Milano, 1983 – Capitolo 18, “*Accoppiamento di albero e mozzo*”
- [6] Machinery’s Handbook, 27<sup>th</sup> Edition, Copyright 2004, Industrial Press, Inc., New York, NY – “*Gears, splines and cams*” – “*Involute splines*”
- [7] D.W. Dudley, How to design involute splines, *Prod. Eng.* (October) (1957) 75–80.
- [8] C.H.H. Ratsimba, I.R. McColl, E.J. Williams, S.B. Leen, H.P. Soh - *Measurement, analysis and prediction of fretting wear damage in a representative aeroengine spline coupling* – *Wear* 257 (2004) 1193–1206
- [9] D. Aldham, J. Warburton, R.E. Pendlebery, *The unlubricated fretting wear of mild steel in air*, *Wear* 106 (1985) 177–201.
- [10] R.B. Waterhouse, *Fretting Wear*, ASM Handbook, 32, Friction, Lubrication and Wear Technology, ASM International, 1992, pp. 242–256
- [11] M.V. Korovchinsky, *Local contact of elastic bodies with wear of their surface*, in: *Contact Interaction of Solid bodies and Calculation of Friction Forces and Wear*, Nauka, Moscow, 1971, pp. 130–140.
- [12] L.A. Galin, *Contact problems of the theory of elasticity in the presence of wear*, *J. Appl. Math. Mech.* 40 (1976) 981–986.
- [13] L.A. Galin, I.G. Korovchinsky, *Axisymmetric contact problem of the theory of elasticity in the presence of wear*, *J. Appl. Math. Mech.* 41 (1977) 826–831.
- [14] I.G. Korovchinsky, P.T. Rajeev, T.N. Farris, *Wear in partial slip contact*, *J. Tribol.* 123 (2001) 848–856.

- [15] I.R. McColl, J. Ding, S.B. Leen, *Finite element simulation and experimental validation of fretting wear*, *Wear* 256 (11–12) (2004) 114–1127.
- [16] J. Ding, S.B. Leen, I.R. McColl, *The effect of slip regime on fretting wear-induced stress evolution*, *Int. J. Fatigue* 26 (2004) 521–531
- [17] J.F. Archard, *Contact and rubbing of flat surfaces*, *J. Appl. Phys.* 24 (1953) 981–988.
- [18] R.A. Newley, *The mechanisms of fretting wear of misaligned splined in the presence of lubricant*, Ph.D. thesis, Imperial College, 1978.
- [19] P.M. Ku, M.L. Valtierra, *Spline wear-effects of design and lubrication*, *J. Eng. Ind. Trans. ASME* November (1975) 1257–1263.
- [20] S.B. Leen, I.R. McColl, C.H.H. Ratsimba, E.J. Williams, *Fatigue life prediction for a barrelled spline coupling under torque overload*, *Proc. Inst. Mech. Eng., Part G, J. Aerospace Eng.* 217 (2003) 123–142.
- [21] S.B. Leen, T.H. Hyde, C.H.H. Ratsimba, E.J. Williams, I.R. McColl, *An investigation of the fatigue and fretting performance of a representative aeroengine splined coupling*, *J. Strain Anal.* 37 (6) (2002) 565–583 .
- [22] C.H.H. Ratsimba, S.B. Leen, I.R. McColl, E.J. Williams, *Effect of the coefficient of friction on the fatigue life of splines*, in: A. Varvani- Farahani, C.A. Brebbia (Eds.), *Fatigue Damage of Materials*, WIT Press, Southampton, Boston, 2003, p. 35.
- [23] A.V. Olver, S. Medina, R.F. Baker, D.P. Davies, *Fretting and wear of splined couplings*, *Proceedings of the One Day Seminar organized by the IMechE on Coupling and Shaft Technology for Aerospace Transmissions*, Solihull, June, 1999.
- [24] [http://www.ing.unitn.it/~colombo/USURA\\_CORROSIONE/3-usura.html](http://www.ing.unitn.it/~colombo/USURA_CORROSIONE/3-usura.html)
- [25] [http://www.flitalia.it/en/fl/manuale/en/trasm\\_0107.htm](http://www.flitalia.it/en/fl/manuale/en/trasm_0107.htm)
- [26] Jin O, Lee H, Mall S. *Investigation into cumulative damage rules to predict fretting fatigue life of Ti-6Al-4V under two-level block loading condition*. *Journal of Engineering Materials and Technology*, *Transactions of the ASME* 2003;125(3):315-323.
- [27] Matsuisaki M, Endo T. *Fatigue of metals subjected to varying stress*. In: Kyushu District meeting of the Japan Soc Mech Engrg Fukuoka, 1968, pp. 37-40.
- [28] Stephens RI, Farneti A, Stephens RR, Fuchs HO. *Metal fatigue in engineering*. Wiley-IEEE, 2001.
- [29] Newman Jr JC. *The merging of fatigue and fracture mechanics concepts: A historical perspective*. *Progress in Aerospace Sciences* 1998;34(5-6):347-390.

- [30] Bowden FP, Tabor D. *The friction and lubrication of solids*. Parts 1 and 2. Oxford: Clarendon Press, 1954.
- [31] Houghton D. *Representative fretting fatigue testing and prediction for splined couplings*. PhD Thesis of the University of Nottingham
- [32] Paris PC, Erdogan, F. *A Critical Analysis of Crack Propagation Law*. Trans ASME, J Basic Eng 1963;85(4):528.
- [33] Walker K. *The effect of stress ratio during crack propagation and fatigue for 2024-T3 and 7075-T6 aluminium*. Effects of Environment and Complex Load History on Fatigue Life 1970; ASTM STP 462:1-14.
- [34] Mindlin RD. J App Mech 1949;16:259-268.
- [35] Mindlin RD. , Deresiewicz H. *Elastic spheres in contact under varying oblique forces*, Trans. ASME Ser. E.J. Appl. Mech, 20 (1953) 327-344.
- [36] Johnson K.L. *Contact Mechanics*. Cambridge University Press, Cambridge. 1985.
- [37] Vingsbo O, and Soderberg, D. *On Fretting Maps*. Wear 1988;126:131- 147.
- [38] Zhou ZR, Nakazawa K, Zhu MH, Maruyama N, Kapsa P, Vincent L. *Progress in fretting maps*. Tribology International 2006;39(10):1068- 1073.
- [39] S. Fouvry, P. Kapsa, L. Vincent, *Quantification of fretting damage*. Wear 200 (1996), 186-205
- [40] Zhou Z.R., Vincent L. , *Mixed fretting regime*. Wear, 181-183 (1995) 531-536.
- [41] A.S. Leikin, G.A. Vasil'eva, *Stress concentration and distribution in straight-sided splined shafts in torsion*, Russ. Eng. J. 54 (3) (1974) 39–43.
- [42] B.P. Volfson, *Stress sources and critical stress combinations for splined shaft*, J. Mech. Des. 104 (1982) 551–556.
- [43] C.W.R. McFarlane, E.J. Williams, T.H. Hyde, *The comparison of the boundary element analysis of a high performance spline coupling with experimental measurement*, in: *Coupling and Shaft Technology for Aerospace Transmissions*, IMechE One Day Seminar, Solihull, England, June 9, 1999.
- [44] T.R.Hyde, S.B. Leen, I.R. McColl, *A simplified fretting test methodology for complex shaft couplings*, Fatigue Fract. Eng. Mater. Struct. 28 (2005) 1047-1067
- [45] S.B. Leen. I.J. Richardson. I.R. McColl, I.J. Williams, T.R. Hyde, *Macroscopic fretting variables in a splined coupling under combined torque and axial load*, J. Strain Anal. Eng. Des. 36(5) (2001) 481-499

- [46] S.I. Ivanov, Residual stress and fatigue resistance of splined shafts, Soc. Eng. Res. 5 (7) (1985) 5–7.
- [47] A. Tjenberg, *Load distribution in the axial direction in a spline coupling*, Eng. Failure Anal. 8 (2001) 557–570.
- [48] A. Tjenberg, *Load distribution and pitch errors in a spline coupling*, Mater. Des. 22 (2001) 259–266.
- [49] D.L. Limmer, D. Nowell, D.A. Hills, *A combined testing and modelling methodology for the prediction of the fretting fatigue performance of splined shafts*, Proc. Inst. Mech. Eng., Part G: J. Aerospace Eng. 215 (2001) 105–112.
- [50] Z.M. Levina, *Friction and wear in spline connexions*, Mach. Tooling 37 (11) (1966) 14–21.
- [51] Z.M. Levina, D.N. Reshetov, *Cyclic sliding in spur gear splined joints and nominal calculation of their wear-resistance*, Russ. Eng. J. 54 (7) (1974).
- [52] S. Medina, A.V. Olver, *Regime of contact in spline couplings*, J. Tribol. ASME 124 (2002) 351–357.
- [53] P.L. Hurricks, *The mechanism of fretting wear*, Wear 15 (1970) 389–409.
- [54] D. Aldham, J. Warburton, R.E. Pendlebery, *The unlubricated fretting wear of mild steel in air*, Wear 106 (1985) 177–201.
- [55] L. Vincent, Y. Berthier, M. Goget, *Testing methods in fretting fatigue: a critical appraisal*, ASTM STP 1159 (1992) 3–32.
- [56] Shinde S, Hoepfner DW. *Quantitative analysis of fretting wear crack nucleation in 7075-T6 aluminum alloy using fretting maps*. Wear 2005;259(1-6):271-276.
- [57] Chivers T.C., Gordelier S.C., *Fretting fatigue and contact conditions: a rational explanation of palliative behaviour*, Proc. Inst. Mech. Eng. 199 (1985) 325-337.
- [58] Bill R.C., *Selected fretting wear resistant coating for Ti-6Al-4V alloy*, Wear, 106 (1985) 283-301.
- [59] L. Vincent, Y. Berthier, M. Goget, *Overstressing and overstraining in fretting*, Proc. Leeds-Lyon Symposium, September 1993
- [60] J. Silvers, C.D. Sorensen, K.W. Chase, *A New Statistical Model for Predicting Tooth Engagement and Load Sharing in Involute Splines*, AGMA Technical Resources, ISBN 978-1-55589-982-0 (2010)
- [61] Zhansheng Liu, Guang Zhao, Feng Chen, *Meshing force of misaligned spline coupling and the influence on rotor system*, School of Energy Science and Engineering, Harbin Institute of Technology, Harbin, China, 2008.

- [62] R. A. Marmol, A. J. Smalley, J. A. Tecza, *Spline couplings induced non synchronous rotor vibrations*, ASME, J. Mech. Des., 1980, 102(1), 168-176.
- [63] Cuffaro V., Curà F., Mura A., *Calcolo della deformazione dei denti di alberi scanalati*, AIAS 40° Convegno Nazionale, Palermo, 7-10 Settembre 2011.
- [64] K.W. Chase, C.D. Sorensen, B. DeCares, *Variation analysis of tooth engagement and load strain in involute splines*, Gear Technology June 2010.
- [65] Curà F., Mura A., Gravina M., *Load distribution in spline coupling teeth with parallel offset misalignment*, Proc IMech Part C: J Mechanical Engineering Science DOI: 10.1177/0954406212471916.
- [66] W. J. O'Donnell, *The additional deflection of a cantilever due to the elasticity of the support*, ASME Journal of Applied Mechanics, 1960.
- [67] R. W. Cornell, *Compliance and stress sensitivity of spur gear teeth*, ASME Journal of Mechanical Design, 103 (1981).
- [68] Sato K., Attia M., Waterhouse R., *Determination and control of contact pressure distribution in fretting fatigue.*, editors.: American Society for Testing and Materials, Philadelphia, 1992, pp. 85-100.
- [69] Iyer K, Mall S. *Analyses of contact pressure and stress amplitude effects on fretting fatigue life*. Journal of Engineering Materials and Technology, Transactions of the ASME 2001;123(1):85-93.
- [70] Waterhouse RB. *Fretting Corrosion*. Oxford: Pergamon, 1972
- [71] Hertz, H. R., 1882, *Ueber die Beruehrung elastischer Koerper*, in Gesammelte Werke, Vol. 1, Leipzig, Germany, 1895.
- [72] Curti G., Curà F., *Teoria di Hertz sui corpi a contatto*, Corso di Costruzione di Macchine tenuto presso il Politecnico di Torino.
- [73] <http://www.fujifilm.com/products/prescale/>
- [74] Wittkowsky BU, Birch PR, Dominguez J, Suresh S. *Apparatus for quantitative fretting fatigue testing*. Fatigue and Fracture of Engineering Materials and Structures 1999;22(4):307-320.
- [75] Jin O, Mall S. *Effects of independent pad displacement on fretting fatigue behavior of Ti-6Al-4V*. Wear 2002;253(5-6):585-596.
- [76] Jin O, Mall S. *Effects of slip on fretting behavior: Experiments and analyses*. Wear 2004;256(7-8):671-684.

- [77] Nishida T, Kondoh K, Xu JQ, Mutoh Y. *Observations and Analysis of Relative Slip in Fretting Fatigue*. Y. Mutoh SEKaDWH, editor.: American Society for Testing and Materials International, West Conshohocken, PA, 2003.
- [78] Sabelkin V, Mall S. *Investigation into relative slip during fretting fatigue under partial slip contact condition*. *Fatigue and Fracture of Engineering Materials and Structures* 2005;28(9):809-824.
- [79] M. Varenberg IEaGH. *Slip Index: A New Unified Approach to Fretting*. *Tribology Letters* 2004;17(3):569-573.
- [80] Madge JJ, Leen SB, McColl IR, Shipway PH. *Contact-evolution based prediction of fretting fatigue life: Effect of slip amplitude*. *Wear* 2007;262(9-10):1159-1170.
- [81] Smith KN, Watson, P., Topper, T.H. *A stress strain function for the fatigue of metals*. *J Mat, JMLSA* 1970;5:767-778.
- [82] Fatemi A, Socie D. *A critical plane approach to multiaxial fatigue damage including out of phase loading*. *Fatigue Fract Eng Mater Struct* 1988;11(3):149-165.
- [83] Madge JJ, Leen SB, Shipway PH. *A combined wear and crack nucleation-propagation methodology for fretting fatigue prediction*. *International Journal of Fatigue* 2008;30(9):1509-1528.
- [84] Ruiz C, Boddington, P.H.B., Chen, K.C. *An investigation of fatigue and fretting in a dovetail joint*. *Exp Mech* 1984;24:208-217.
- [85] Gadelmawla E.S., Koura M.M., Maksoud T.M.A., Elewa I.M., Soliman H.H., *Roughness parameters*, Original Research Article *Journal of Materials Processing Technology*, Volume 123, Issue 1, 10 April 2002, Pages 133-145